MANTLE FLOW AND MELTING BENEATH YOUNG OCEANIC LITHOSPHERE: SEISMIC STUDIES OF THE GALÁPAGOS ARCHIPELAGO AND THE JUAN DE FUCA PLATE

by

JOSEPH STEPHEN BYRNES

A DISSERTATION

Presented to the Department of Earth Sciences
and the Graduate School of the University of Oregon
in partial fulfillment of the requirements
for the degree of
Doctor of Philosophy

June 2017

DISSERTATION APPROVAL PAGE

Student: Joseph Stephen Byrnes

Title: Mantle Flow and Melting beneath Young Oceanic Lithosphere: Seismic Studies of the Galápagos Archipelago and the Juan de Fuca Plate

This dissertation has been accepted and approved in partial fulfillment of the requirements for the Doctor of Philosophy degree in the Department of Earth Sciences by:

Douglas Toomey	Chairperson
Emilie Hooft	Core Member
Eugene Humphreys	Core Member
Alan Rempel	Core Member
Allen Malony	Institutional Representative

and

Scott L. Pratt	Dean of the Graduate School

Original approval signatures are on file with the University of Oregon Graduate School.

Degree awarded June 2017

DISSERTATION ABSTRACT

Joseph Stephen Byrnes

Doctor of Philosophy

Department of Earth Sciences

June 2017

Title: Mantle Flow and Melting beneath Young Oceanic Lithosphere: Seismic Studies of the Galápagos Archipelago and the Juan de Fuca Plate

In this dissertation, I use seismic imaging techniques to constrain the physical state of the upper mantle beneath regions of young oceanic lithosphere. Mantle convection is investigated beneath the Galápagos Archipelago and then beneath the Juan de Fuca (JdF) plate, with a focus on the JdF and Gorda Ridges before turning to the off-axis asthenosphere. In the Galápagos Archipelago, *S*-to-*p* receiver functions reveal a discontinuity in seismic velocity that is attributed to the dehydration of the upper mantle. The depth at which dehydration occurs is shown to be consistent with prior constraints on mantle temperature. A comparison between results from receiver functions, seismic tomography and petrology shows that mantle upwelling and melt generation occur shallower than the depth of the discontinuity, despite the expectation of high viscosities in the dehydrated layer. Beneath the JdF and Gorda Ridge, low *Vs* anomalies are too large to be explained by the cooling of the lithosphere and are attributed to partial melt. The asymmetry, large *Vs* gradients, and sinuosity of the anomalies beneath the JdF Ridge are consistent with models of buoyancy-driven upwelling. However, deformation zone processes appear to dominate mantle flow over seafloor spreading beneath the Explorer and Gorda diffuse plate boundaries. Finally, *S*-to-*p* receiver functions

reveal a seismic discontinuity beneath the JdF plate that can only be attributed to seismic anisotropy. Synthesis of the receiver function results with prior *SKS* splitting results requires heterogeneous anisotropy between the crust and the discontinuity. Models of anisotropy feature increasing anisotropy before the decrease at the discontinuity, but well below the base of the lithosphere, and a clockwise rotation of the fast direction with increasing depth. In these results and even in the *SKS* splitting results, additional driving mechanisms for mantle flow such as density or pressure anomalies are required.

This dissertation includes previously published and unpublished co-authored material.

CURRICULUM VITAE

NAME OF AUTHOR: Joseph Stephen Byrnes

GRADUATE AND UNDERGRADUATE SCHOOLS ATTENDED:

University of Oregon, Eugene, Oregon, USA
Iowa State University, Ames, Iowa, USA

DEGREES AWARDED:

Doctor of Philosophy, Geological Sciences, 2017, University of Oregon
Bachelors of Science, Physics and Mathematics, 2011, Iowa State University

AREAS OF SPECIAL INTEREST:

Seismic Imaging Techniques
Processing of Oceanic Bottom Seismometer Data
Mantle Dynamics of the Lithosphere-Asthenosphere System

PROFESSIONAL EXPERIENCE:

Research Staff, University of Minnesota, 2016-2017

Graduate Assistant, University of Oregon, 2011-2017

Undergraduate Researcher, Iowa State University, 2009-2011

GRANTS, AWARDS, AND HONORS:

Johnson Award for Research, University of Oregon, 2012, 2013, and 2015

AGU Fall Meeting Outstanding Student Paper Award, 2014

NSF East Asia Pacific Scientific Institute (EAPSI) Grant, 2013

PUBLICATIONS:

Byrnes, J. S., D. R. Toomey, E. E. E. Hooft, J. Nábělek, and J. Braunmiller, Mantle dynamics beneath the discrete and diffuse plate boundaries of the Juan de Fuca plate: Results from Cascadia Initiative body wave tomography, *Geochem. Geophys. Geosys.*, accepted.

Malony, A. D., M. A. H. Monil, C. Rasusen, K. Huck, J. Byrnes, and D. Toomey (2016), Towards scaling parallel seismic raytracing, *IEEE International Conference on Computational Science and Engineering*.

Malony, A. D., S. McCumsey, J. S. Byrnes, C. Rasmusen, S. Keever, and D. R. Toomey (2016), A data parallel algorithm for seismic ray tracing, *International Meeting on High Performance Computing for Computational Science (VECPAR)*.

Byrnes, J.S., Hooft, E.E.E., Toomey, D.R., Villagómez, D.R., Geist, D.J., and Solomon, S.C. (2015), An upper mantle seismic discontinuity beneath the Galápagos Archipelago and its implications for studies of the lithosphere-asthenosphere boundary, *Geochem., Geophys., Geosys., 16,* 1070–1088, doi:10.1002/2014GC005694

ACKNOWLEDGMENTS

I am deeply grateful for the time and patience of my advisors, Douglas Toomey and Emilie Hooft. I want to thank the other graduate students in the Hooft/Toomey labs, including Matt Beachly, Anne Wells, Kohtaru Araragi, Afshin Golamy, Ben Heath, Miles Bodmer, Brandon VanderBeek, Gillean Arnoux, Dan O'hara, and Eunyoung Kim. I would like to extend my thanks to Hitoshi Kawakatsu and Akiko Takeo for my summer at the Earthquake Research Institute at the University of Tokyo, and Max Bezada for my time at the University of Minnesota. I owe special gratitude to other members of this and other departments, in particular but not limited to, Eugene Humphreys, Leif Karlstrom, Alan Rempel, Allen Malony, Josh Roering, Edward Davis, David Schmidt, Becky Dorsey, Amanda Thomas, Jim Watkins, Greg Retallack, Mark Reed, and Paul Wallace. Jessica Lodweyk and Kasey Adherhold at IRIS were always helpful when working with Cascadia Initiative data. Craig Rassumesen and Rob Yelle wasted much of their time on my trivial computer issues. Finally, I am ever in debt to the office staff in the department, and would like to thank Marla Trox, Sharon Douglas, Sandy Thoms, Dave Stemple, and Vicki Arbeiter.

For my partner, Linley Davidson, who keeps me whole

TABLE OF CONTENTS

Chapter Page

I. INTRODUCTION 1

II. AN UPPER MANTLE SEISMIC DISCONTINUITY BENEATH THE GALAPAGOS ARCHIPELAGO AND ITS IMPLICATIONS FOR STUDIES OF THE LITHOSPHERE-ASTHENOSPHERE BOUNDARY 8

Introduction 8

Seismic Data and Receiver Functions 13

Results 20

Discussion 26

Spatial Relationship of Seismic Velocity Anomalies and the G Discontinuity 26

The G Discontinuity Marks the Base of Fully Dehydrated Mantle 29

Potential Temperature of the Plume and Surrounding Mantle 31

A Scenario for Mantle Melting and Seismic Velocity Changes 33

The Amplitude of the G Discontinuity 37

The G discontinuity is not the LAB 39

Conclusions 42

Bridge 43

Chapter Page

III. MANTLE DYNAMICS BENEATH THE DISCRETE AND DIFFUSE PLATE BOUNDARIES OF THE JUAN DE FUCA PLATE: RESULTS FROM CASCADIA INITIATIVE BODY WAVE TOMOGRAPHY 45

Introduction 45

Geological Setting 48

Data and methods 51

Seismic Experiments 51

Measurement of Delay Times 53

Tomographic Method 56

Results 59

Teleseismic Delay Times 59

Tomographic Model 63

Model Resolution 70

Discussion 75

Physical Properties 75

Geodynamic Processes 82

Juan de Fuca Ridge and Plate 83

Ridge-Transform-Ridge Plate Boundaries 90

Gorda Ridge and Plate 91

Conclusion 93

Bridge 94

Chapter Page

IV. FLOW IN THE OCEANIC ASTHENOSPHERE BENEATH THE JUAN DE FUCA PLATE: RESULTS FROM S-TO-P RECEIVER FUNCTIONS WITH CASCADIA INTIATIVE DATA 96

Introduction 96

Seismic Data and Receiver Functions 99

Results 103

Receiver Functions 103

Models of Isotropic Seismic Velocity 106

Models of Anisotropic Seismic Velocity 111

Discussion 118

Conclusion 124

V. DISSERTATION CONCLUSION 125

APPENDICES 127

A. CHAPTER II THE EFFECT OF DEHYDRATION ON SEISMIC VELOCITY 127

B. CHAPTER III SUPPORTING INFORMATION 131

C. CHAPTER IV APPENDIX A AND SUPPLEMENTAL FIGURES 147

REFERENCES CITED 157

LIST OF FIGURES

Figure Page

Chapter II

1. Map of the Galápagos Archipelago and the seismic network. White triangles are seismic stations. Stations with names that begin with G formed the temporary array; PAYG is part of the GSN. The Galápagos Spreading Center (GSC) and the direction of Nazca plate motion in a hotspot reference frame [*Gripp and Gordon*, 2002] are shown. The dashed lines show the locations of the profiles in Figures 2 and 5. Inset shows the broader setting of the study area. 14

2. Depth sections through the CCP stack of the S-to-p receiver functions. (a, b) Cross sections in the south-to-north direction. (c, d) Cross sections in the west-to-east direction. The locations of the cross-sections are shown in Figure 1. The dashed line in each plot marks the depth of the largest negative amplitude of the CCP stack. The amplitude (Sp/S) of the CCP stack is the ratio of the amplitude of the S-to-p converted phase to that of the direct S arrival.. 16

3. Depth to the conversion point of the negative receiver function phase beneath the Galápagos Archipelago and receiver function stacks within the southeastern archipelago and surrounding region. (a) Contour map of the depth (gray scale) to the negative phase in the CCP stack of the receiver functions. The stations are shown as triangles, with station G08 labeled in white (see text for discussion). The islands are outlined. The solid lines show the locations of the profiles in Figures 2 and 5. The piercing points of the receiver functions at 80 km depth are shown as 30 red and 50 blue circles for conversion points deeper and shallower than this depth, respectively; the 16 white circles could be included in either region. The hachured area reflects the uncertainty in the boundary between the southeastern archipelago and the surrounding region. See text for discussion. (b) Stacks of the receiver functions from the southeastern archipelago (red solid line) and surrounding region (blue solid line) plotted as functions of depth. The dashed lines show twice the standard error of the mean for each stack in the corresponding color. The amplitude of the stacks is scaled as in Figure 2. 18

4. Waveform modeling of the three receiver function stacks from the surrounding portions of the archipelago (left column), the southeastern archipelago (middle column), and the region over the Galápagos mantle plume (right column). (Top row: a, c, and e) Amplitudes of the positive (black lines) and negative (blue lines) phases in synthetic receiver functions as functions of the velocity contrast across the G discontinuity; see text for

details. The observed amplitude of the positive phase (conversion at the Moho, magenta line) and the negative phase (conversion at the G discontinuity, green line) for each receiver function stack are shown (dashed green lines show the uncertainty in the amplitude of the negative phase). The best-fitting velocity contrast is chosen by matching the observed and modeled negative-phase amplitudes (bold gray dashed line), and the error in the velocity contrast (thin gray dashed lines) corresponds to the uncertainty in the amplitude of the negative phase. (Bottom row: b, d, and f) Comparison of the receiver function stack from the surrounding portions of the archipelago, the southeastern archipelago, and the region over the Galápagos mantle plume (blue, red, and yellow, respectively) with the best-fitting synthetic receiver function for each region (black). The residual receiver function (black dashed line) is the difference between the observed and synthetic receiver function and represents structure in the receiver function that we have not modeled. The significance of the residual receiver function can be inferred relative to two standard errors for the stack (dashed lines in the color corresponding to each region). 19

5. Overlays of the depth of the G discontinuity from Figure 2 (dashed lines) on cross sections through the seismic tomographic models of *Villagómez et al*. [2014]. (a, b) Cross sections in the south-to-north direction. (c, d) Cross sections in the west-to-east direction. The locations of the cross sections are shown in Figure 1. The seismic velocity anomalies are plotted as percent change relative to a one dimensional velocity model that corresponds to the 1350℃ adiabat (Figure 11 of *Villagómez et al*. [2007]). 28

6. Scenario for mantle melting and its effect on physical properties (cf. Figure 1 of *Choblet and Paramentier* [2001]). (a) Diagram showing the approximate depth extent of the carbonatite, hydrous, and anhydrous melting regimes over the plume. (b) The corresponding melting rate for a given upwelling rate (solid line) and water content of the mantle (dashed line) as functions of depth. (c) Schematic changes in viscosity (solid line) and seismic velocity (dashed line) as functions of depth as a result of dehydration of the upwelling mantle. (d) Schematic cross section at 91° W, modified from *Villagómez et al*. [2014], showing mantle flow and melting processes beneath the Galápagos region. Mantle flow directions are shown in green, the plume in orange, the partially to fully dehydrated volume in gray, the zone of anhydrous silicate melting in light orange, elevated temperature and water content within the plume in black, and the observed G discontinuity and inferred depth of the anhydrous solidus in red. 34

Figure Page

Chapter III

1. a) Major tectonic features in the study area. Black lines are transform faults, double lines are spreading centers, and the line with triangles is the Cascadia megathrust. Bold arrows indicate the direction of absolute plate motion, and thin arrows indicate the direction of ridge migration. Numbers next to the bold arrows are estimates of the velocity of absolute plate motion in mm/yr [*DeMets et al.*, 2010]. Streaked areas indicate diffuse plate boundaries. ..... Tectonic features of interest are marked by capital letters; starting near 48˚N and moving south along the ridge-transform-ridge system, A marks the Endeavour Segment, B the Cobb Offset, C Axial Seamount, D the Cascadia Depression, and E the Escanaba Segment. The scale bar in the bottom-left approximately shows 200 km for the Mercator projection at these latitudes. b) Age of the seafloor for the JdF, Gorda, and Pacific plates [*Wilson,* 1993].... 47

2. a) Map of the study area and the locations of the OBSs used. Blue and red triangles show stations deployed during the northern and southern legs of the Cascadia Initiative, respectively. Reoccupied sites that tie the northern and southern deployments together are shown by half red and half blue triangles. Yellow triangles show broadband OBSs deployed during the Blanco transform experiment. Background colors show bathymetry in kilometers below sea level. Thick and thin contours show 1 and 2.5 km below sea level, respectively. 53

3. Example seismograms for teleseismic *S* phases recorded on the transverse component of OBSs. The vertical, dotted line shows the part of the seismogram used for cross-correlation. a) Seismograms of a magnitude 7.0 event in Japan, recorded during the first year of the Cascadia Initiative. b) Seismograms of a magnitude 6.6 event off-shore of New Guinea recorded during the second year of the Cascadia Initiative and the Blanco Experiment. 55

4. a) Locations of the 60 events used in this study. b) Histogram of the azimuth of the delays measured for this study. 60

5. Summary of the delay times. a) Mean delay times in seconds recorded at each station after applying event statics and sediment corrections. b) Mean delay times in seconds recorded at each station after applying only the event statics. The datasets in Figure 5a and 5b have been separately demeaned. c) One-way travel times through seafloor sediments at each station in seconds, which were subtracted from the measured delay times for Figure 5a. Circles are stations where the method of *Ruan et al.* [2014] was used, squares are stations where interpolation was used. d) The standard

deviation of the delay times in seconds recorded at each station (not the uncertainty of the observations). 62

6. Horizontal cross sections through the tomographic model at a) 50 km depth, b) 100 km depth, c) 200 km depth, d) the average over 0 to 200 km depth, e) 300 km depth, and f) 400 km depth. The images are masked where there is no ray path coverage.. 65

7. Vertical cross sections through the tomographic model. The images are masked where there is no ray path coverage. The locations of select features are indicated at the top of the plots. a) Cross section across the northern JdF plate. b) Cross section across the southern JdF plate. c) Cross section along the Blanco transform. d) Cross section across the Gorda Ridge. e) Cross section along the JdF Ridge. The map in the upper right shows the locations of the cross sections..... 67

8. a) Shear-wave velocity anomalies as a function of the age of the lithosphere to the east and west of the JdF Ridge (blue), the Gorda Ridge (orange), and the East Pacific Rise (yellow) averaged over the upper 200 km. Each profile was set to 0% at an age of 0 Myr. The vertical bars show the standard deviation, not the uncertainty, of the velocity anomaly at a given age. b) Map showing the regions where velocities were taken from for the JdF (blue) and Gorda (orange) Ridges. 69

9. Examples of Backus-Gilbert averaging kernels. (Top row: a, b, c, and d). Averaging kernels for chosen model parameters in map view. The inner and outer contours show the 0.5 and 0.25 levels, respectively, for kernels normalized to 1. Black circles show the location of the model parameter. a) Three parameters at 100 km depth throughout the study area. b) Three model parameters at the same location as in a) but at 300 km depth. c) Three parameters near ridge-transform intersections at 100 km depth. d) Parameters on each side of the JdF and Gorda Ridges at 100 km depth. (Bottom row: e, f, g, and h) Line plots of averaging kernels against depth for the model parameter with the matching color in the map directly above. See text for discussion.. 72

10. Inversion of a synthetic data set generated for a model with a regular pattern of anomalies. The recovered model is shown at 100 km depth (a), 300 km depth (b), averaged over the upper 200 km (c), and along longitude 128˚W (g). Anomalies from the starting model are shown for the same regions in panels d, e, f, and h.. 74

11. Trends of Vs anomalies averaged over the upper 200 km against the age of the lithosphere. a) Plots of velocity against age for the JdF region (blue),

Gorda region (orange), the East Pacific Rise (yellow), and a half-space cooling models (black and dashed). Each profile was set to 0% at an age of 0 Myr. Vertical bars show the standard deviation, not the uncertainty, of the velocity anomalies at a given age. b) Map showing the regions where the velocities were taken from in a) for the JdF (blue) and Gorda (orange) region..... 76

12. Contours of depth-averaged variations in melt fractions in the upper 200 km (in %). The same regions are masked as in Figure 6d, with the addition of the regions south of the Mendocino transform fault and east of the Cascadia megathrust. The calculation and associated uncertainties are described in the text.. 81
13. Magnitude of the gradient of the *Vs* anomalies shown in Figure 6d. The bold lines show the 0.03 %/km contour. The same regions are masked as in Figure 6b. The calculation is described in the text.. 84

14. Scenario for upwelling and melting beneath the JdF Ridge. Melt fractions are qualitatively shown in shades of orange, the lithosphere in blue, streamlines by black lines with arrows, the edge of station coverage by the vertical dashed line, and approximate depths are given on the left. See text for discussion.. 85

15. Comparison between *Vs* anomalies (orange), the asymmetry of mantle Bouguer anomalies (ΔMBA, black, dashed lines and text, from *Marjanović et al.*, [2011]), and helium ratios (blue, from *Lupton et al.*, [1993]) along the JdF Ridge. The orange line shows the difference between *Vs* anomalies averaged over the top 200 km of the mantle along transects 75 km east and directly on the JdF Ridge; positive values indicate increasing *Vs* to the east of the ridge axis. ΔMBA is the difference between gravity anomalies 50 km east and west of the JdF Ridge from three ridge-perpendicular transects; positive values indicate a greater mass deficit to the west of the ridge... 88

Chapter IV

1. Topographic map of the study area and the locations of the OBSs used. Blue triangles show stations deployed during the first or third year of the Cascadia Initiative, red triangles show stations deployed during the second year of the Cascadia Initiative, and sites reoccupied during a northern and southern deployment are shown by half red and half blue triangles. Background colors show bathymetry in kilometers below sea level. Thick and thin contours are drawn at 1 and 2.5 km below sea level..... 98

2. Vertical (a) and radial (b) seismograms for a magnitude 7.1 event off the coast of Peru, which occurred on September 25th, 2013. Seismograms are aligned to the predicted arrival time by the IASPEI radial earth model.. 100

3. Event distribution. a) Locations of the 73 events used in this study. b) Rose diagram of the azimuth of the station-event pairs used in this study..... 102

4. Receiver function results and comparison with synthetics for crustal structure. a,b,c) Stacks of receiver functions (colored) from the JdF-Ridge, JdF-plate, and Gorda regions, respectively, with the associated the 95% confidence intervals (dashed lines). Synthetic receiver functions for the expected crustal structure are shown in black. d) Shaded regions show where the JdF-Ridge (red), JdF-plate (blue), and Gorda (green) stacks were taken from. Black dots show the piercing points of individual receiver functions at 140 km depth. e) Example *Vs* model for the oceanic crust with an 800 m thick sedimentary layer..... 105

5. Results of a grid search to test for a G discontinuity beneath the JdF plate. a) Contours show the χ^2 misfit of the synthetic receiver functions for models with a G discontinuity for different depth and velocity contrasts. b) Examples of predicted receiver functions for velocity models with a G discontinuity at 20, 50 and 80 km depth and a 6% velocity contrast. The solid and dashed black lines show the receiver function from the JdF-plate stack and its uncertainty, respectively..... 109

6. Waveform modeling of the JdF-plate stack with isotropic seismic velocity models. a) Black line shows the predicted amplitude of the *S*140*p* phase in synthetic receiver functions for decrease in *Vs* at 140 km depth, solid and dashed blue lines shows the amplitude of the *S*140*p* phase in the JdF-plate stack and its uncertainty, respectively. b) Black line shows the the best fitting synthetic receiver, solid and dashed blue lines show the JdF-plate stack and its uncertainty, respectively..... 111

7. Waveform modeling of the JdF-plate stack with anisotropic seismic velocity models. a) Colored lines with circles show the predicted amplitude of the *S*140*p* phase, relative to the maxima near 90 km depth, for a decreases in the magnitude of *S* anisotropy at 140 km depth with different fast directions. The solid and dashed black lines show the fast polarization direction from *SKS* splitting for the JdF plate and its uncertainty, respectively. The solid and dashed blue lines show the relative amplitude of the *S*140*p* phase in the JdF-plate stack and its uncertainty, respectively. b) Solid and dashed blue lines show the JdF-plate stack and its uncertainty, respectively. The red and green lines show the predicted receiver

functions for decrease in *S* anisotropy of 6% with fast directions of 20° and 120°, respectively..... 113

8. Each column shows a model of seismic anisotropy found by the Markov Chain Monte Carlo search, as discussed in the text. (a,c,e) Magnitude of *S* anisotropy with depth. (b,d,f) Azimuth of the fast direction with depth. Solid black lines mark the fast polarization direction from *SKS* splitting. 115

9. Comparison between the magnitude of anisotropy in the upper and lower layers of models found by the Markov Chain Monte Carlo search. Colors show the fast direction in the lower layer in degrees. The dashed line marks where models would have the same magnitude of anisotropy in the both the upper and lower layer. See text for discussion..... 119

LIST OF TABLES

Table Page

Chapter II

1. Estimates for the Excess Temperature of the Galápagos Spreading Center Near 91° W 32

2. Estimates for the Excess Temperature of the Galápagos Plume 32

Chapter III

1. Summary of data statistics 58

2. Summary of the parameters for the inversion 60

Chapter IV

3. Summary of parameters used in the Markov Chain Monte Carlo search..... 116

CHAPTER I

INTRODUCTION

The surface expression of plate tectonics is well characterized, but the sub-surface pattern of mantle convection is not. Where oceanic lithosphere diverges at mid-ocean ridges, conservation of mass requires that the asthenosphere rises toward the surface. Hence, mantle convection beneath spreading centers has been inferred since the earliest days of plate tectonics. Rising asthenosphere will undergo decompression melting when the pressure-dependent solidus is crossed and this process generates the basalts that form the oceanic crust. Mantle convection beneath the young lithosphere of mid-ocean ridges is therefore a necessary consequence of plate tectonics that is responsible for the creation of nearly 70% of the Earth's surface.

Despite the importance of mid-ocean ridges and oceanic plates to the theory of plate tectonics, the physical state and convective motion of the underlying asthenosphere remain enigmatic. The temperature and pressure dependence of the strength of mantle minerals predicts a weak asthenosphere below the conductively cooling lithosphere. However, because the strength of the upper mantle is uncertain, many mutually exclusive models of mantle convection are possible. While the role of weakening due to partial melt or dissolved water during convection is poorly constrained, even the strength of dry and solid olivine is uncertain at upper mantle conditions due to factors such as grain size or deformation mechanism. Numerical models of convection that assume higher viscosities generally predict that mantle

flow is primarily driven by viscous coupling between the lithosphere and asthenosphere, while models that assume lower viscosities predict that flow can be driven by driving forces such as variations in buoyancy and pressure within the asthenosphere. Because of these uncertainties, the details of mantle convection cannot be discerned from first principles and geophysical observations of the lithosphere-asthenosphere system are necessary to better understand the dynamics of the upper mantle.

This dissertation uses seismic imaging techniques to address unknowns related to mantle flow and melting beneath young oceanic lithosphere. These processes are explored beneath the Galápagos hotspot and the Juan de Fuca plate. In both regions, decades of inter-disciplinary research provide a context to interpret seismic observations. Seismic results are first used to infer the physical state of lithosphere-asthenosphere system. Once it is shown how the seismic observations constrain the temperature, composition, or deformation history of the upper mantle, two interrelated topics concerning geodynamics may be addressed: how is mantle melting distributed with depth, and what are the patterns of mantle convection beneath the lithosphere? Conductive cooling is generally considered to be the first order control on the oceanic lithosphere-asthenosphere system. Variations in mantle temperature are therefore taken as the null hypothesis to explain the seismic observations. However, the observationally constrained models of seismic velocity require that variations in water content, melt fraction, or seismic anisotropy be invoked. Once constraints are placed on physical state of the upper mantle, geodynamic processes may be inferred. While viscous coupling with the lithosphere

must drive some component of flow in the asthenosphere, each chapter discusses evidence for asthenospheric flow decoupled from the motion of the overriding plate. Deep low velocity anomalies also support the existence of a 'volatile-induced' melting regime, where low-degree melts form in the presence of dissolved carbon or water at depths as great as 300 km depth.

Chapter II discusses the seismic structure of the upper mantle and the implications for mantle flow beneath the Galápagos hotspot. Synthesis with previous results from petrology and seismic tomography are used to construct a model of mantle flow and melting in the upper 300 km of the mantle. The *S*-to-*p* receiver function technique is used to identify contrasts in seismic velocity in the upper mantle known as the G discontinuity. In the northern and western regions of the islands, the discontinuity occurs at 72 ± 5 km depth. In the southeastern quadrant of the islands, the depth of the discontinuity deepens to 91 ± 8 km depth. A comparison of these results and results from seismic tomography show that the deepest discontinuity occurs where the plate has passed over the mantle plume. Previously published estimates of the temperature of the Galápagos Spreading Center and plume are consistent with the hypothesis that dehydration of the upper mantle occurs at the discontinuity due melting in the anhydrous regime. Gradual dehydration of the upper mantle during hydrous melting occurs at deeper depths. A contrast in melt fraction at the discontinuity, in addition to dehydration, may also be required to explain the amplitude of the discontinuity.

Though the G discontinuity is often interpreted to mark the lithosphere-asthenosphere boundary, mantle upwelling occurs at depths shallower than the

discontinuity. A comparison between the results from receiver functions with previous results from seismic tomography and petrology reveals that basalts are generated at depths shallower than 70 km, and likely as shallow as 45 km depth. The generation of basalts requires decompression melting of upwelling mantle, and the lithosphere does not experience internal convection. Therefore, despite the expectation that dehydration strengthens the mantle, the discontinuity does not mark the base of the rigid lithosphere, but lies within the actively deforming asthenosphere.

The next two chapters turn to the Juan de Fuca (JdF) and Gorda Ridges, which lie offshore of the Northwestern United States. These two intermediate spreading ridges and the young lithosphere of the JdF and Gorda plates were the target the Cascadia Initiative, a recent community seismic experiment that deployed ocean bottom seismometers across full span of the JdF and Gorda plates. Data from the ocean bottom seismometer component of the experiment are used to investigate mantle flow and melting beneath young oceanic lithosphere with seismic tomography in Chapter III and the *S*-to-*p* receiver function technique in Chapter IV.

Results from seismic tomography of the upper mantle at the JdF Ridge support models of dynamic upwelling. Low *Vs* regions beneath the ridge axis can only be explained by the presence of melt in the asthenosphere, and extend to depths in the volatile-melting regime. Large *Vs* gradients near the JdF Ridge can be created by the freezing of melt during mantle downwelling. Some numerical models of dynamic upwelling, where the buoyancy of the mantle enhances upwelling rates, predict off-axis downwelling, while models of passive upwelling do not provide a

mechanism for a large off-axis *Vs* gradient. Moreover, the distribution of melt about the JdF Ridge is asymmetric, with more melt present beneath the Pacific than JdF plate. Numerical models predict that such asymmetry will arise when a ridge migrates over a modest thermal anomaly in the asthenosphere if dynamic upwelling is occurring, while models of asymmetry during passive upwelling likely require unrealistic thermal anomalies for the JdF region. Finally, near the JdF-Blanco ridge-transform-ridge intersection the low *Vs* anomalies extend eastwards under the JdF plate and form a smoother pattern than the right-angles of surface offsets. Models of dynamic upwelling beneath ridge-transform-ridge systems predict a smoother, sinuous pattern beneath ridge-transform intersections than models of passive upwelling, in accordance with the observed *Vs* anomalies.

In comparison with results for the discrete plate boundary of JdF Ridge, mantle flow is anomalous beneath the diffuse plate boundaries of the Explorer and Gorda deformation zones. The large *Vs* gradients of the JdF Ridge that were attributed to mantle downwelling are absent in both regions. The amplitude of *Vs* anomalies decreases beneath the northern JdF Ridge, and melt is inferred within the entire Gorda region. Results from *SKS* splitting show that mantle deformation beneath the Gorda Ridge is not driven by seafloor spreading or the motion of the lithosphere, but is instead captured by a shear zone between the Pacific and JdF plates. Tomography moreover reveals lower *Vs* anomalies where the Gorda plate is more extensively deformed. Remarkably, the shear-zone between the appear to dominate mantle flow over the influence of either seafloor spreading or mantle buoyancy.

Finally, *S*-to-*p* receiver functions reveal a discontinuity associated with seismic anisotropy beneath the JdF plate. Robust receiver functions are obtained using Cascadia Initiative data for three regions, the JdF Ridge, the Gorda Ridge, and the JdF plate. Discontinuities at depths shallower than approximately 100 km depth cannot be clearly imaged because of large converted phases from seafloor sediments. At depths that can be reliably imaged, no clear phases are observed near either ridge, but a large phase is observed beneath the JdF plate. This phase is attribute to a mantle discontinuity that we refer to as the Lehmann, or L, discontinuity. Previous work has suggested that the onset of melting beneath ridges could be sharp enough to produce a converted phase; in this region melt in volatile-induced regime must be distributed over a length scale longer than approximately 50 km depth so as not to produce a detectable converted phase.

Beneath the JdF plate, mantle deformation at the L discontinuity must be driven by forces within the asthenosphere and not by coupling with the motion of the overriding lithosphere. Fast-polarization directions from *SKS* splitting are nearly parallel to the motion of the plate in a hotspot reference frame, but a persistent clockwise rotation is observed. After rejecting a contrast in isotropic velocity for the observe phase, it is shown that only azimuthal anisotropy with a fast direction rotated clockwise of absolute plate motion by 50 to 90° can satisfy the observations. A set of models of anisotropy are constructed to be consistent with both the *SKS* splitting and receiver functions results. These models all contain a layer of anisotropy parallel or nearly parallel to the motion of the JdF lithosphere, with a

deep region of anisotropy that always displays high magnitudes of anisotropy or azimuths with a large clockwise rotation from the motion of the plate.

To conclude, this dissertation explores outstanding questions related to the nature of mantle flow and melting beneath young oceanic lithosphere. Beneath the Galápagos hotspot and the JdF plate, mantle flow and melting are interconnected and determine the physical state of the upper mantle. Each chapter infers a component of mantle flow decoupled from the motion of the overriding lithosphere, and paints a picture of active mantle flow in the oceanic asthenosphere.

Chapter II of this dissertation has been published, and was co-authored with Emilie E. E. E. Hooft, Douglas R. Toomey, Dennis R. Geist, Darwin J. Villagómez, and Sean C. Solomon. Chapter III of this dissertation has been accepted for publication and was coauthored with Douglas R. Toomey, Emilie E. E. E. Hooft, John Nábělek, and Jochen Braunmiller. Chapter IV of this dissertation is in preparation for publication and was co-authored with Douglas R. Toomey and Emilie E. E. E. Hooft.

CHAPTER II

AN UPPER MANTLE SEISMIC DISCONTINUITY BENEATH THE GALÁPAGOS ISLANDS AND ITS IMPLICATIONS FOR STUDIES OF THE LITHOSPHERE-ASTHENOSPHERE BOUNDARY

From Byrnes, J. S., Hooft, E. E. E., Toomey, D. R., Villagómez, D. R., Geist, D. J., and Solomon, S. C. (2015), An upper mantle seismic discontinuity beneath the Galápagos Archipelago and its implications for studies of the lithosphere-asthenosphere boundary, *Geochem., Geophys., Geosys., 16,* 1070–1088, doi:10.1002/2014GC005694

1. Introduction

Plate tectonics is broadly defined as the steady movement of colder, more rigid lithospheric plates over hotter, more ductile asthenosphere. The lithosphere and asthenosphere are further distinguished thermally by conductive versus advective heat transfer, respectively, because the lithosphere does not convect internally, whereas the asthenosphere does. Seismic studies have documented a seismic discontinuity in the upper mantle beneath ocean basins, historically known as the Gutenberg or G discontinuity [*Gutenberg,* 1948; G*aherty et al.*, 1996; *Bagley and Revenaugh,* 2008], which has often been interpreted as the "lithosphere-asthenosphere boundary" or LAB [*Fischer et al.*, 2010]. This interpretation implies that the transition from lithosphere to asthenosphere, or from conductive to advective regimes, is sharp on the scale of a seismic wavelength [*Rychert et al.*, 2005,

2007; *Kawakatsu et al.*, 2009]. However, the physical processes that give rise to a seismically detectable interface are controversial [*Karato*, 2012; *Rychert et al.*, 2012; *Schmerr*, 2012; *Karato*, 2014], as is the attribution of the G discontinuity to the LAB.

Under the simplest models, the formation of the oceanic lithosphere is by cooling [*Parsons and McKenzie*, 1978; *Faul and Jackson*, 2005], and a seismically sharp interface is not expected [*Stixrude and Lithgow-Bertelloni*, 2005]. By these models, the transition from lithosphere to asthenosphere occurs as minerals lose their strength at elevated temperatures and the lithosphere gradually thickens, approximately as the square root of the age of the plate. Because conductive cooling is gradual and continuous, the higher seismic velocities of the lithosphere should grade into the lower seismic velocities of the asthenosphere over a length scale that is greater than the seismic wavelength typically used to map upper mantle discontinuities [*Stixrude and Lithgow-Bertelloni*, 2005].

Alternatively, models of oceanic lithosphere that include the effects of compositional layering and melt formation and transport can produce a seismically sharp interface in the upper mantle [*Karato and Jung*, 1998; *Karato*, 2012; *Olugboji et al.*, 2013]. In particular, the water content of olivine markedly affects the viscosity [*Karato*, 1986; *Hirth and Kohlstedt*, 1996; *Phipps Morgan*, 1997] and seismic velocity [*Karato and Jung,* 1998] of the upper mantle, with anhydrous olivine predicted to be more viscous (by orders of magnitude), and higher in seismic velocity, than partially hydrated olivine. Because water preferentially partitions into melt, the residuum of mantle melting is predicted to be stronger and higher in seismic velocity than unmelted mantle material. Under this scenario the rheology of

oceanic mantle reflects its melting history. Thus, the depth at which relatively strong, high-velocity mantle is predicted to occur depends only on the depth at which anhydrous melting starts within upwelling mantle and is more or less independent of age [*Gaherty et al.*, 1996, 1999].

Oceanic hotspots are an ideal setting to test if upper mantle seismic discontinuities are thermally or compositionally controlled and whether seismic discontinuities are associated with a LAB. This opportunity arises because the temperatures and compositions of hotspots affect both the thermal structure of the surrounding mantle and the depth of mantle melting. The addition of heat by hotspot upwelling causes mantle isotherms to shoal [*Detrick and Crough*, 1978], resulting in thinning of the thermal lithosphere [*Li et al.,* 2004; *Mittelstaedt et al*., 2011]. Elevated temperatures, however, also drive melting and dehydration of the mantle to greater depths, which produces a thicker layer of relatively high viscosity and high seismic velocity [*Phipps Morgan et al.*, 1995; *Hall and Kincaid*, 2003]. Larger volatile contents in a mantle plume may further deepen the initiation of melting [*Asimow and Langmuir*, 2003; *Asimow et al.*, 2004]. Thermal and compositional models of the oceanic upper mantle therefore predict opposite changes in the rheological and seismic structure of the upper mantle when overriding a hotspot.

Results of previous studies are equivocal on the thermal or compositional origin of upper mantle seismic discontinuities beneath oceanic plates. The Gutenberg (G) discontinuity [*Gutenberg,* 1948], at which velocity decreases sharply with depth, is typically located between 40 and 100 km depth. Many workers have interpreted this

discontinuity as the base of the lithosphere [e.g., *Rychert and Shearer*, 2009; *Rychert et al.*, 2010; *Kind et al.*, 2012, *Schmerr*, 2012]. Moreover, many studies of this seismic discontinuity beneath the Pacific plate indicate that it deepens with age, as expected for a plate that thickens by conductive cooling [*Kawakatsu et al.*, 2009; *Kumar and Kawakatsu*, 2011; *Rychert and Shearer*, 2011; *Schmerr,* 2012], though for young (<30 Ma) lithosphere the depth of the discontinuity identified from SS precursors is greater (50-55 km) than expected [*Schmerr*, 2012]. The seismic discontinuity beneath Hawai'i is observed to shoal along the hotspot chain, which is consistent with a feature that is thermally controlled [*Li et al.*, 2004]. Another hypothesis, which is related to a thermal origin for the G discontinuity, is that accumulation of melt at the base of the thermal lithosphere creates the sharp discontinuity in seismic velocity [*Kawakatsu et al.*, 2009; *Hirschmann*, 2010; *Schmerr*, 2012].

On the other hand, the depth of the upper mantle discontinuity beneath most hotspots and some oceanic plates is consistent with a high viscosity, dehydrated mantle. Analysis of receiver functions from the Cape Verde Islands and Hawai'i indicated the presence of a dehydrated and depleted root [*Lodge and Helffrich*, 2006; *Rychert et al.*, 2013]. Similarly, upper mantle seismic discontinuities beneath Amsterdam Island, Easter Island, the Galápagos Archipelago, and Iceland are all deeper (50 to 80 km) than the predicted depth of the thermal boundary layer at the corresponding crustal ages [*Vinnik et al.*, 2005; *Kumar et al.*, 2005; *Heit et al.*, 2007; *Kumar et al.*, 2007; *Rychert et al.*, 2014]. *Tonegawa and Helffrich* [2012] identified a discontinuity at 50–70 km depth beneath the Philippine Sea that could not be

explained by conductive cooling of the plate. *Beghein et al.* [2014] found that the depth of the G discontinuity beneath the Pacific is independent of plate age and inferred that it is likely formed by dehydration of the topmost mantle at the spreading center and the presence of seismic anisotropy due to lattice preferred orientation below the dehydrated layer.

In this paper we investigate the structure of the upper mantle seismic G discontinuity beneath the Galápagos Archipelago using *S*-to-*p* conversions identified in radial receiver functions derived from teleseismic body waves that were recorded by a temporary broadband array. We aim to test whether thermal or compositional processes define the G discontinuity, and if the G discontinuity separates the lithosphere from the asthenosphere. The Galápagos Archipelago is an ideal setting because the young seafloor age [*Hey and Vogt*, 1977; *Barckhausen et al*., 2001] predicts a thin thermal lithosphere. In addition, previous studies provide detailed seismic images of the mantle velocity structure [*Villagómez et al.*, 2007, 2014] and extensive information on the geochemistry of the lavas throughout the archipelago [*Herzberg and Gazel*, 2009; *Gibson and Geist*, 2010; *Graham et al.*, 1993; *Kurz and Geist*, 1999; *White et al.*, 1993; *Harpp and White*, 2001]. *Rychert et al.* [2014] found a G discontinuity at 75 ± 12 km depth beneath the southwestern Galápagos, which they interpreted to be caused by depletion and dehydration in the upper mantle. We find a similarly deep G discontinuity, but the area can be separated into distinct regions of differing discontinuity depth. We show that mantle melting, volatile removal, and their physical effects can explain the change in discontinuity depth and the associated mantle velocity structure. Moreover, by comparing the structure of

this interface with the mantle seismic velocities and the inferred mantle melting depths, we conclude that above the G discontinuity the mantle is flowing upward and melting over a broad region. Thus the seismic interface does not represent the base of the rigid lithosphere or coincide with the LAB. Our results may have implications for the interpretation of upper mantle discontinuities beneath oceanic plates in other locations.

2. Seismic Data and Receiver Functions

We analyzed seismic data from 10 portable, three-component broadband stations that were installed across the Galápagos Archipelago from September 1999 to April 2002 (Figure 1). The instrumentation used was described by *Hooft et al.* [2003]. The array was augmented by the permanent Global Seismographic Network (GSN) station PAYG on the island of Santa Cruz. The aperture of the seismic array was 300 km by 200 km, and the station spacing was 50 to 70 km.

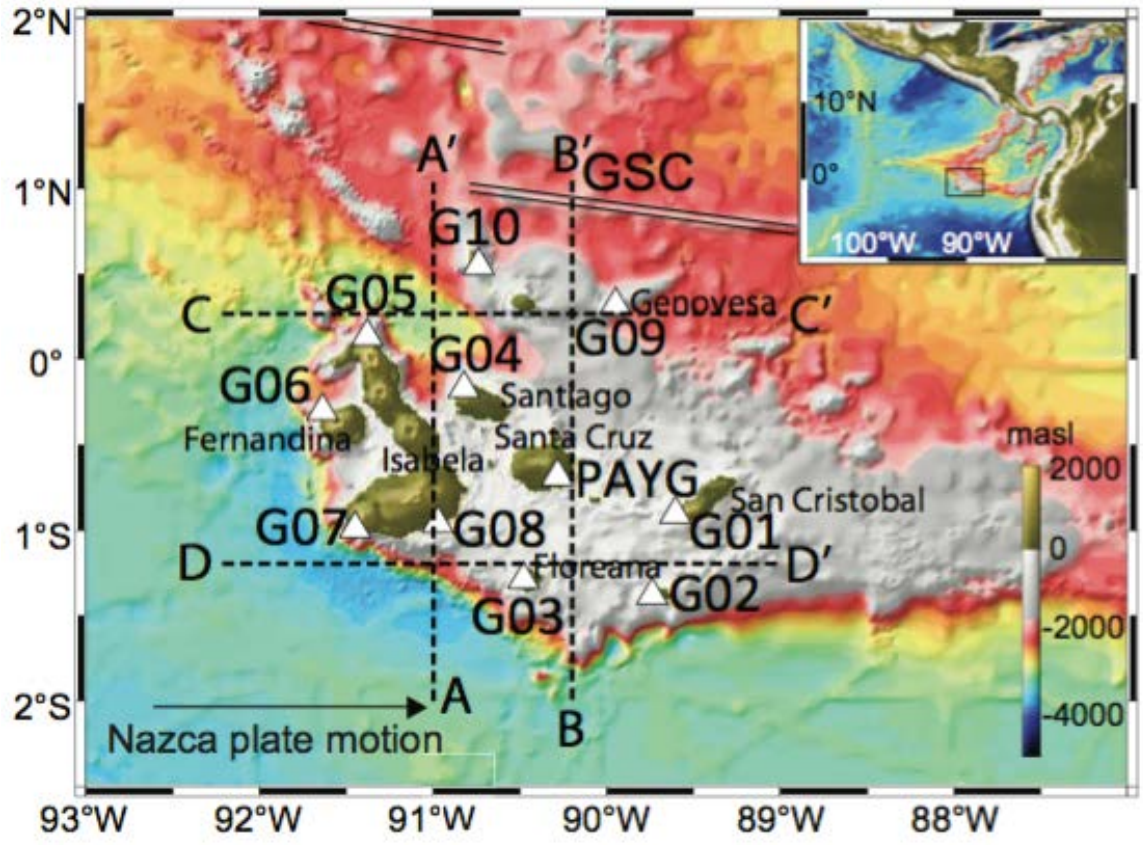

Figure 1. Map of the Galápagos Archipelago and the seismic network. White triangles are seismic stations. Stations with names that begin with G formed the temporary array; PAYG is part of the GSN. The Galápagos Spreading Center (GSC) and the direction of Nazca plate motion in a hotspot reference frame [*Gripp and Gordon*, 2002] are shown. The dashed lines show the locations of the profiles in Figures 2 and 5. Inset shows the broader setting of the study area.

We used the radial receiver function method to identify seismic discontinuities from *S*-to-*p* conversions in the upper mantle beneath the network. Energy converted from *S* to *P* waves arrives before the primary *S* phase and so is not contaminated by crustal reverberations (particularly the reflections from the crust–mantle boundary), making *S*-to-*p* conversions ideal for studies of the upper mantle. Since the converted *p* wave refracts at a larger angle than that of the direct *S* wave, the footprint of *S*-to-*p* conversions is also larger than that for *P*-to-*s* conversions. On the other hand, conversions from *S* phases are noisier and the usable signal is lower

in frequency than for *P* phases. In this study we used the *S* or *SKS* phase from 29 teleseismic events located at 60° to 115° epicentral distance. Events were visually selected, records were rotated into the *P-SV-SH* coordinate system [*Vinnik*, 1977], and the rotated traces were bandpass filtered between 0.01 and 2 Hz before processing.

Receiver functions were calculated using the extended-time, multi-taper deconvolution method [*Park et al.*, 1987; *Park and Levin*, 2000; *Helffrich et al.*, 2006]. To smooth the source spectra, the traces were divided into 10-s-long segments with 50% overlap. Spectra for each segment were calculated with three Slepian tapers and a half-bandwidth parameter of 2.5, and then all the spectra were averaged [*Helffrich et al.*, 2006]. After spectral division, the receiver functions were bandpass filtered between 0.03 and 0.1 Hz to avoid the microseismic noise peak [*Webb*, 1998]. On the basis of visual inspection, traces that had a poor signal-to-noise ratio or that appeared monochromatic were removed from our analysis. To plot the arrival times and polarities of the receiver functions as are done for the more common *P*-to-*s* receiver functions, the time axis and polarity were reversed. Here we discuss changes in velocity in the direction of seismic wave propagation, so an increase in velocity as the wave moves upward produces a converted phase in the receiver function that has a negative sign.

The results of 96 receiver functions are presented using three separate stacking procedures. First, a common conversion point (CCP) stack was calculated [*Dueker and Sheehan*, 1998; *Hansen and Dueker*, 2009] by migrating the receiver functions to depth through the velocity model of *Villagómez et al.* [2014] (Figure 2). The CCP

stack was binned at 20 km intervals and was averaged horizontally over 140 km but was not averaged vertically. Bins with less than five receiver functions after horizontal averaging were rejected. A map of the migrated depth of the negative phase (Figure 3a, dashed lines in Figures 2) was made by taking the minimum value of the CCP stack above 150 km depth.

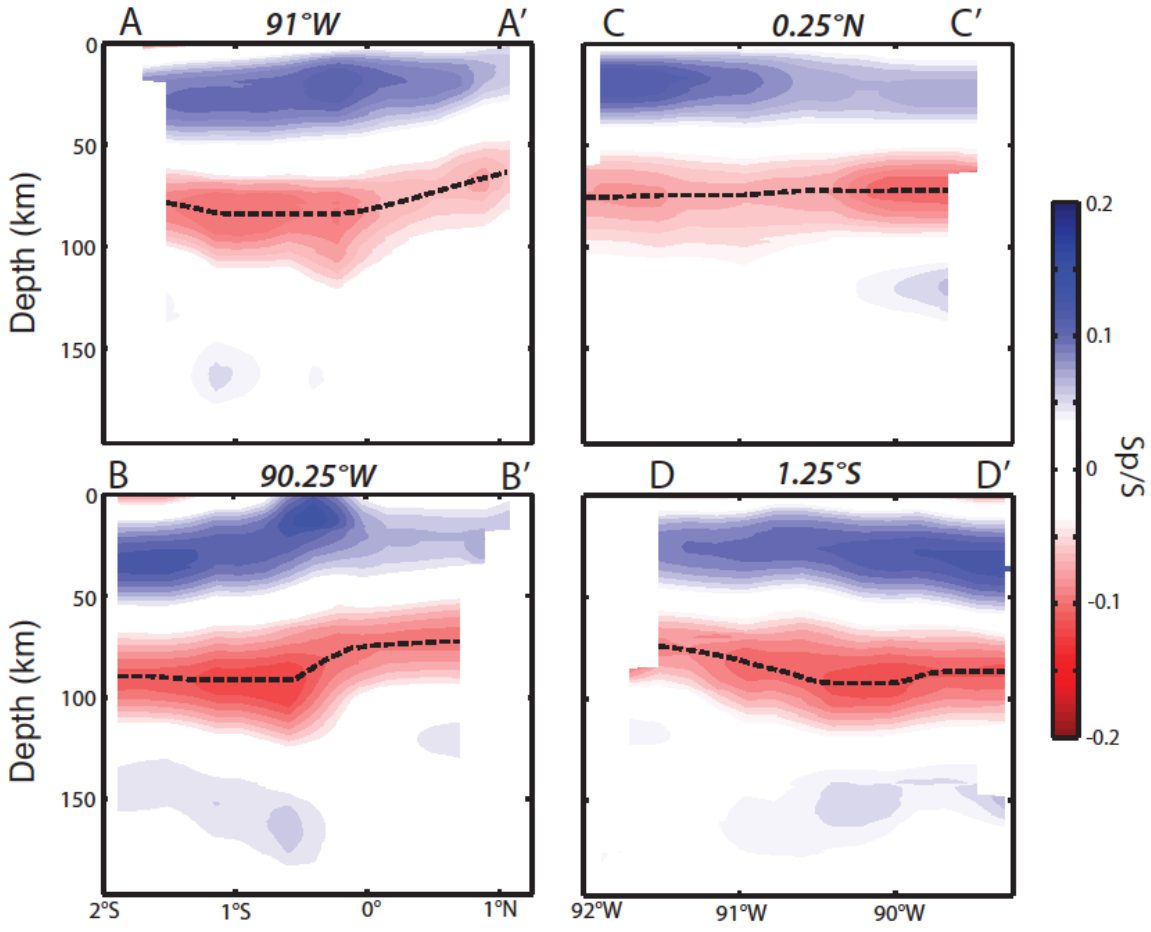

Figure 2. Depth sections through the CCP stack of the *S*-to-*p* receiver functions. (a, b) Cross-sections in the south-to-north direction. (c, d) Cross-sections in the west-to-east direction. The locations of the cross-sections are shown in Figure 1. The dashed line in each panel marks the depth of the largest negative amplitude of the CCP stack. The amplitude (*Sp*/*S*) of the CCP stack is the ratio of the amplitude of the *S*-to-*p* converted phase to that of the direct *S* arrival.

Second, inspection of the CCP stack revealed two regions of differing discontinuity depth, motivating us to stack separately the receiver functions in these two regions. A stack of receiver functions from the southeastern quadrant of the archipelago was compared with a stack from the rest of the study area (Figures 3). The latitudinal and longitudinal boundaries of the southeastern quadrant were estimated by a grid search that sought to maximize the difference in the depth of the G discontinuity between that quadrant and the surrounding region. During the grid search, only boundaries of the southeastern quadrant that included 20 or more receiver functions in both the southeastern archipelago and surrounding region were considered. Standard errors for the amplitude of the phases in these two stacks were found by calculating the standard error of the mean for the stack of receiver functions (shown by the dashed lines in Figures 3b), and the errors in the inferred depth of the phases were found by bootstrapping with 1000 samples; all reported uncertainties are twice the standard error, σ.

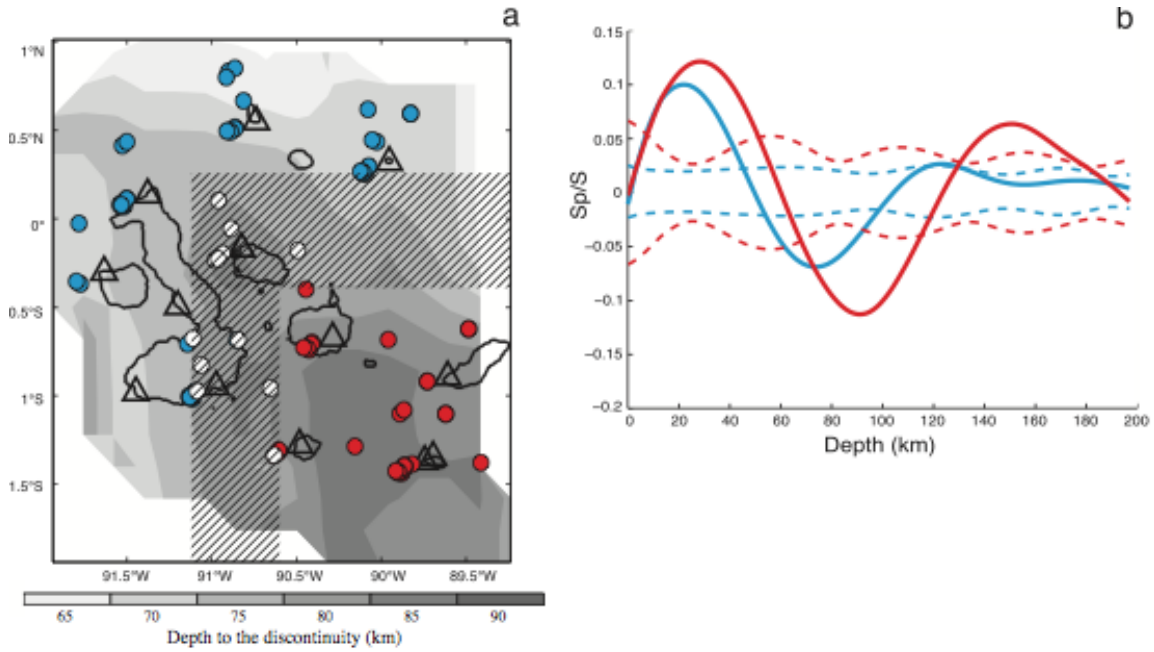

Figure 3. Depth to the conversion point of the negative receiver function phase beneath the Galápagos Archipelago and receiver function stacks within the southeastern archipelago and surrounding region. (a) Contour map of the depth (gray scale) to the negative phase in the CCP stack of the receiver functions. The stations are shown as triangles, and the islands are outlined. The piercing points of the receiver functions at 80 km depth are shown as 30 red and 50 blue circles for conversion points deeper and shallower than this depth, respectively; the 16 white circles could be included in either region. The hachured area reflects the uncertainty in the boundary between the southeastern archipelago and the surrounding region. See text for discussion. (b) Stacks of the receiver functions from the southeastern archipelago (red solid line) and surrounding region (blue solid line) plotted as functions of depth. The dashed lines show twice the standard error of the mean for each stack in the corresponding color. The amplitude of the stacks is scaled as in Figure 2.

Third, to probe upper mantle structure directly over the location of the inferred Galápagos plume at 150 to 200 km depth [*Villagómez et al.*, 2014], we separately stacked receiver functions in the southwestern archipelago (specifically within 50 km of station G08, Figure 4c and 4f). Errors for the amplitude and depth of phases in this stack were found by the same method as for the two regional stacks. We note

that our dataset does not provide spatial coverage to determine the G discontinuity structure immediately west of the plume location (Figure 3a).

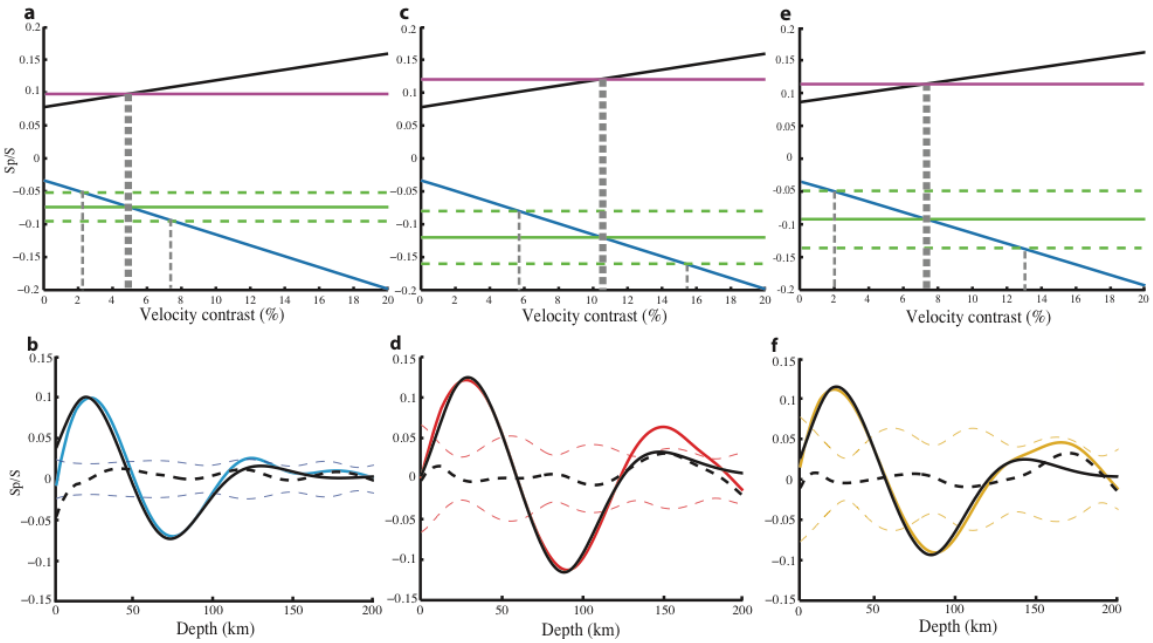

Figure 4. Waveform modeling of the three receiver function stacks from the surrounding portions of the archipelago (left column), the southeastern archipelago (middle column), and the region over the Galápagos mantle plume (right column). (Top row: a, c, and e) Amplitudes of the positive (black lines) and negative (blue lines) phases in synthetic receiver functions as functions of the velocity contrast across the G discontinuity; see text for details. The observed amplitude of the positive phase (conversion at the Moho, magenta line) and the negative phase (conversion at the G discontinuity, green line) for each receiver function stack are shown (dashed green lines show the uncertainty in the amplitude of the negative phase). The best-fitting velocity contrast is chosen by matching the observed and modeled negative-phase amplitudes (bold gray dashed line), and the error in the velocity contrast (thin gray dashed lines) corresponds to the uncertainty in the amplitude of the negative phase. (Bottom row: b, d, and f) Comparison of the receiver function stack from the surrounding portions of the archipelago, the southeastern archipelago, and the region over the Galápagos mantle plume (blue, red, and yellow, respectively) with the best-fitting synthetic receiver function for each region (black). The residual receiver function (black dashed line) is the difference between the observed and synthetic receiver function and represents structure in the receiver function that we have not modeled. The significance of the residual receiver function can be inferred relative to two standard errors for the stack (dashed line in the color corresponding to each region).

3. Results

In the Galápagos archipelago, we identify two clear *S*-to-*p* converted phases in the CCP stack, a positive phase at ~20 km depth and a negative phase at ~80 km depth (Figure 2). We associate the positive-polarity phase with the velocity increase (with increasing depth) at the crust–mantle boundary or Moho. We identify the negative phase with the G discontinuity, a common label for the base of the high seismic velocity layer in the oceanic upper mantle [e.g., G*aherty et al.*, 1996; *Bagley and Revenaugh,* 2008]. A third, low-amplitude, positive-polarity phase may be indicated in records from the southeastern archipelago at ~150 km depth. In this paper we focus on the negative-polarity G phase at ~80 km depth, because the long wavelength of *S*-to-*p* phases relative to the depth to the base of the crust limits the resolution of the shallowest discontinuity, and the phase from ~150 km depth is small in amplitude and waveform modeling suggests that it may be an artifact, as discussed below.

A map of the depth of the phase conversion associated with the negative phase (Figure 3) reveals that the G discontinuity in the southeastern quadrant of the study area is systematically deeper than in the rest of the archipelago. To quantify the difference in the discontinuity depth between these two regions, we used the grid search method, described above as the second stacking method, to stack the receiver functions (Figure 3). From that search, the resulting discontinuity depths are 91 ± 8 km in the southeastern archipelago and 72 ± 5 km in the surrounding region; i.e., the G discontinuity is 19 ± 9 km deeper in the southeastern portion of

the area than elsewhere. The receiver function stacks for the two distinct regions do not change significantly if the borders of the southeastern quadrant are moved by approximately 0.5° in either the latitudinal or longitudinal direction (hachured region in Figure 3a).

The data in the areas where the G discontinuity transitions from relatively deep to shallow depths do not clearly resolve whether the change in the depth of the G discontinuity occurs as a step or a gradient. The western transition, near 91°W, is located above the location of the inferred Galápagos plume at 150 to 200 km depth (Figure 3c of *Villagómez et al.* [2014]). A stack of receiver functions with piercing points at 80 km depth that are within 50 km of site G08 shows a negative phase that migrates to a depth of 82 ± 10 km (Figure 4c). This G discontinuity depth is intermediate between that for the two regional stacks, but within twice the standard error of each. The 82 ± 10 km depth could represent either an actual intermediate depth or a poorly resolved rapid transition from 72 km to 91 km depth. Henceforth, we consider simply the two-region division between the "southeastern quadrant" and "surrounding regions" as shown in Figure 3a unless otherwise noted.

The amplitude of the receiver functions can be used to constrain the velocity contrast across the G discontinuity. In the southeastern quadrant and the surrounding region the amplitude of the G-discontinuity conversion normalized by the amplitude of the direct arrival is –0.12 ± 0.04 and -0.07 ± 0.02, respectively (Figures 3b and 4a and 4b). To estimate the associated velocity contrast, the amplitude of each observed stack was compared with a stack of synthetic receiver functions. The latter were generated for a range of *S*-wave velocity contrasts at the

G discontinuity and two- and three-layer velocity models, using the same ray parameters as the observations. Two-layer models included a topmost mantle layer (4.5 km/s) and an underlying half-space, for which the velocity was varied but was less than the layer above. The three-layer models included an additional crustal layer (4 km/s), for which the velocity is consistent with the results of *Villagómez et al.* [2011]. The thickness of the crust (28 ± 9 km and 20 ± 4) and the depth to the G discontinuity (91 and 72 km) were taken from the results for the southeastern archipelago and surrounding region, respectively. Green's functions were calculated with a reflectivity algorithm [*Park*, 1996; *Levin and Park*, 1998], convolved with a synthetic source, and subsequently deconvolved and filtered following the same method as that used for the observed data. Densities were determined from the Nafe-Drake relation [*Brocher*, 2005]. We adopted a ratio of *P*-wave velocity to *S*-wave velocity, V_p/V_s, of 1.76, and attenuation was not included.

Our estimate of the shear velocity contrast at the G discontinuity depends on whether the Moho is or is not modeled simultaneously with the G discontinuity (three- and two-layer model, respectively). This dependence arises because the phases from the Moho and G discontinuity interfere, which affects their amplitudes. Figure 4 shows the results of synthetic modeling for three-layer models; two-layer models were treated in a similar manner. To estimate the velocity contrast at the G discontinuity, we varied the velocity of the half-space, measured the amplitude of the resulting Moho and G-discontinuity conversions on the synthetic receiver functions, and compared these directly with the observed amplitudes. The uncertainty in the amplitude of the observed G-discontinuity conversion was used

to estimate the error in the velocity contrast at the G discontinuity (Figure 4). When we use the two-layer models (i.e., no Moho), we obtain shear velocity contrasts of 18 ± 5% and 11 ± 3% in the southeastern and surrounding regions, respectively. By including a Moho interface and matching the amplitude of both the positive and negative phases, we infer shear velocity contrasts of 11 ± 5% and 5 ± 3% in the southeastern archipelago and surrounding region, respectively. Our estimate of the shear velocity contrast at the G discontinuity thus decreases by 6 to 7% in a three-layer versus a two-layer model. More complicated models are not required because of the long-period character and overall structure of the receiver functions. Additional modeling indicates that changes in the velocity contrast at the Moho have a small effect on our estimate of the velocity contrast at the G discontinuity. Furthermore, our estimate of the arrival time of the conversion from the G discontinuity is insignificantly affected by interference with the Moho arrival; we estimate that the introduced error is less than 1 km. To evaluate this potential source of error, we compared the arrival time of the converted phase from the G discontinuity in impulsive Green's functions to the arrival time in synthetic receiver functions for a range of ray parameters. The difference in arrival time is equivalent to a change in the depth of the G discontinuity by ±1 km, which is well within our observational error.

The amplitude of a converted phase is also influenced by the sharpness of the associated discontinuity. Receiver functions are most sensitive to velocity gradients distributed over a depth range of less than half the wavelength of the incident phase [*Rychert et al.,* 2007]. The dominant wavelength of the incident phase in our study is

~50 km. As a result, the velocity gradient could be distributed over a range from 0 to ~25 km. Lower gradients produce smaller-amplitude converted phases. Since we estimated the shear velocity contrasts associated with our receiver function with abrupt discontinuities, our estimates of 11 ± 5% and 5 ± 3% are lower bounds.

The deeper positive-polarity phase observed in the southeastern archipelago at a depth of 150 km has an amplitude of 0.06 ± 0.04. A similar phase does not appear in the receiver function stack from the surrounding portion of the archipelago, and the phase is not resolved in a stack of receiver functions with piercing points beneath southern Isabela. Synthetic receiver functions show that the amplitude of this later positive-polarity phase is partially an artifact of deconvolution; the synthetic receiver functions that reproduce the Moho and G-discontinuity conversions form a side lobe that has an amplitude approximately one quarter that of the adjacent negative phase (Figure 4). When corrected for this effect the amplitude of a possible phase converted near 150 km depth is less than twice the standard error (Figure 4); hence this phase does not indicate a discontinuity at high confidence.

The results presented here are consistent with previous receiver function studies in the Galápagos [*Heit et al*., 2007; *Rychert et al*., 2014]. *Heit et al.* [2007] calculated receiver functions from the GSN station PAYG, and *Rychert et al.* [2014] examined receiver functions from PAYG and an array (SIGNET) concentrated on the southern half of Isla Isabela. Our study has the advantage of both broader station coverage and inclusion of the regional mantle velocity model of *Villagómez et al.* [2014]. The use of this velocity model aids in the migration of the receiver functions to depth and, more importantly, provides a context for interpretation of the results. On the

basis of stacks of receiver functions at PAYG from all azimuths, previous studies indicated a negative-polarity phase converted at a depth of 70 km [*Heit et al.*, 2007] and 75 ± 12 km [*Rychert et al.*, 2014], values consistent with our result for most of the Galápagos, 72 ± 5 km. With the SIGNET array, *Rychert et al.*, [2014] mapped lateral variations in the depth of this phase from 66 km to 82 km. That study had the best coverage in the southwestern archipelago, where *Rychert et al*. [2014] found the negative phase to originate from a depth between 76 km and 80 km, a value within the error of that obtained in this study beneath southern Isabela, 82 ± 10 km. The broader spatial coverage of our study allows us to identify the greatest depth of the discontinuity, 91 ± 8 km, beneath the southeastern Galápagos. Given the poor resolution of the Moho, our results (28 ± 9 km and 20 ± 4 from the southeastern quadrant and surrounding regions, respectively) are broadly consistent with those of previous receiver function studies (30 and 37 ± 7 km, *Heit et al.* [2007] and *Rychert et al.* [2014], respectively).

Our estimates of the shear velocity contrast at the G discontinuity are similar to those found in other studies both near and away from oceanic hotspots. Beneath the Pacific plate, reported velocity contrasts are consistently 6 to 7% [*Gaherty et al.*, 1996; *Tan and Helmberger*, 2007; *Kawakatsu et al.*, 2009; *Schmerr*, 2012]. Beneath hotspots, reported shear velocity contrasts are somewhat larger and range from 8 to 20% [*Collins et al.*, 2002; *Lodge and Helffrich*, 2006; *Wölbern et al.*, 2006]. In the southeastern Galápagos the velocity contrast, 11 ± 5%, is comparable to that at other oceanic hotspots, whereas elsewhere in the Galápagos the velocity contrast, 5 ± 3%, is similar to that beneath normal seafloor.

4. Discussion

We discuss our results in the context of previous studies of the Galápagos Archipelago and argue that: (1) the observed *G* discontinuity marks the base of fully dehydrated mantle (i.e., where dry silicate melting begins in upwelling mantle); (2) variations in the depth of the *G* discontinuity are consistent with estimates of the excess temperature of the Galápagos plume relative to the nearby spreading center; (3) mantle melting, volatile removal, and the physical effects of these processes can account for the depth of the G discontinuity, as well as tomographically imaged high-velocity anomalies, (4) the velocity contrast across the seismic discontinuity places bounds on likely variations in composition, water content, and partial melt; and (5) mantle upwelling and decompression melting occur above the *G* discontinuity, implying that the discontinuity is not the LAB. Each of these topics is addressed below.

4.1. Spatial Relationship of Seismic Velocity Anomalies and the G Discontinuity

Previous seismic imaging is consistent with an upwelling mantle plume beneath the Galápagos that shoals toward the Galápagos Spreading Center and is overlain by a high-velocity anomaly formed by chemical depletion and dehydration [*Villagómez et al*., 2007, 2014]. Moreover, *Hooft et al.* [2003] showed that the mantle transition zone is anomalously thin beneath the southwestern archipelago, and they attributed this anomaly to elevated temperatures within a hot plume that is upwelling from depths greater than 410 km. Tomographic analysis of surface wave data and a joint analysis of body and surface wave data show a low-velocity anomaly above the anomalously thin transition zone that is consistent with plume upwelling

[*Villagómez et al.,* 2007, 2014]). The low-velocity anomaly at 200 to 300 km depth is located south of Isabela and is not deflected eastward in the direction of plate motion (Figures 1 and 5). Between 200 and 100 km depth, substantially deeper than the base of the thermal lithosphere, the low-velocity anomaly is inclined toward the Galápagos Spreading Center (Figure 5a). Tomographic imaging also reveals a high-velocity anomaly in the uppermost mantle that is approximately 80 and 150 km thick in the northern and southern archipelago, respectively; this feature is both thicker and more prominent in the southeastern archipelago. *Villagómez et al.* [2007, 2014] attributed this feature, which we term the "high-velocity lid," to chemical depletion and dehydration associated with melt removal. Above the inferred plume and within the high-velocity lid, an approximately 100-km-wide region of reduced velocity is observed at ~40 km depth (Figure 5a); this feature has been attributed to decompression melting of upwelling mantle [*Villagómez et al.,* 2007; 2014].

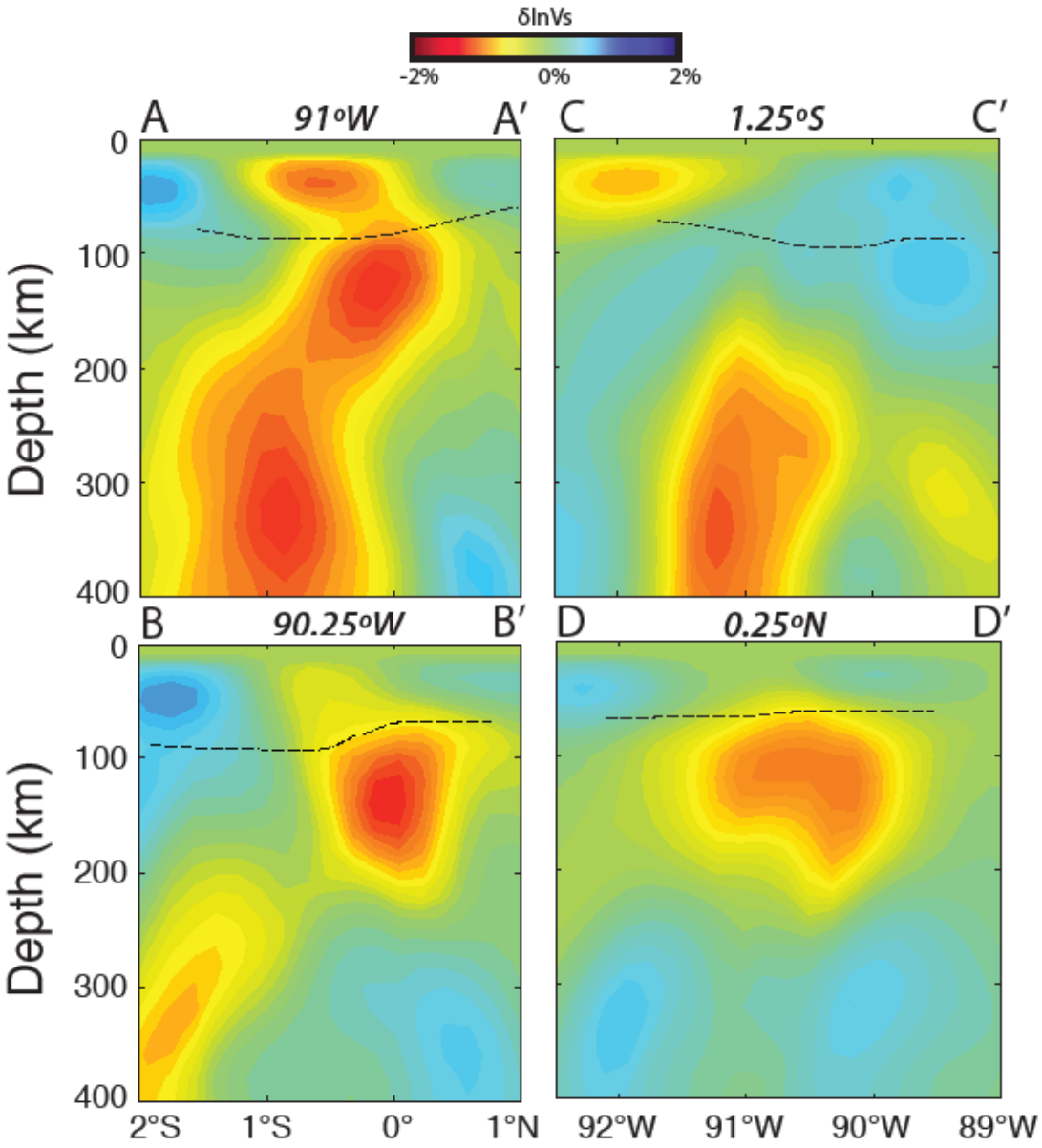

Figure 5. Overlays of the depth of the *G* discontinuity from Figure 2 (dashed lines) on cross-sections through the seismic tomographic models of *Villagómez et al.* [2014]. (a, b) Cross-sections in the south-to-north direction. (c, d) Cross-sections in the west-to-east direction. The locations of the cross-sections are shown in Figure 1. The seismic velocity anomalies are plotted as percent change relative to a one-dimensional velocity model that corresponds to the 1350°C adiabat (Figure 11 of *Villagómez et al*. [2007]).

Beneath most of the archipelago the depth of the G discontinuity lies within or near the base of the high-velocity lid (Figure 5). Moreover, as the Nazca plate moves

to the east [*Gripp and Gordon*, 2002] over the Galápagos plume (near 91°W), both the depth of the G discontinuity and the thickness of the high-velocity lid increase substantially (Figure 3a and Figure 5). This increase in thickness of the high-velocity lid is clear in the difference between the southern ends of profiles A-A' and B-B' (Figure 5a and 5b) and on the eastern end of profile D-D' (Figure 5d). In the northern archipelago, the G discontinuity and the base of the high-velocity lid are shallower and appear at approximately the same depth (north ends of profiles A-A' and B-B', Figures 5a and 5b, and profile C-C', Figure 5c). Exceptions are (i) the presence of the G discontinuity beneath the shallow low-velocity anomaly that overlies the plume (Figure 5a, profile A-A'), and (ii) the presence of the G discontinuity shallower than high-velocity anomalies that extend to the bottom of the tomographic model in the southeastern corner of the study area (Figure 5d, profile D-D'), a pattern that may be the result of downwelling along the margins of the archipelago [*Villagómez et al.,* 2014].

4.2. The G Discontinuity Marks the Base of Fully Dehydrated Mantle

Building on the interpretation of *Villagómez et al.* [2007, 2014], we propose that the observed *G* discontinuity marks the base of a depleted and dehydrated residuum and is a consequence of the removal of hydrogen from olivine by dehydration melting. A thermal origin for the G discontinuity can be rejected because of its depth and spatial pattern. First, plate-cooling models predict that the thermal lithosphere is only 30 to 40 km thick beneath the archipelago [*Turcotte and Schubert*, 2002], values that are approximately half of the observed depth of the G discontinuity (70–90 km). Second, for a thermally controlled boundary, the depth to the *G*

discontinuity is expected to have decreased where the plate has passed over the plume thermal anomaly – a prediction opposite to the observed pattern (Figure 3a).

The observed depth of the G discontinuity and its increase to the east of the Galápagos plume forms the basis for our interpretation of this boundary as the base of a depleted and dehydrated layer (Figure 3a). The observed depths of the G discontinuity are in general agreement with laboratory predictions of the thickness of a layer of depleted and dehydrated residuum beneath oceanic crust (60–100 km depth) [e.g., *Hirth and Kohlstedt*, 1996; *Phipps Morgan*, 1997, *Karato and Jung*, 1998]. Furthermore, given the eastward motion of the Nazca plate in the hotspot reference frame [*Gripp and Gordon*, 2002], we infer that the depth of the G discontinuity increases when the Nazca plate moves over the Galápagos plume. This increase in discontinuity depth corresponds to predictions that elevated plume temperatures will cause melt extraction and dehydration of the mantle to greater depths, producing a thicker layer of high viscosity and high seismic velocities.

In the region of the present Galápagos plume (southern Isabela), the depth of the *G* discontinuity (82 ± 10 km) appears to be intermediate between the depths beneath the southeastern archipelago and surrounding portions of the archipelago (Figure 4). We consider two possible interpretations for this apparent depth. The intermediate depth (82 ± 10 km) could be the result of limited spatial resolution of a more abrupt change with horizontal distance. Alternatively, a *G* discontinuity at this intermediate depth is consistent with a 91-km-deep discontinuity that is in the process of being formed over the mantle plume. This view implies either that the discontinuity forms gradually as it deepens from 72 km depth to 91 km depth over a

horizontal distance of approximately 100 km, or that the locally high melt flux directly above the plume stem alters the seismic structure of the overlying mantle.

4.3. Potential Temperature of the Plume and Surrounding Mantle

Our interpretation of the G discontinuity as the base of a depleted and dehydrated layer is consistent with the predicted depth of the solidus for anhydrous mantle material and independent estimates of mantle temperature at both the Galápagos Spreading Center (Table 1) and the Galápagos plume (Table 2). The *G* discontinuity is at 91 ± 8 km depth only where the plate has passed over the inferred center of the upwelling plume, located beneath southern Isabela. This outcome suggests that the *G* discontinuity depth of 72 ± 5 km in the surrounding region was formed by melting during upwelling beneath the Galápagos Spreading Center away from the direct influence of the upwelling plume stem. Our interpretation that the anhydrous solidus is at 72 ± 5 km depth corresponds to a potential temperature of 1387 ± 25°C (on the basis of the solidus curve of *Herzberg et al.* [2000]). This value is consistent with previous estimates of a 20° to 50°C excess potential temperature at the Galápagos Spreading Center near the archipelago (Table 1 and references therein), relative to a reference mantle potential temperature of 1350°C for parts of the Galápagos Spreading Center not influenced by the plume [*Asimow and Langmuir*, 2003].

Table 1. Estimates for the excess temperature of the Galápagos Spreading Center near 91° W.

Study	Excess temperature (° C)	Method
Ito and Lin [1995]	50 ± 25	From modeling of crustal thickness and gravity
Detrick et al. [2002]	30	From crustal thickness
Asimow and Langmuir [2003]	45	From modeling of major and trace elements of basalts and crustal thickness
Cushman et al. [2004]	20	From modeling of glass chemistry
Ingle et al. [2010]	30	From modeling of trace elements and isotopic data
This study	37[a] ± 25	From an interpretation of the G seismic discontinuity

[a] Excess temperature was calculated relative to a reference mantle temperature of 1350° C, as inferred along the Galápagos Spreading Center between 85° and 87° W [*Asimow and Langmuir*, 2003].

Table 2. Estimates for the excess temperature of the Galápagos plume.

Study	Excess temperature (° C)	Method
Schilling [1991]	214 ± 50	From modeling of the elevation and geographical extent of geochemical anomalies at spreading centers that interact with mantle plumes.
Ito and Lin [1995]	200	From scaling relations between crustal thickness and temperature [*McKenzie*, 1984]
Hooft et al. [2003]	130 ± 60	From mantle transition zone thickness
Herzberg and Gazel [2009]	135[a]	From FeO and MgO contents of primary magmas
Gibson and Geist [2010]	75-100[a]	From variations in rare earth elements in lavas at Fernandina (75 °C) and Santiago (100 °C)
Rychert et al. [2014]	100–200	From an interpretation of a seismic discontinuity as the onset of melting
This study	115[a] ± 30	From an interpretation of the G seismic discontinuity

[a] Excess temperature was calculated relative to a reference mantle temperature of 1350° C, as inferred along the Galápagos Spreading Center between 85° and 87° W [*Asimow and Langmuir*, 2003].

In the southeastern archipelago, the depth of the *G* discontinuity at 91 ± 8 km implies a potential temperature at the time of formation of 1465 ± 30° C [*Herzberg et al.,* 2000]. Relative to a reference mantle potential temperature of 1350°C, this figure gives an excess potential temperature of 115 ± 30° C for the Galápagos plume. This result agrees well with previously published estimates of approximately 75° to 200° C for the excess temperature of the Galápagos plume (Table 2 and references therein).

4.4. A Scenario for Mantle Melting and Seismic Velocity Changes

We propose that mantle upwelling through the depth interval of volatile-induced melting results in a progressive increase in seismic velocity with decreasing depth. When upwelling mantle material subsequently crosses the anhydrous solidus at shallower depth, an abrupt increase in seismic velocity results (Figure 6a-c). This hypothesis provides a consistent explanation of both our results and previous seismic and geochemical studies in the Galápagos Archipelago. By this view, where the plate has been influenced by the plume, volatile-enhanced melting is more substantial, resulting in (i) a deeper G discontinuity and thicker high-velocity lid, and (ii) a high-velocity lid that extends to greater depth than the G discontinuity (Figure 6d).

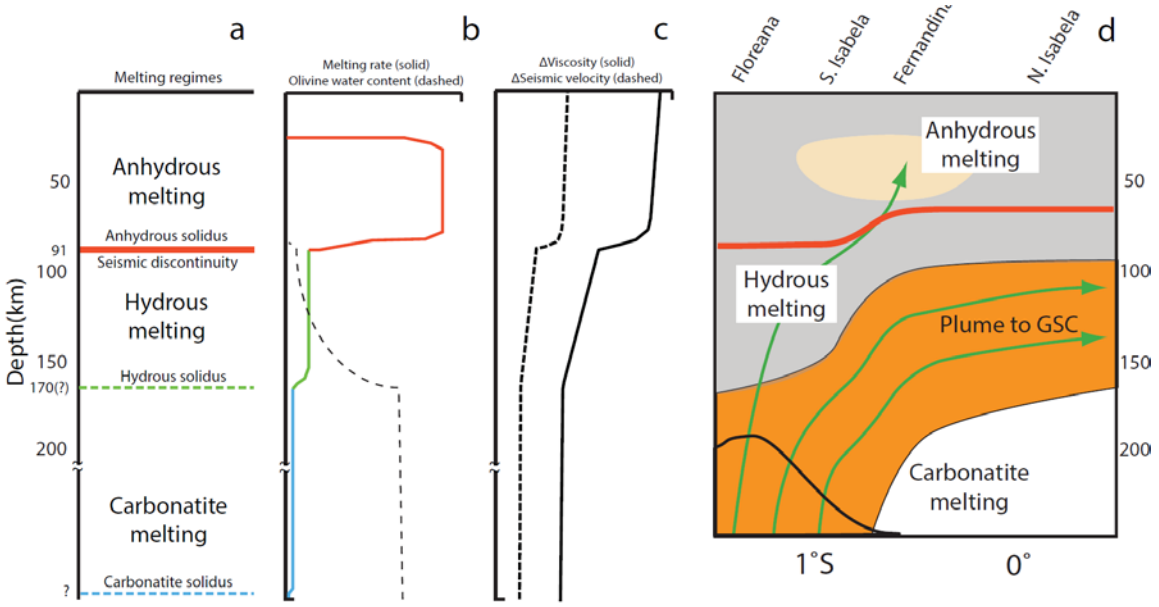

Figure 6. Scenario for mantle melting and its effect on physical properties (cf. Figure 1 of *Choblet and Paramentier* [2001]). (a) Diagram showing the approximate depth extent of the carbonatite, hydrous, and anhydrous melting regimes over the plume. (b) The corresponding melting rate for a given upwelling rate (solid line) and water content of the mantle (dashed line) as functions of depth. (c) Schematic changes in viscosity (solid line) and seismic velocity (dashed line) as functions of depth as a result of dehydration of the upwelling mantle. (d) Schematic cross section at 91°W, modified from *Villagómez et al.* [2014], showing mantle flow and melting processes beneath the Galápagos region. Mantle flow directions are shown in green, the plume in orange, the dehydrating volume in grey, the zone of anhydrous silicate melting in light orange, elevated temperature and water content within the plume in black, and the observed G discontinuity and inferred depth of the anhydrous solidus in red.

We illustrate the viscosity and velocity structures that will result from melt extraction and H_2O removal over a mantle plume in Figure 6. At depths greater than that at which the anhydrous solidus is reached, a small amount of melt is produced because of the presence of volatiles [*Hirschmann,* 2010, and references therein]. Both CO_2 and H_2O induce melting at temperatures below the anhydrous solidus [*Dasgupta et al.*, 2007]. Upwelling through the depth interval between the solidus temperatures for volatile-bearing and anhydrous mantle material produces a small

amount of melt per upward displacement, and the mantle progressively dehydrates (Figure 6b), which increases the viscosity [*Karato*, 1986; *Hirth and Kohlstedt*, 1996; *Phipps Morgan*, 1997] and seismic velocity of the material [*Karato and Jung*, 1998; *Karato*, 2012] (Figure 6c).

When the upwelling mantle reaches the anhydrous solidus, melt production greatly increases [*Hirth and Kohlstedt*, 1996], and the remaining water is removed from olivine, creating a pronounced upward increase in viscosity and seismic velocity that is sharp relative to the seismic wavelength (Figure 6). Whereas the removal of water at the anhydrous solidus can be more pronounced in fractional than batch melting [*Hirschmann,* 2010], melting models that do not yield an abrupt increase in melt production at the anhydrous solidus still predict that all of the water is effectively removed from the mantle at similar depths [e.g., *Asimow et al.*, 2004].

Although the amount of water that remains before the upwelling mantle reaches the anhydrous solidus is likely small [*Hirth and Kohlstedt*, 1996, Figure 4], the physical properties of olivine are predicted to change strongly during the transition from nominally dry to completely dry conditions. Both the viscosity [*Hirth and Kohlstedt*, 1996] and seismic velocity [*Karato and Jung*, 1998; *Karato*, 2012] are reduced by the presence of even a small (less than 100 ppm H/Si) amount of water. Removal of the remaining water thus results in a sharply demarcated, high-viscosity, and high-velocity lid above a region in which velocities and viscosities are lower; in this deeper region, velocity and viscosity gradually increase upward (Figure 6). This model is consistent with positive velocity anomalies that extend

deeper than the *G* discontinuity beneath the southeastern archipelago but reach their maximum amplitude above the discontinuity (Figure 5a through 5c).

The flow pattern of the mantle and the effect of this pattern on melting control the spatial variations in the thickness and internal structure of mantle residuum (Figure 6d). Beneath most of the Galápagos Archipelago, the onset of anhydrous melting in upwelling material at ~72 km is consistent with models of mid-ocean ridge melting at only slightly elevated temperatures beneath the Galápagos Spreading Center as a result of plume-ridge interaction. Within the plume, however, both volatile-enhanced and anhydrous melting begin at greater depths as a result of elevated water content and temperature [*Fisk et al.*, 1982; *Schilling et al.*, 1982; *Detrick et al.*, 2002; *Koleszar et al.*, 2009], so the upward increase in seismic velocity in upwelling material also occurs at greater depths, resulting in a greater depth extent of high-velocity anomalies (to approximately 150 km depth in the southeastern Galápagos, see Figures 5 and 6). Similarly, within the upwelling plume, olivine is dehydrated at greater depths, resulting in the formation of the *G* discontinuity at 91 ± 8 km.

Results from an earlier receiver function study were also interpreted in the context of the onset of melting and the presence of elevated potential temperatures beneath the Galápagos. *Rychert et al.* [2014] estimated excess potential temperatures beneath the Galápagos by attributing a positive-polarity phase at ~135 km depth to the onset of anhydrous melting at a potential temperature of 1450 to 1550˚C. However, this interpretation requires potential temperatures beneath the entire archipelago that are near, or higher than, the maximum potential

temperature of the plume obtained in other studies (Table 2). Instead, we suggest that our hypothesis, which includes the onset of volatile-enhanced melting, together with mantle potential temperatures that are more consistent with other results, better accounts for the observations of *Rychert et al.* [2014] as well as those of this study. This interpretation requires a water content of 1600 to 4000 ppm H/Si in the Galápagos mantle at depths greater than the hydrous solidus [*Hirschmann et al.*, 2009] for the potential temperatures inferred in our study. If small amounts of the initially hydrous melts are retained in the mantle, a small-amplitude, positive-polarity discontinuity could develop [*Havlin and Parmentier*, 2014]. However, this deep phase, if present, is weak in our receiver functions.

4.5. The Amplitude of the G Discontinuity

The relatively large shear velocity contrast (~5 to 11%) across the *G* discontinuity places bounds on variations in mantle composition, water content, and partial melt content across the boundary. Chemical depletion of the mantle during anhydrous melting is not well understood, and its effect on shear wave velocity has been suggested to range from no significant change [*Schutt and Lesher*, 2006], to a ~1% increase after 30% melt removal [*Afonso and Schutt*, 2012], to a 2.6% increase with depletion from pyrolite to harzburgite in the spinel stability field [*Matsukage et al.*, 2005]. Only if the effect of chemical depletion is near the upper end of these estimates could it account for a substantial proportion of the observed velocity contrast. We conclude that major-element depletion does not contribute substantially to the amplitude of the seismic discontinuity documented in this study.

We focus instead on the effect of water on the shear quality factor, Q [*Karato and Jung*, 1998]. Motivated by laboratory experiments which suggest that Q decreases with increasing water content in nominally anhydrous minerals [*Jackson et al.*, 1992; *Aizawa et al.*, 2008], *Karato and Jung* [1998] predicted a reduction in the seismic velocity of hydrated rock that can be described by the absorption band model [*Anderson and Given,* 1982]. The absorption band model predicts that Q decreases with the frequency of a seismic wave as $Q \propto \omega^{-\alpha}$, where ω is the angular frequency andα is a unitless constant that ranges from 0.1 to 0.4 [*Shito et al.,* 2004]. In this model seismic velocity decreases with decreasing Q, and the decrease in velocity is greater at a given Q for smaller values of α. Q would have to lie between ~20 and ~40 and be accompanied by a concentration of water of 100 ppm H/Si at depths greater than that of the G discontinuity beneath the southeastern archipelago and the surrounding portions of the archipelago, respectively, to fully account for our velocity contrasts of 11% and 5% (see Appendix A for details). Similar Q values have been reported from other magmatically active regions between 50 and 100 km depth for shear waves at 1 Hz [*Abers et al., 2014*], but the required values are somewhat lower than estimates for the mantle beneath the East Pacific Rise at similar depths for waves at 10 to 70 s period [*Yang et al.*, 2007]. If other factors contribute to the velocity discontinuity in addition to high attenuation as a result of water, Q values beneath the discontinuity could be larger.

An alternative explanation is that the shear velocity contrast at the G discontinuity may also be affected by the presence of melt beneath an interface [*Kawakatsu et al.*, 2009; *Schmerr*, 2012]. Melt accumulation may occur in the oceanic

asthenosphere between 80 and 100 km depth, because the pressure dependence of the density and viscosity of basaltic melts suggests that melts are neutrally buoyant at these depths [*Sakamaki et al.*, 2013]. The effect of accumulated melt on shear velocity depends strongly on the geometry of the melt distribution. Melt retained in organized, cuspate films reduces seismic velocity by 8% for a melt fraction of 1% [*Hammond and Humphries*, 2000]. Models of melt inclusions with large aspect ratios [*Tandon and Weng,* 1984] or of melt segregated into horizontal bands [*Kawakatsu et al.*, 2009, and references therein] can account for velocity reductions of ~6% with melt fractions as low as ~0.02%. We conclude that partial melt, which could be retained in a range of possible geometries immediately below the G discontinuity, may contribute to the velocity contrast.

Of course, a combination of the above processes is also possible. For instance, if we assume that melt retained in organized cuspate films lowers the shear wave velocity [*Hammond and Humphreys*, 2000], a 4% velocity contrast can be generated by a 0.5% contrast in melt fraction across the G discontinuity. If at the same depth 100 ppm H/Si water were removed from sub-solidus mantle material with a Q of 50 (see Appendix A), dehydration would contribute another 4% change in velocity. If chemical depletion further increases the velocity above the discontinuity by 1-2%, then the net effect of all three processes is a ~9-10% contrast in velocity, similar to the observed value beneath the southeastern archipelago.

4.6. The G Discontinuity Is Not the LAB

Many recent studies invoke the explanation that a sharp decrease in seismic velocity with depth in the oceanic upper mantle corresponds to the boundary that

separates the mechanically strong, conductively cooled lithosphere from the convecting asthenosphere [*Fischer et al., 2010*; *Rychert et al.*, 2010; *Kind et al.*, 2012]. Three independent arguments indicate that the G discontinuity beneath the Galápagos, in contrast, is not the LAB. First, the seismic discontinuity lies beneath a ~100-km-wide region of anomalously low seismic velocities that has been attributed to decompression melting of anhydrous peridotite (see Figures 5 and 6 and the discussion by *Villagómez et al.* [2014]). That the low-velocity anomaly underlies the three most active volcanoes in the archipelago suggests that it is the source region for magmatism. Second, the iron and magnesium contents of young Galápagos lavas, calibrated to the potential temperature and pressure at the point of melt extraction, suggest that primary melt production occurs above the seismic discontinuity. The shallowest melting, inferred from samples throughout the archipelago, occurs at a pressure of 2.0 ± 0.28 GPa, or 60 ± 8 km depth [*Herzberg and Gazel*, 2009]. This depth is 31 ± 11 km and 12 ± 9 km shallower than the discontinuity beneath the southeastern archipelago and surrounding parts of the archipelago, respectively. These values suggest that decompression melting, and hence mantle upwelling, continues to depths shallower than the seismic discontinuity. Third, variations in rare-earth-element concentrations in lavas reflect the proportion of melting that occurred in the garnet and spinel stability fields and thus constrain the depth to the top of the melting column. Analyses of rare-earth-element concentrations in Galápagos lavas are also consistent with mantle melting at depths shallower than the observed seismic discontinuity [*Gibson and Geist*, 2010]. The top of the melting column is inferred to reach depths as shallow as 46

km, whereas the G discontinuity is found at 72 and 91 km depth. Because lithosphere, by definition, should not convect upwards, the G discontinuity beneath the Galápagos Archipelago is not the LAB.

Mantle upwelling has been inferred to occur above the G discontinuity in other volcanically active settings as well. Beneath Iceland, seismic studies have established an increase in seismic velocity at ~80 km depth, sometimes identified with the LAB [*Kumar et al*., 2005]. However, melting is thought to occur as shallow as 40 to 50 km depth [*Shen and Forsyth*, 1995], a result consistent with the broad, low-velocity anomalies observed between 50 and 80 km depth [*Li and Detrick*, 2006]. Beneath the High Lava Plains in Oregon, *Till et al.* [2013] inferred that the melting column extends almost to the base of the crust (~35 km depth), consistent with low shear wave velocity anomalies seen in surface wave tomography [*Wagner et al*, 2012]. In this setting, the LAB had previously been inferred from receiver functions to occur at ~70 km depth [*Li et al*., 2007; *Abt et al.*, 2010]. Moreover, a G discontinuity beneath the island of Hawai'i was observed at 110 km depth [*Li et al.*, 2004], but the minimum depth of melting inferred from thermobarometric modeling of mafic magma compositions is between 35 km and 60 km [*Lee et al.*, 2009].

Our results raise an important question. Many recent studies [e.g., *Fischer et al.*, 2010; *Kind et al.,* 2012, and references therein] have led to the suggestion that the G discontinuity observed in the oceanic upper mantle marks the LAB. We argue that dehydration of the oceanic upper mantle during melting beneath the Galápagos has resulted in a layer of residuum that is not strictly part of the lithosphere, but the

residuum is higher in viscosity than the underlying volatile-bearing peridotite [*Hirth and Kohlstedt*, 1996; *Phipps Morgan*, 1997]. This combination of circumstances may apply in other oceanic regions as well. Moreover, this residuum need not be homogeneous but can be variable in its water content and thus its rheologic and seismic properties. Under certain conditions the residuum can move with oceanic lithosphere, relax [*Phipps Morgan et al.,* 1995], or even upwell and continue melting, as it likely does beneath the Galápagos Archipelago and as it must do beneath spreading centers [e.g., *Ito et al.*, 1999].

5. Conclusions

We have documented a seismic discontinuity, identified as the G discontinuity, in the mantle beneath the Galápagos Archipelago on the basis of *S*-to-*p* conversions mapped with receiver functions. The discontinuity is deeper in the southeastern archipelago than in the surrounding region, 91 ± 8 km versus 72 ± 5 km, respectively. We attribute the seismic discontinuity to the base of a dehydrated and depleted layer that corresponds to the deepest extent of anhydrous melting. The 72-km-deep discontinuity formed at or near the Galápagos Spreading Center, whereas the greater depth of the discontinuity beneath the southeastern archipelago is the result of the Nazca plate having moved over an upwelling mantle plume with an excess potential temperature of 115 ± 30°C. That the observed change in shear velocity across the G discontinuity is larger beneath the southeastern Galápagos than in the surrounding region, 11% versus 5%, could result from some combination of chemical depletion, dehydration of olivine, and a contrast in partial melt fraction.

The G discontinuity lies within a high-velocity lid imaged with seismic tomography. We interpret this geometry as indicating that below the discontinuity, between the depths at which the solidus temperatures for volatile-bearing and anhydrous mantle material are reached, the upwelling mantle is partially dehydrated and viscosity and seismic velocity gradually increase upward. At the anhydrous solidus, the remaining water is removed, creating a sharp increase in viscosity and seismic velocity with further ascent that results in the observed discontinuity. Results from seismic tomography and geochemistry require that mantle upwelling and partial melting continue above the G discontinuity and within the dehydrated and depleted layer. These observations are inconsistent with the assumption, commonly made on the basis of seismic observations in other regions, that such a discontinuity represents the base of the rigid lithosphere, or the LAB. That the G discontinuity is not the lithosphere-asthenosphere boundary in the Galápagos raises the question of the extent to which the association between this seismic discontinuity and the LAB is generally applicable.

6. Bridge

The proximity of the Galápagos Islands to a spreading center allows the study of processes related to both mid-ocean ridges and mantle plumes within one study area. In Chapter II, the G discontinuity was inferred to have two origins – melting beneath the Galápagos Spreading Center in the north and within the mantle plume in the southwest. A scenario for mantle flow and melting beneath the islands was proposed for the upper 300 km of the mantle. Calling on decades of inter-disciplinary research was critical to building these interpretations.

In the next two chapters, this dissertation turns to another tectonic setting where seismic results can be synthesized with decades of work from all areas of Earth Science. The Juan de Fuca and Gorda Ridges and the associated patterns of mantle flow and melting are the primary focus of Chapter III, while Chapter II primarily focused on the effects of a mantle plume. Yet the basic concepts which will be discussed remain the same. Constraints on seismic velocity are used to explore regions of melting beneath young oceanic lithosphere, which in turn provide novel constraints on the pattern of mantle flow in the asthenosphere. Buoyancy-driven mantle upwelling is invoked to explain the observations near the JdF Ridge. The ridge forms a discrete plate boundary that broadly conforms to expectations for a divergent oceanic-oceanic plate boundary. However, beneath the diffuse plate boundaries at the northern and southern end of the JdF Ridge, the influence of seafloor spreading on mantle flow appears to be overwhelmed by the influence of shear-zone processes.

CHAPTER III

MANTLE DYNAMICS BENEATH THE DISCRETE AND DIFFUSE PLATE BOUNDARIES OF THE JUAN DE FUCA PLATE: RESULTS FROM CASCADIA INITIATIVE BODY WAVE TOMOGRAPHY

From Byrnes, J. S., D. R. Toomey, E. E. E. Hooft, J. Nábělek, and J. Braunmiller, Mantle dynamics beneath the discrete and diffuse plate boundaries of the Juan de Fuca plate: Results from Cascadia Initiative body wave tomography, *Geochem. Geophys. Geosys.*, in review.

1. Introduction

The Cascadia Initiative community experiment [*Toomey et al.,* 2014] provides a novel opportunity to investigate mantle structure beneath an entire oceanic plate, from its formation at the Juan de Fuca and Gorda Ridges to its subduction beneath North America. While the Cascadia Initiative study area is relatively compact, within its aperture there are all types of plate boundaries, including spreading centers, transform faults, a convergent margin capable of generating large earthquakes, and diffuse plate boundaries to the north and south (Figure 1a). In addition, decades of interdisciplinary studies indicate that the JdF Ridge interacts with hotspots of the northeastern Pacific. A primary motivation for the Cascadia Initiative was to better understand the regional scale structures that can affect processes occurring near the Cascadia subduction zone, which poses a significant hazard to the Pacific Northwest.

Mantle processes beneath young oceanic plates, particularly those that are bounded by such diverse, discrete and diffuse tectonic boundaries, are not well

constrained by geophysical observations. Factors that can influence mantle convection, melt generation, and internal deformation of young oceanic lithosphere include the motion of the overlying lithosphere, the viscosity of the asthenosphere, and the heterogeneity of the upwelling mantle. A key unknown is whether mantle upwelling occurs as a passive response to the spreading of the plates [e.g. *Phipps Morgan and Forsyth*, 1988], or if dynamic upwelling occurs due to the buoyancy of the upwelling mantle [*Scott and Stevenson*, 1989; *Buck and Su*, 1989; *Katz*; 2010]. A range of observations from different parts of the globe [e.g. *Lin et al*., 1990; *Spiegelman and Reynolds*, 1999; *Hung et al*., 2000; *Wang et al*., 2009; *Key et al*., 2013] has yet to resolve the pattern of mantle convection beneath spreading centers.

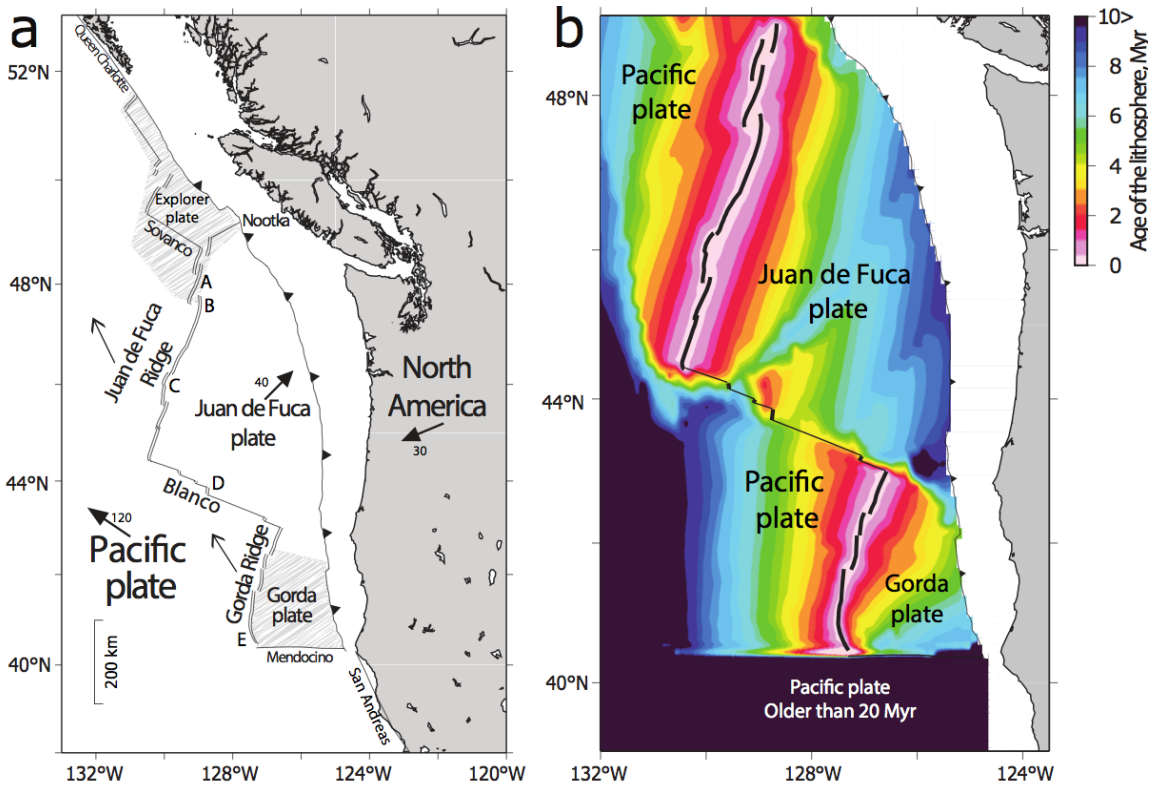

Figure 1. a) Major tectonic features in the study area. Black lines are transform faults, double lines are spreading centers, and the line with triangles is the Cascadia megathrust. Bold arrows indicate the direction of absolute plate motion, and thin arrows indicate the direction of ridge migration. Numbers next to the bold arrows are estimates of the velocity of absolute plate motion in mm/yr [*DeMets et al.*, 2010]. Streaked areas indicate diffuse plate boundaries. Tectonic features of interest are marked by capital letters; starting near 48˚N and moving south along the ridge-transform-ridge system, A marks the Endeavour Segment, B the Cobb Offset, C Axial Seamount, D the Cascadia Depression, and E the Escanaba Segment. The scale bar in the bottom-left approximately shows 200 km for the Mercator projection at these latitudes. b) Age of the seafloor for the JdF, Gorda, and Pacific plates [*Wilson,* 1993].

Here, we invert the delay times of teleseismic *S* waves for velocity anomalies in the upper mantle. We use data recorded by ocean bottom seismometers (OBSs) that were deployed across the JdF and Gorda plates during the Cascadia Initiative [*Toomey et al.,* 2014] and Blanco transform experiments [*Ghorbani et al.*, 2015]. The observed range of *Vs* anomalies requires significant variations in asthenospheric melt content. We infer that dry melting occurs within 100 km of the JdF Ridge, but is

more broadly distributed around the Gorda Ridge. Deeper, volatile-induced melting extends to at least 200 km depth and around the Blanco transform fault. Models of dynamic upwelling better explain both the asymmetric distribution and large lateral gradients of the retained melt fraction near the JdF Ridge than models of purely passive upwelling. Dynamic upwelling also provides an explanation for the sinuous pattern of upwelling we observe near the Blanco transform fault. In contrast, we do not observe evidence for dynamic upwelling beneath the diffuse plate boundaries of the Gorda and Explorer regions. Results from both seismic tomography and *SKS* splitting from the Gorda deformation zone show a strong association with the deformation of the Gorda plate and a weak association with the Gorda Ridge. These results suggest distinct patterns of mantle flow beneath discrete and diffuse plate boundaries.

2. Geological setting

Seafloor spreading in the northeast Pacific occurs along three spreading centers, known as the Explorer, JdF, and Gorda Ridges, which are offset by the Sovanco and Blanco transform faults (Figure 1a). The full spreading rate is 56 mm/yr [*Wilson et al.*, 1993] except along the southern half of the Gorda Ridge, where the spreading rate decreases to ~10 mm/yr [*Riddihough*, 1984]. The ridge system migrates to the northwest at 25 mm/yr due to the higher velocity of the Pacific plate in a hotspot reference frame [*Small and Danyushevsky*, 2003]. Both the Explorer and Gorda plates are undergoing significant internal deformation and re-organization [*Wilson*, 1986; *Wilson*, 1989; *Braunmiller and Nábělek*, 2002; *Chaytor et al.,* 2004; *Dziak*, 2006]. The recently developed Nootka transform fault separates the

Explorer and JdF plates [*Hyndman et al., 1979*; *Riddihough*, 1984], whereas the boundary between the JdF and Gorda plates is diffuse. With this in mind, we refer throughout this paper to the plates subducting beneath North America north and south of the Blanco fracture zone as the JdF and Gorda plates and the regions where crust was created at the JdF and Gorda Ridges as the JdF and Gorda regions, respectively. We do not have seismic data from the Explorer plate; however, we do have coverage of a diffuse deformational region that lies on the Pacific plate south of the Sovanco transform and north of the Cobb Offset along the northern JdF Ridge.

Several observations suggest significant differences in the mantle structure beneath the JdF and Gorda Ridges, even along segments with similar spreading rates. The JdF Ridge is characterized by an axial high, while the Gorda Ridge is characterized by an axial valley [*Hooft and Detrick*, 1995]. This suggests that either the temperature or the supply of melt is greater beneath the JdF than Gorda Ridge [*Chen and Morgan*, 1990]. Results from *SKS* splitting indicate that mantle flow beneath the JdF plate is to first approximation driven by absolute plate motion, whereas mantle deformation beneath the Gorda region is driven by the relative motion of the JdF and Pacific plates with no detectable contribution from the overriding Gorda plate [*Bodmer et al*., 2015; *Martin-Short et al.*, 2015]. Results from surface wave tomography show low *Vs* anomalies beneath the JdF Ridge that are likely due to the retention of melt [*Tian et al.*, 2013] and that are asymmetric about the ridge axis [*Bell et al.*, 2016]; in contrast, weaker variations in seismic velocity are observed beneath the Gorda Ridge [*Bell et al.*, 2016]. Each of these results suggests

different mantle structures and processes beneath the intact JdF and the internally-deforming Gorda plates.

The Blanco transform fault formed ~6 Ma [*Embley and Wilson*, 1992; *Wilson,* 1993] and has lengthened to 350 km. Seismicity occurs along the entire length of the fault [*Braunmiller and Nábělek*, 2008], and is segmented by several pull-apart basins and one active intra-transform spreading center (Figure 1a). Active seafloor spreading likely occurs at the largest of these, the Cascadia Depression [*DeCharon*, 1989; *Braunmiller and Nábělek*, 2008]. Along the northwestern section of the Blanco transform fault, from the Cascadia Depression to the JdF Ridge, large, negative residual mantle Bouguer anomalies are consistent with thickened crust [*Gregg et al.*, 2007]. The major element composition of basalts erupted along this section of the fault suggests that some melting occurs beneath the Pacific plate south of the JdF Ridge [*Gaetani et al.,* 1998].

Relatively little is known about how the aging of the lithosphere affects the JdF and Gorda plates. Before being subducted beneath the North American continent, the JdF and Gorda plates reach ages of 8 to 10 Myr and 4 to 7 Myr, respectively [*Wilson,* 1993]. The age of neither plate corresponds directly to distance from the ridge because of offsets in age at propagator wakes and internal deformation of the Gorda plate (Figure 1b). The age of crust that may have been created at intra-transform spreading centers is also not known. Surface wave tomography results show that seismic velocity in the upper mantle appears to increase rapidly on the eastern flank of the JdF Ridge [*Tian et al.*, 2013; *Bell et al.*, 2016], while an age progressive pattern is less clear for the Gorda plate [*Bell et al.*,

2016]. Onshore seismic studies have identified a seismic discontinuity beneath the recently subducted JdF and Gorda plates at depths near 50 km [*Kumar and Kawakatsu*, 2011] and 25 km [*Liu et al.*, 2012] below the oceanic crust, respectively, likely consistent with a seismic structure that is controlled in part by the aging of the oceanic lithosphere [*Kumar and Kawakatsu*, 2011]. Seafloor sediments are generally thicker where oceanic crust is older and near the subduction zone, and thicknesses range from near zero to approximately 2 km [*Divins et al*., 2003; *Ruan et al.,* 2014; *Bell et al.*, 2015; *Han et al.,* 2016].

3. Data and methods

3.1 Seismic Experiments

We analyzed teleseismic *S* phases recorded by instruments deployed during the Cascadia Initiative [*Toomey et al*., 2014] and the Blanco transform experiment [*Ghorbani et al.*, 2015] (Figure 2). We used data from both the onshore and offshore components of the Cascadia Initiative when measuring the delay times, since signal-to-noise ratios are generally higher in the onshore data, and used data from only the offshore component during the inversions. Stations deployed on the forearc were not used due to high ambient noise levels. Delay times were measured with 29, 28, and 31 OBSs from the first, second, and third years of the Cascadia Initiative, which were deployed from July 26th, 2011 to July 22th, 2012, July 14th, 2012 to August 10th, 2013, and August 2nd, 2013 to July 7th, 2014, respectively. Stations deployed during the first and third years were predominately in the northern half of the study area (blue triangles in Figure 2) and all but three stations from the third year reoccupied sites from the first year. Stations deployed during the second year (red triangles in

Figure 2) were predominately in the southern half of the study area. Triangles which are half red and half blue in Figure 2 mark sites that were reoccupied during at least one northern and southern leg of the Cascadia Initiative and are necessary to connect relative travel time measurements from different deployments. The Blanco transform experiment occurred from September 18th, 2012 to October 5th, 2013, which largely overlaps with the second year of the Cascadia Initiative. We used data from 30 of these broadband OBSs (yellow triangles in Figure 2).

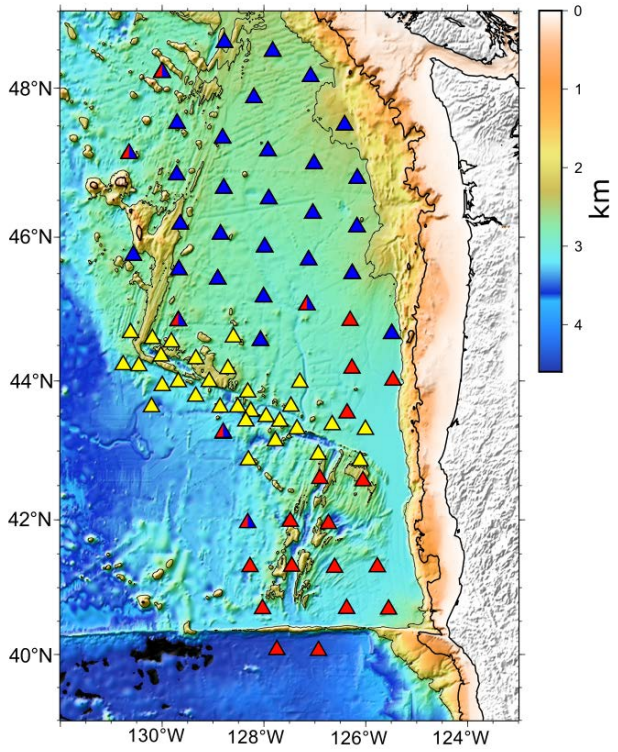

Figure 2. a) Map of the study area and the locations of the OBSs used. Blue and red triangles show stations deployed during the northern and southern legs of the Cascadia Initiative, respectively. Reoccupied sites that tie the northern and southern deployments together are shown by half red and half blue triangles. Yellow triangles show broadband OBSs deployed during the Blanco transform experiment. Background colors show bathymetry in kilometers below sea level. Thick and thin contours show 1 and 2.5 km below sea level, respectively.

3.2 Measurement of Delay Times

We measured the relative delay times of teleseismic *S* and *sS* phases on the transverse channel. Before measuring delay times, all seismograms were corrected for instrument response, rotated into the radial-transverse coordinate system, and filtered. Transfer functions describing the instrument response for all stations were provided by the IRIS DMC and deconvolved from each seismogram, using the method of *Haney et al.* [2012]. The orientations of the horizontal components for OBSs from the Cascadia Initiative were determined by *Sumy et al*. [2015]. Data from all stations were resampled to a common sampling rate of 40 samples per second.

Finally, we applied a third-order bandpass filter with corner periods of 12 and 33 seconds to each seismogram. Signal-to-noise ratios for all arrivals observed on the horizontal components were sensitive to the short-period limit of the bandpass filter, which we attribute to noise from microseisms [*Webb*, 1998]. Examples of aligned seismograms processed in this manner are shown in Figure 3.

We measured the delay times with the method of *VanDecar and Crosson* [1990]. Arrival times were first predicted with the IASP91 velocity model [*Kennett and Engdahl*, 1991] and after cross-correlation the delay times were demeaned. This method preserves the relative arrival time of a phase and therefore is only sensitive to relative variations in seismic velocity. We measured the *sS* phase for one event with estimated depth of 150 km. The minimum standard error of the delay times is assumed to be 0.25 s, which is discussed in Section S1 of the Supporting Information (SI). By convention, a positive (negative) delay time represents a delayed (advanced) arrival with respect to the mean for an event.

Figure 3 (next page). Example seismograms for teleseismic *S* phases recorded on the transverse component of OBSs. The vertical, dashed lines show the part of the seismogram used for cross-correlation. a) Seismograms of a magnitude 7.0 event in Japan, recorded during the first year of the Cascadia Initiative. b) Seismograms of a magnitude 6.6 event offshore of New Guinea recorded during the second year of the Cascadia Initiative and the Blanco transform experiment.

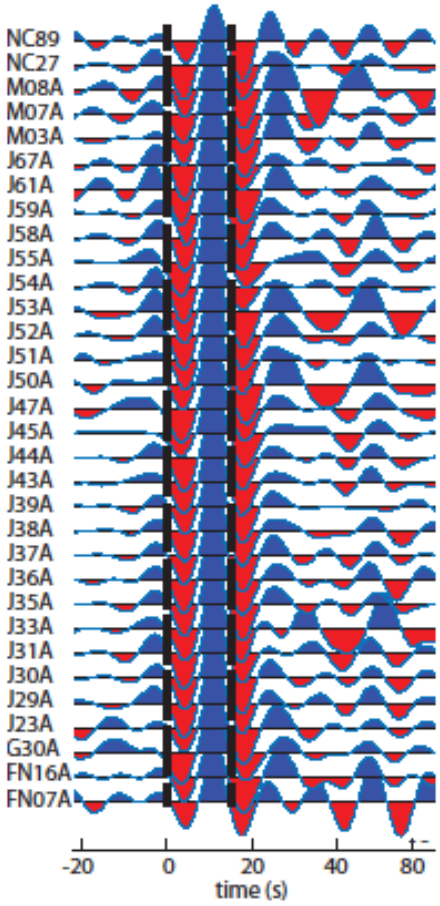
NC89
NC27
M08A
M07A
M03A
J67A
J61A
J59A
J58A
J55A
J54A
J53A
J52A
J51A
J50A
J47A
J45A
J44A
J43A
J39A
J38A
J37A
J36A
J35A
J33A
J31A
J30A
J29A
J23A
G30A
FN16A
FN07A
-20
0
20
40
80
time (s)

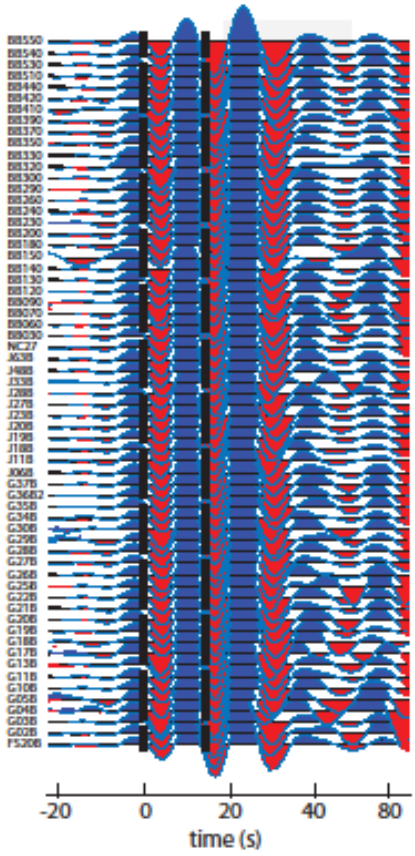
-20
0
20
40
80
time (s)

Variations in the thickness of seafloor sediments across the study area contribute to the delay times of teleseismic arrivals. Before imaging mantle structure, we corrected the delay times for sediment thickness variations using two methods. The first method, described by *Ruan et al*. [2014], measures the thickness and mean *Vs* of a sediment layer from the ratio of vertical and pressure displacements of Rayleigh waves, from which one-way travel times may be calculated. We used corrections found with this method for 43 unique sites by *Ruan et al*., [2014] and *Bell et al.*, [2015]. Sediment corrections for reoccupied sites agreed with 0.05 s between deployments [*Bell et al.*, 2015] and we used the corrections measured for the first station deployed at a given site. Stations deployed on exposed basement were assigned a sediment thickness of zero. For OBSs where the first method could not be used, we interpolated sediment thickness from a global compilation provided by the National Geophysical Data Center [*Divins*, 2003], which have been smoothed laterally over a minimum distance of 10 km. We then calculated the travel time through the sedimentary layer using the mean *Vs* profile of the regional sediments calculated by *Ruan et al*. [2014]. For the 43 sites where both methods could be used, the mean difference in the correction is 0.13 s, with a standard deviation of 0.46 s, which is less than the range of measured delay times and the sediment corrections (see Section 4 and Table 2 below).

3.3 Tomographic Method

The tomographic method used to image upper mantle structure is described in *Hammond and Toomey* [2003] and *Bezada et al*. [2013]. Within the model domain, seismic ray paths and travel times are calculated with Dijkstra's algorithm

[*Dijkstra*, 1959; *Moser,* 1991]; outside the model domain travel times are calculated through a 1-D model using the tau-p method [*Crotwell et al*., 1999]. The inverse problem is solved by simultaneously minimizing the Euclidean norm of the prediction error, the model perturbational vector relative to the starting model, and the roughness of the perturbational model (see *Toomey et al.* [1994] for details). The method also solves for event and station statics, both with units of seconds. The event statics account for the differing distribution of stations that record each event and for unknown structure outside of our image volume. The station statics account for unknown shallow structure beneath a station or station timing errors. The station statics are damped during the inversion to avoid removing signal from mantle structure (see Section 3 of the SI). The partial derivatives of a travel time with respect to the model parameters are calculated by fitting approximations of "banana-doughnut" kernels [*Schmandt and Humphreys*, 2010a] around the ray paths calculated within the model domain [*Bezada et al.*, 2013]. This approach approximates the sensitivity of finite-frequency delay times measured by cross-correlation to seismic structure located near a ray path [*Dahlen et al.*, 2000]. Iterations of the forward and inverse problem are repeated until improvements in data misfit are negligible.

For the results presented below, we adopted the following inversion parameters, which are summarized in Table 1. For seismic ray tracing, the velocity model was gridded at 10 km intervals. The differences between the travel times calculated by our ray tracing approach and by the tau-p method [*Crotwell et al.*, 1999] have a standard deviation of 0.12 s, considerably less than the relative travel

time errors. We solved for perturbations to the starting model every 25 and 50 km in the horizontal and vertical directions, respectively. The bounds of the model are 500 km to the east and west of 128˚W and 800 km north and south of 45˚N. Nodes that are masked in the plots of the velocity models have values of the derivative-weight-sum (DWS) less than 10 [*Toomey and Foulger*, 1989; *Toomey et al.,* 1994]. Weights for the penalty, vertical smoothness, and horizontal smoothness were set to 1, 75, and 150, respectively (see *Toomey et al.* [1994] for details). We chose these parameters by comparing the recovery of anomalies and the misfit to the data in many different inversions of synthetic and actual data. All results shown were obtained by repeating the forward and inverse problems over 6 iterations.

Table 1: Summary of the inversion parameters

Parameter	Value
Ray tracing grid spacing	10 km
Standard deviation of ray tracing errors	0.12 s
Perturbational grid vertical spacing	50 km
Perturbational grid horizontal spacing	25 km
Iterations of the forward and inverse problem	6
Bounds of the model domain	37.8˚N-52.2˚N and 121.6˚W-134.4˚W
Penalty, vertical smoothing, and horizontal smoothing weights	1, 75, 150
RMS of the station terms for the preferred model	0.22 s
RMS of the misfit to the delay times	0.43 s

4. Results

4.1 Teleseismic Delay times

The measured delay times are summarized in 5 and Table 2. We measured 1,343 delays times of teleseismic *S* and *sS* waves on the transverse channel from 108 events at epicentral distances between 30 and 100 degrees (Figure 4a). We measured an average of 12 delay times per event on OBSs. The azimuthal distribution of the delays is dominated by events from Japan, South America, and Tonga (Figure 4b). After measuring the delay times, eight stations from the Cascadia Initiative were removed from our analysis because their timing base is suspect. To identify these sites, we used results from this study and an ongoing analysis of teleseismic *P* wave data (M. Bodmer, personal communication). The latter provides a larger data sample and thus better statistical estimates. Suspect stations were identified by either an average delay time after shallow corrections at each station that fell outside the 2.5 sigma range for both onshore and offshore sites in the Pacific Northwest, or a difference in the mean S wave delay time at reoccupied sites that exceeded 0.8 s.

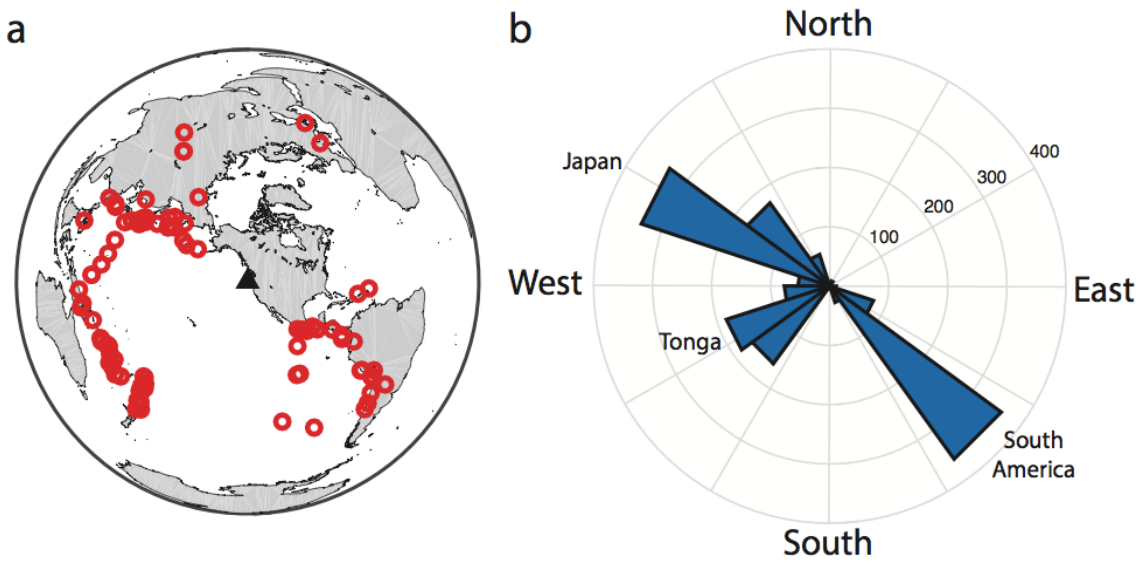

Figure 4. a) Locations of the 108 events used in this study. b) Rose diagram of the azimuth of the delay times measured for this study.

Table 2: Data statistics

Parameter	Value
Number of arrivals	1,343
Number of events	108
Picking error	0.25 s
RMS of the measured arrivals	0.95 s (1.82 s with event terms applied)
Bandpass filter limits	12 to 33 s
RMS of the sediment corrections	0.65 s
RMS of the sediment-corrected arrivals	1.42 s (2.1 s with event terms applied)

Figure 5a shows the mean delay by station after applying corrections for sediment thickness and event statics; these delays are averaged at reoccupied sites; see Section 2 of the SI for mean delays by deployment. Figure 5b shows the mean station delay without a correction for sediment thickness. Both data sets have been demeaned. We did not make corrections for variations in crustal thickness; typical

variations are likely less than 0.5 km [*Carbotte et al.*, 2008; *Han et al*., 2016] and would contribute a delay time of at most 0.01 seconds, which is insignificant in comparison with the uncertainty of a measurement (0.25 s). For the entire set of delays, the RMS and range is 0.95 s and -2.3 s to 3.6 s, respectively, without sediment corrections, and these values increase to 1.42 s and -3.2 s to 4.3 s when sediment corrections are applied. For comparison, the RMS of *S* wave delay times measured across the Western United States is 1.18 s [*Schmandt and Humphreys*, 2010b]. The sediment corrections are shown in Figure 5c and vary between 0 and 2 seconds. This range is approximately one third of the range of the measured delay times. The corrections for sediment thickness generally increase with lithospheric age and are greatest near the continental margin and within the JdF plate. Corrections for sediment thickness within the Gorda region are systematically less than for the JdF region and do not systematically increase with the age of the crust. These patterns are expected because of the sediment loads of the rivers in the Northwestern United States. Figure 5d shows the standard deviation of the delays in seconds measured at each station. This is not the uncertainty of the observations, instead it provides an indication of the heterogeneity of seismic structure beneath a station. The standard deviation at a given station is much smaller than variations of the mean delays between stations, which indicates that upper mantle structure primarily varies at depths shallow enough for rays from different azimuths to sample similar structure. We note that if we were to solve for undamped station statics during the inversion, a large portion of the signal related to upper mantle

heterogeneity would be removed (Figure S9 of the SI); this underlies the importance of making sediment corrections.

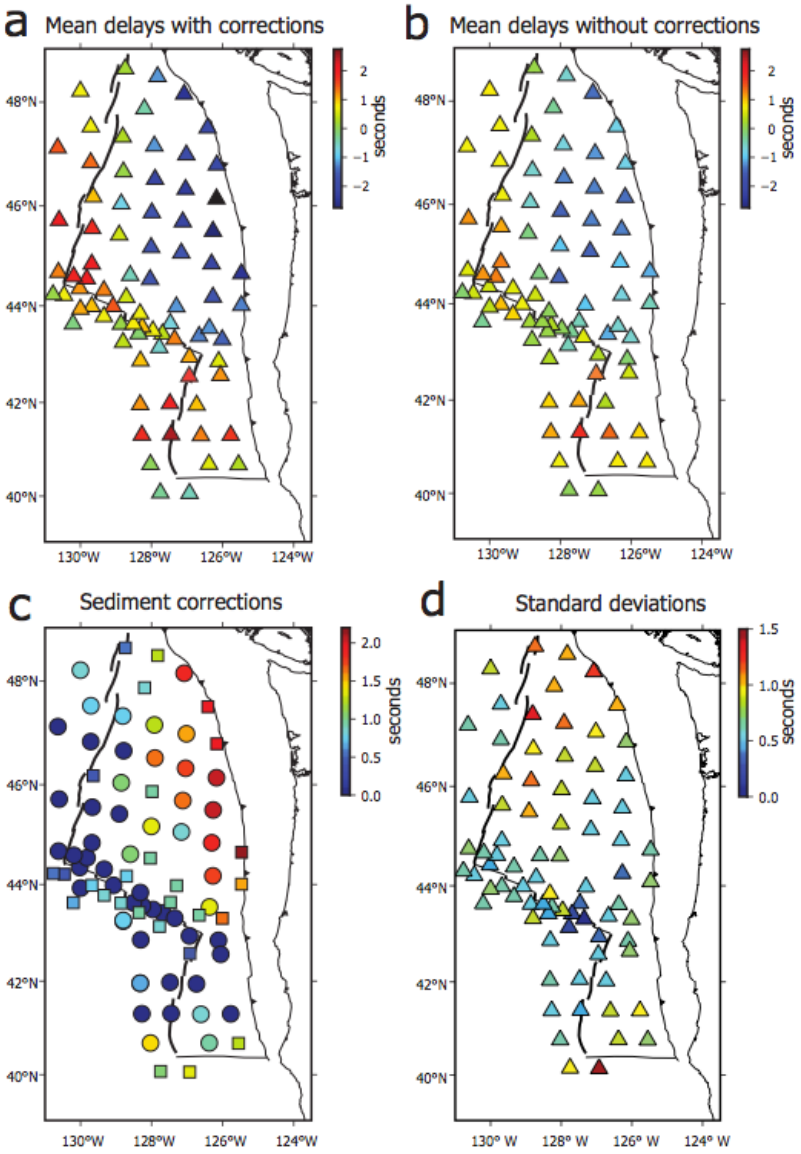

Figure 5. Summary of the delay times. a) Mean delay times in seconds recorded at each station after applying event statics and sediment corrections. b) Mean delay times in seconds recorded at each station after applying only the event statics. The datasets in Figure 5a and 5b have been separately demeaned. c) One-way travel times through seafloor sediments at each station in seconds, which were subtracted from the measured delay times for Figure 5a. Circles are stations where the method of *Ruan et al.* [2014] was used, squares are stations where interpolation was used. d) The standard deviation of the delay times in seconds recorded at each station (not the uncertainty of the observations).

Geographic patterns in the mean station delays are apparent in Figures 5a and b. In the JdF region, the mean delays are more positive (delayed arrival) at stations near the spreading center and become more negative (advanced arrival) where the plate is older; this pattern indicates an increase in upper mantle velocity with plate age. We note that this pattern is more pronounced in the set of delay times that include the sediment corrections. The mean delay times are also asymmetric about the JdF Ridge whether or not the sediment corrections are applied, with more delayed arrivals for sites on the Pacific plate, except toward the southern JdF Ridge where it intersects the Blanco transform fault. In the Gorda region, no clear relation between the mean delay times and the age of the crust is observed in either Figures 5a or b; this suggests a weaker relationship between plate age and upper mantle *Vs*. In the region of the Blanco and Mendocino transform faults, the mean station delays vary abruptly near the ridge-transform intersections (RTI), with more positive delays where the crust is younger. We do not observe a region of more positive delays near the Cascadia Depression. Curiously, the most negative delays are on the oldest sections of the JdF plate, despite the presence of older lithosphere south of both the JdF-Blanco RTI and the Mendocino Transform fault (Figure 1b); this is true for delays with and without sediment thickness corrections.

4.2 Tomographic Model

Our preferred tomographic results are shown in Figures 6 and 7. To construct our preferred model, we inverted sediment corrected delay times for mantle structure and damped station terms. We prefer this approach because the

sediment corrections account for known structure that cannot be resolved by teleseismic delays, and the damped station statics account for uncertainties in sediment corrections, instrumental clock errors, or the seismic velocity of the oceanic crust. After conducting trial inversions, we chose to damp the stations statics to an RMS of 0.22 s (Figure S5 of the SI); when larger station terms are allowed, the statics develop long-wavelength trends that are due to mantle structure (see Supporting Information). The Supporting Information also shows tomographic results for delay times without sediment corrections, the structure introduced by sediment corrections, differing inversion parameters, and the effects of including OBSs with suspect timing.

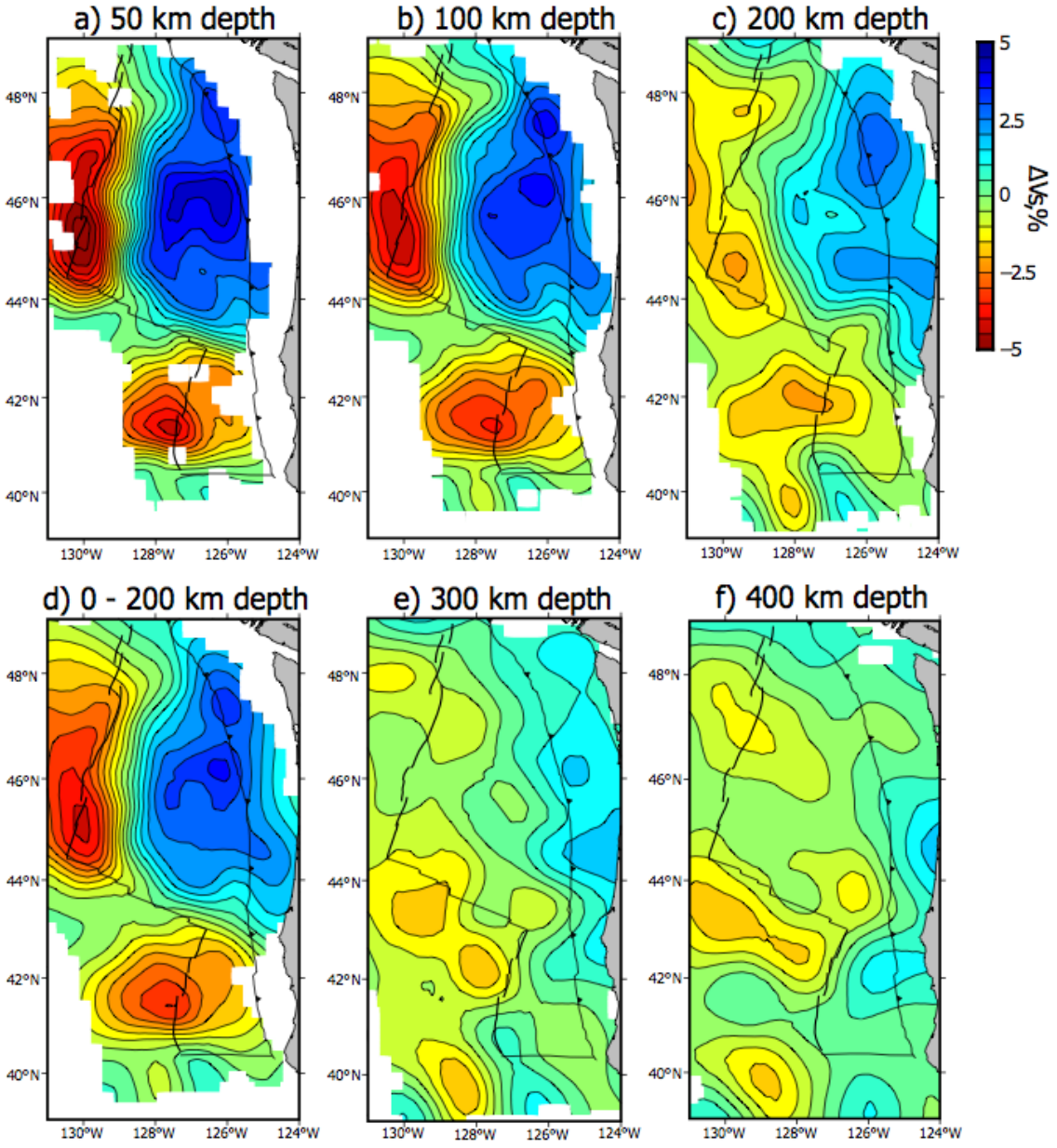

Figure 6. Horizontal cross sections through the tomographic model at a) 50 km depth, b) 100 km depth, c) 200 km depth, d) the average over 0 to 200 km depth, e) 300 km depth, and f) 400 km depth. The images are masked where there is no ray path coverage.

Figure 6 shows that in the upper 200 km significant variations in shear wave velocities are observed throughout the study area. Overall, anomalies vary from approximately -5% to 5% (Figure 6a-d), comparable to the total variation in the

upper 200 km beneath the entire United States [*Schmandt and Lin*, 2014]. Without sediment corrections, the range of velocity anomalies is less, -3% to 3% (Figure S7 of the SI), but still considerable. At 200 km depth, the overall magnitude of the velocity anomalies decreases to –2.5% to 2.5%. The largest negative and positive velocity perturbations in the region are located near the two ridges and the oldest portions of the JdF plate, respectively (Figure 6a-d). However, significant variations in velocity are observed beneath areas with similarly aged lithosphere, with generally lower velocities beneath the southern half of the JdF plate, relative to the north (Figure 6a-d, 7a,b). Remarkably, the highest velocities beneath the JdF plate exceed the velocities to the south of the Mendocino transform fault, which is the oldest lithosphere in the study area (Figure 1b). By 200 km depth, velocities are higher beneath the central region of the JdF Ridge (north of Axial Seamount) than elsewhere along the ridge, with the possible exception of a high velocity anomaly that is at the edge of the study area to the north (Figure 6c). To the east of the Cascadia megathrust, *Vs* begins to decrease; however, this occurs at the edge of the study area and is not well constrained by our results.

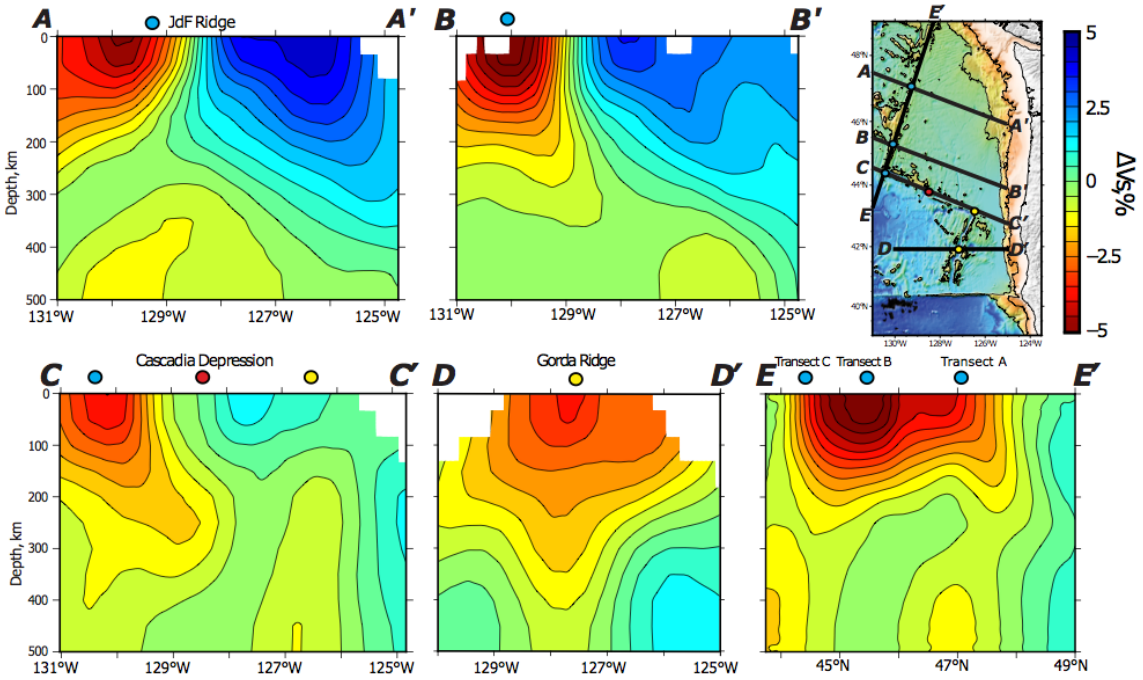

Figure 7. Vertical cross sections through the tomographic model. The images are masked where there is no ray path coverage. The locations of select features are indicated at the top of the plots. a) Cross section across the northern JdF plate. b) Cross section across the southern JdF plate. c) Cross section along the Blanco transform. d) Cross section across the Gorda Ridge. e) Cross section along the JdF Ridge. The map in the upper right shows the locations of the cross sections.

The velocity anomalies beneath the JdF Ridge are not uniform or symmetric. Where we have good resolution, anomalously low velocities are observed farther to the west of the JdF Ridge than to the east, indicating an asymmetric anomaly beneath the spreading center. This is particularly evident north of Axial Seamount (~46˚N); for example, Figure 8 shows that *Vs* at ~4 Myr old crust is up to 3% lower on the western flanks of the JdF Ridge than to the east, which is large in comparison to an asymmetry of 1-2% in the upper 200 km of the mantle near the southern East Pacific Rise [*Hammond and Toomey*, 2003]. South of Axial Seamount anomalously low velocities extend farther to the east of the ridge axis than to the north (Figures

6a and b, and 7a and b), particularly near the JdF-Blanco RTI. On the Pacific side of the JdF Ridge south of Axial seamount, *Vs* does not appear to be as asymmetric as to the north; however, due to a lack of instruments on the Pacific plate, we cannot fully assess the degree of asymmetry in this region. Using surface wave data from Cascadia Initiative stations, *Bell et al.* [2016] also reported an asymmetric low-velocity anomaly in this region. For the results of *Bell et al.* [2016], the degree of asymmetry about the southern JdF Ridge is reduced if the lateral smoothing constraint is relaxed and the velocity anomalies then appear more similar to the results presented here [S. Bell and D. Forsyth, personal communication, 2017]. Along the northern JdF Ridge — including the region of the Endeavour segment and south of the Sovanco transform — the amplitude of the low-velocity anomaly decreases and again extends farther to the east of the ridge axis than beneath the central section of the JdF Ridge. This region is associated with a diffuse plate boundary [*Dziak*, 2006] near the southern limits of the Explorer plate (Figure 1a).

Near the Gorda Ridge, *Vs* is generally low, and does not increase with distance from the spreading center as clearly as near the JdF Ridge (Figure 6a-d). Velocities are asymmetric beneath the Gorda Ridge (Figure 8), with lower velocities imaged beneath the Pacific plate, but in contrast to the JdF Ridge the degree of asymmetry is at most 1%, and is only apparent in the sediment-corrected results (Figure S7 of the SI). We observe a north to south trend in velocities that correlates with the southward decrease in spreading rate along the Gorda Ridge. *Bell et al.* [2016] also observed less asymmetry beneath the Gorda than JdF Ridge and a north to south trend in *Vs*, though at depths shallower than 55 km they observed higher *Vs*

beneath the Gorda than JdF Ridge. Velocities are low in our model within the whole region bounded by the Blanco and Mendocino transform faults east of 129°W and increase rapidly across the transform faults. We do not observe a change in *Vs* in the northeastern corner of the Gorda region, where *Bodmer et al.* [2015] inferred that mantle flow changes from being driven by absolute plate motion to the relative motion of the JdF and Pacific plates.

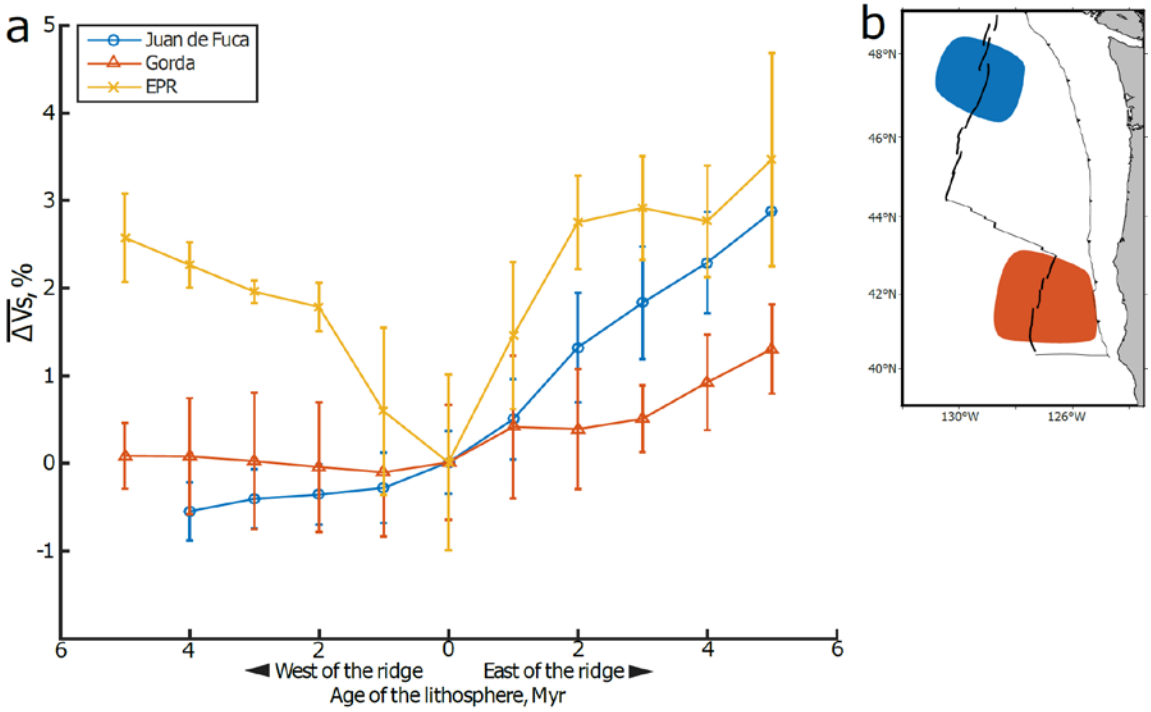

Figure 8. a) Shear-wave velocity anomalies as a function of the age of the lithosphere to the east and west of the JdF Ridge (blue), the Gorda Ridge (orange), and the East Pacific Rise (yellow) averaged over the upper 200 km. Each profile was set to 0% at an age of 0 Myr. The vertical bars show the standard deviation, not the uncertainty, of the velocity anomaly at a given age. b) Map showing the regions where velocities were taken from for the JdF (blue) and Gorda (orange) Ridges.

We observe distinct patterns of velocity anomalies along the strike of the Blanco transform fault. In the upper 200 km, *Vs* along the transform fault is average or slightly low for the region. Velocities are lowest near the JdF Ridge, higher near

the Gorda Ridge, and highest beneath the center of the transform fault and the Cascadia Depression. Lateral variations in velocity are pronounced near each RTI in the upper 200 km of the model, with velocities increasing in the ridge parallel direction toward the older lithosphere. At each RTI, the velocities beneath the older lithosphere are lower than those observed beneath similarly aged lithosphere of the JdF plate. Relative to the direction of ridge migration, two RTIs (JdF-Blanco and Gorda-Mendocino) are leading and one RTI (Gorda-Blanco) is trailing [*Carbotte et al.*, 2004]. The velocity anomalies imaged near the RTIs do not clearly correlate with the direction of ridge migration.

4.3 Model Resolution

The rows of the resolution matrix [*Backus and Gilbert*, 1968; *Jackson*, 1972] and inversions of synthetic data demonstrates the resolving capabilities of our study. Because the number of model parameters exceeds the number of independent data, individual parameters cannot be uniquely resolved. Instead, weighted averages of model parameters are resolved, with the weights given by the resolution matrix. Since our inversion is regularized with off-diagonal elements of a covariance matrix (see *Toomey et al.* [1994] for details), we use the equations of *Vasco and Johnson* [2003] to calculate the resolution matrix after singular value decomposition with the partial-derivative matrix from the final iteration. This approach allows us to identify how well our inversion can resolve an individual model parameter.

Figure 9 shows examples of averaging kernels for our study. Horizontal resolution (Figures 9 a-d) was evaluated by normalizing the off-diagonal elements

of the resolution matrix by the corresponding diagonal elements and contouring the normalized values at 0.5 and 0.25. Vertical resolution (Figures 9e-h) was estimated by averaging the values of the resolution matrix at different depths within the region where the normalized, horizontal resolution was greater than 0.25, and renormalizing the resulting profile. At 100 km depth, the lateral dimension of the averaging kernel varies from 70 to 150 km (Figure 9a), and increases to 100 to 200 km at 300 km depth (Figure 9b). Models parameters are not independent within the upper 200 km (Figure 9e-h), and model parameters at 300 km depth depend on those from approximately 200-400 km depth (Figure 9f). Horizontal resolution is to first approximation limited by station spacing.

Figure 10 shows an inversion of synthetic data predicted for a model with two layers of regularly spaced anomalies at 50-100 and 250-300 km depth; inversion parameters are the same as the preferred model. The sign of the anomalies changes every 100 and 150 km in the upper and lower layer, respectively. In both depth intervals, the inversion recovers lateral variations well (Figure 10 a-c) and overestimates the depth extent of the anomalies (Figure 10g). When the recovered anomalies are averaged over the upper 200 km of the model space, the amplitudes better approximate the input values (Figure 10c and d). The Supporting Information shows results for the same pattern of anomalies with even station and event coverage to demonstrate that resolution is primarily limited by the available ray paths.

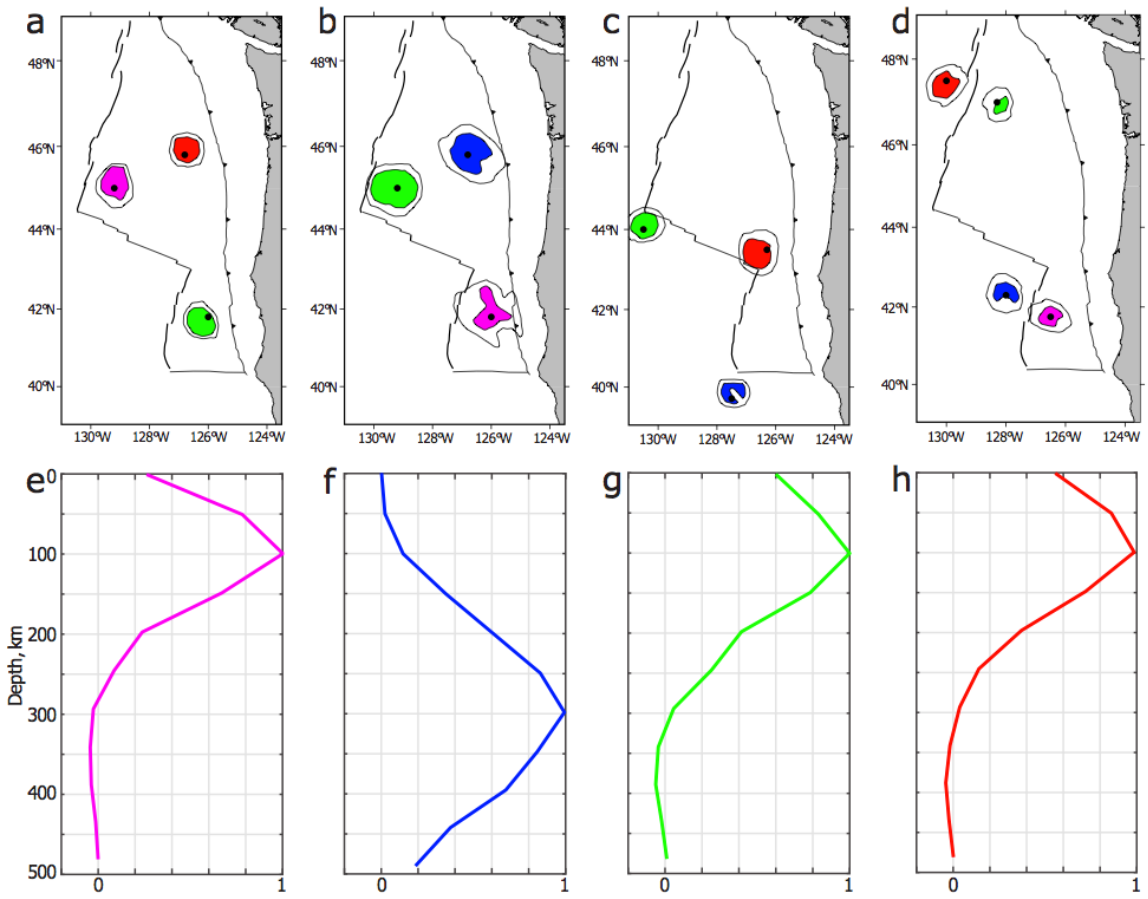

Figure 9. Examples of Backus-Gilbert averaging kernels. (Top row: a, b, c, and d). Averaging kernels for chosen model parameters in map view. The inner and outer contours show the 0.5 and 0.25 levels, respectively, for kernels normalized to 1. Black circles show the location of the model parameter. a) Three parameters at 100 km depth throughout the study area. b) Three model parameters at the same location as in a) but at 300 km depth. c) Three parameters near ridge-transform intersections at 100 km depth. d) Parameters on each side of the JdF and Gorda Ridges at 100 km depth. (Bottom row: e, f, g, and h) Line plots of averaging kernels against depth for the model parameter with the matching color in the map directly above. See text for discussion.

We use the resolution matrix and results of synthetic inversions to ascertain what features of our model may be reliably interpreted. Figures 9c and d show lateral averaging kernels near the 3 RTIs and to either side of the JdF and Gorda ridges, respectively. For the RTIs, model parameters beneath the older plate are independent of all model parameters beneath the ridges, confirming that the low

velocities observed in these regions are resolved independently from ridge structure. Where the spreading centers are encompassed by OBSs, Figure 9d shows that structure to either side of the ridge is independently resolved; this demonstrates that the asymmetric structure imaged near the JdF and Gorda Ridges is robust. Resolution tests also indicate that sharp, vertical contrasts in *Vs* will be averaged laterally, producing gradients with a full width of approximately 75 km. We thus estimate that the region of low *Vs* beneath the JdF Ridge (Figures 6 and 7) could be as narrow as 100 km wide if the actual transition to higher *Vs* is a sharp, vertical boundary (Section 6 of the SI).

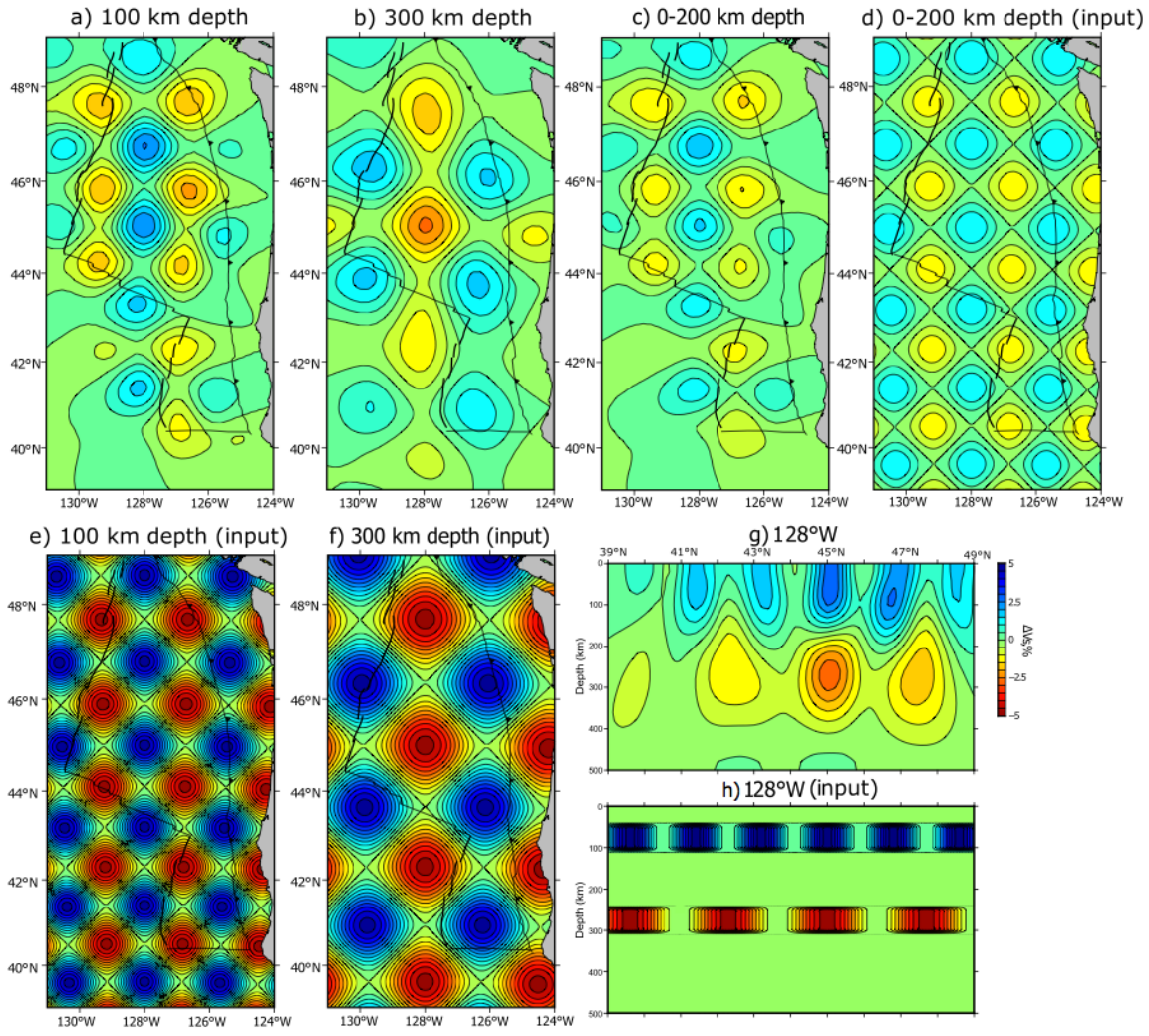

Figure 10. Inversion of a synthetic data set generated for a model with a regular pattern of anomalies. The recovered model is shown at 100 km depth (a), 300 km depth (b), averaged over the upper 200 km (c), and along longitude 128°W (g). Anomalies from the starting model are shown for the same regions in panels d, e, f, and h.

The data require that structure extends to depths of at least 200 km. For a model domain that is 500 km deep (Figures 6 and 7), the final RMS misfit of the data is 0.43 s. When anomalies are restricted to depths above 100, 200, or 300 km, the RMS misfit increases to 0.51 s, 0.46 s, and 0.44 s, respectively. After converting the misfits to a $\chi 2$ distribution, we used an *F*-test to find if the degraded fits to the data

by the squeezed models are statistically significant. We find *p*-values for the extension of the model domain below 100, 200, and 300 km depth of 0.01, 0.15, and 0.25, respectively, and conclude that structure must extend to depths of at least 200 km. At 300 and 400 km depth, the largest velocity anomalies are generally near the edges of the model domain and are of low amplitude. While our inversion can theoretically recover velocity anomalies at these depths (Figure 10), the details of the velocity structure below 200 km are poorly constrained by our results.

5. Discussion

Our tomographic results provide new insights to variations in oceanic upper mantle structure with plate age and near tectonic boundaries, including spreading centers, ridge-transform intersections, transform faults, and the Cascadia subduction zone. We use our results to infer physical properties of the upper mantle and then discuss the implications for geodynamic processes.

5.1 Physical Properties

Figure 11a shows velocity anomalies by plate age for three spreading centers — the JdF Ridge, Gorda Ridge, and East Pacific Rise (EPR) — as well as predictions for half-space cooling models. The EPR result is from *Hammond and Toomey* [2003; see their Figure 12b]. For each spreading center the velocity anomalies are averaged about the ridge axis to remove asymmetries. The velocity anomalies are averaged vertically over the upper 200 km and at 1 Myr intervals, using bin widths of 1 Myr; ages for the JdF and Gorda plates were estimated by linearly interpolating the isochron data of *Wilson* [1993] (Figure 1b). For each curve the velocity anomaly at 0 Myr is set to zero so that we can assess age-dependent variations. The

temperatures of the half-space cooling model were calculated assuming a mantle potential temperature of 1623 K and a seafloor temperature of 273 K [*Turcotte and Schubert*, 2002; *Stixrude and Lithgow-Bertelloni,* 2005; *Harmon et al.*, 2009].

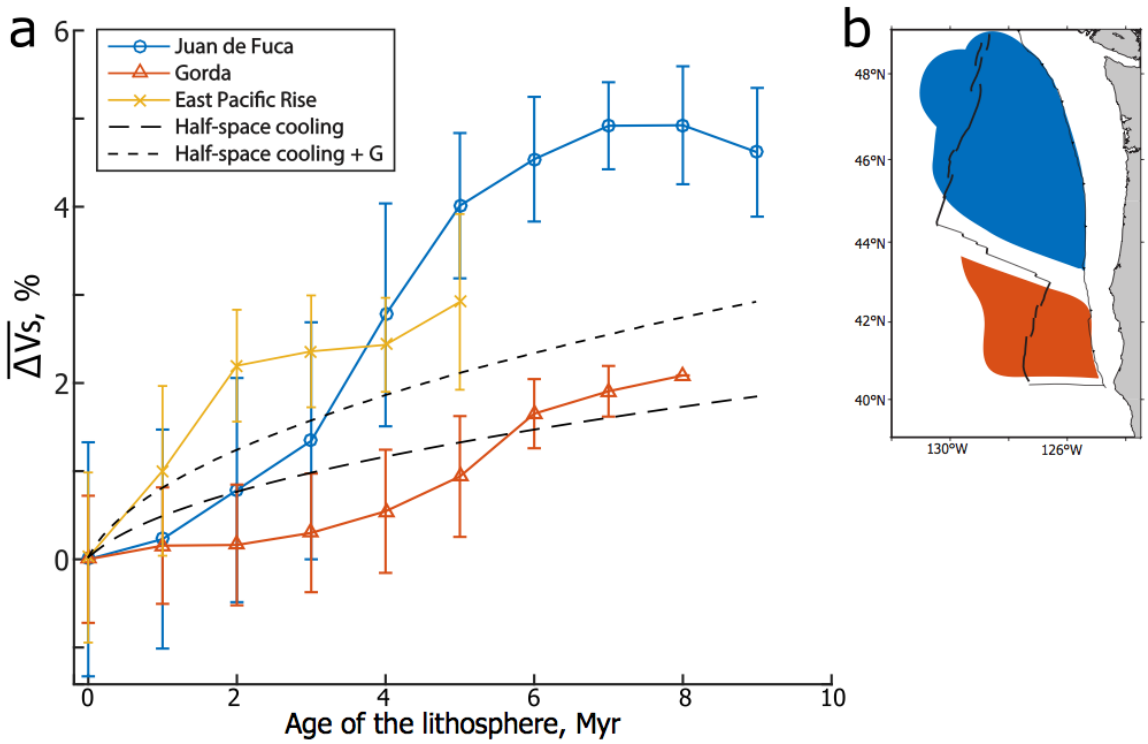

Figure 11. Trends of *Vs* anomalies averaged over the upper 200 km against the age of the lithosphere. a) Plots of velocity against age for the JdF region (blue), Gorda region (orange), the East Pacific Rise (yellow), and a half-space cooling models (black and dashed). Each profile was set to 0% at an age of 0 Myr. Vertical bars show the standard deviation, not the uncertainty, of the velocity anomalies at a given age. b) Map showing the regions where the velocities were taken from in a) for the JdF (blue) and Gorda (orange) region.

The results for both the JdF Ridge and the EPR show systematic increases in upper mantle velocities with plate age that are too large to be explained by variations in temperature due to lithospheric cooling (Figure 11a). Moreover, the velocities beneath the JdF plate continue to rise rapidly to 4 to 6 Myr, as opposed to leveling off between 2 to 4 Myr near the EPR. Beneath the JdF plate, the increase in

seismic velocity with age is greater than that observed in larger scale studies, which typically have poorer lateral resolution [*Nishmura and Forsyth*, 1989; *Nettles and Dziwonski*, 2008; *James et al.*, 2014]. For the Gorda region the age dependence of velocities is less apparent; the Gorda anomalies are discussed separately below.

Since cooling of the lithosphere alone cannot explain our results, we considered the effects of conductive cooling on the depth to a seismic G discontinuity. The G discontinuity is a generic term for a decrease in seismic velocity with increasing depth beneath oceanic lithosphere, and variations in the depth to such a discontinuity will impart a teleseismic delay time. While an age-dependent discontinuity may not exist beneath young oceanic lithosphere, one could be caused by the presence of melt [e.g., *Kawakatsu et al.*, 2009; *Holtzman et al*., 2016] or by a thermally controlled anelastic process [*Karato,* 2012], and such a discontinuity has been previously proposed to exist beneath the JdF plate [*Kumar and Kawakatsu,* 2011]. We assume an ad hoc 8% decrease in velocity at depths greater than the 1100 K isotherm [*Rychert and Shearer,* 2011] of the half-space cooling model. This hypothesis mimics a G discontinuity at the base of the thermal lithosphere, as suggested by onshore studies of the recently subducted JdF [*Kumar and Kawakatsu*, 2009] and Gorda [*Liu et al*., 2012] plates. Including such a discontinuity increases the cumulative age-dependent increase in velocity to 3% for the upper 200 km, which is still significantly less than the observed increase in *Vs* for the JdF plate. Moreover, *Vs* increases most rapidly beneath 3 to 5 Myr old lithosphere, while both half-space cooling models predict that *Vs* should increase at a decreasing rate as the lithosphere ages. On the basis of these comparisons we conclude that thermal

evolution of oceanic lithosphere or its effects on the G discontinuity cannot explain mantle structure in the JdF region.

Our tomographic results require age-dependent variations in the physical properties of the asthenosphere. We discuss the likely effects of temperature, anelasticity, and melt fraction and conclude that the most likely explanation is age-dependent variations in the amount of partial melt. Assuming that variations in temperature occur between the 1100 K isotherm and 200 km depth, a 300 K contrast in temperature is required to explain the variations in *Vs* beneath the JdF plate, assuming a *Qs* of 50 [*Karato*, 1993]. If the anomalies are confined to shallower depths, then the required variations in temperature will be higher. *Qs* is likely higher than 50 [*Yang et al.*, 2007] and a higher *Qs* would increase the required temperature contrast. As the required temperature anomaly is greater than the range of temperature in all MORB and OIB sources [e.g., *Purtika,* 2005], we conclude that other mechanisms are required to explain our results.

A *Qs* anomaly that explains our results by an anelastic processes is also unlikely. We estimate the required variations in *Qs* to explain our results with the equations of *Anderson and Given*, [1982]. We assume that *Qs* reaches a maximum beneath the JdF plate where we observe the highest *Vs*, and then calculate the required reduction in *Qs* to explain the observed velocity anomalies. For maximum values of *Qs* of 50, 100, and 200, *Qs* beneath the JdF Ridge would need to reach minimum values of 13, 14, and 15, respectively. These values are dramatically lower than those inferred from observations beneath the East Pacific Rise and Southern

California, where *Qs* is estimated to be greater than 50 [*Yang et al.*, 2007; *Yang and Forsyth*, 2008].

We infer that variations in the melt fraction of the asthenosphere are required to explain our observations, a result consistent with those of previous surface wave studies [*Tian et al*, 2013; *Bell et al*., 2016]. To estimate lateral variations in melt fraction we first remove the predicted effects of the half-space cooling model and then assume the following: melt is uniformly distributed between the 1100 K isotherm and 200 km depth; 1% of retained melt reduces *Vs* by 8% [*Hammond and Humphreys*, 2000a]; and melt has a negligible effect on seismic attenuation [*Hammond and Humphreys*, 2000b]. Figure 12 shows a map of lateral variations in the melt fraction (as a percentage) of the asthenosphere in the upper 200 km that are consistent with these assumptions. If melt is retained in high aspect-ratio bands [*Holtzman et al.*, 2003; *Kawakatsu et al.*, 2009] or if melt influences *Qs* [*Faul et al.*, 2004; *McCarthy and Takei*, 2011; *Abers et al.*, 2014; *Holtzman*, 2016], then smaller variations in melt fraction are required; however, if melt is retained in triple-junction tubules at low melt fractions [*Hammond and Humphreys* 2000a] then larger variations are required. We also note that because we used an average of velocities in the upper 200 km of the mantle, greater melt fractions in narrower depth intervals are possible and our estimates are a minimum bound on the retained melt fraction. For example, in regions of mantle upwelling we expect relatively higher melt fractions above the anhydrous solidus due to increased productivity.

Figure 12 shows that the inferred, depth-averaged asthenospheric melt fraction varies throughout the study area. We attribute the higher average melt fractions near the JdF and Gorda Ridges to regions of increased melt production and retention. Beneath the Blanco transform fault and its bounding RTIs, the inferred asthenospheric melt fractions are generally less than that beneath the spreading centers, implying lower rates of melt production. Beneath the older JdF plate, melt fractions are less than near the ridges but not uniform, with the smallest melt fractions inferred between 45˚N and 47˚N. Given the uncertainties in our observations and imaging, regions where melt fraction is less than 0.1% may be melt free. Our results do not constrain structure east of the Cascadia deformation front (Figure 10a-c), thus we cannot determine if anomalously high melt fractions are present beneath the subducting JdF slab [*Hawley et al.*, 2016]. However, beneath the older Juan de Fuca plate, we question the existence a sub-slab melt anomaly east of deformation front in view of the low asthenospheric melt fractions.

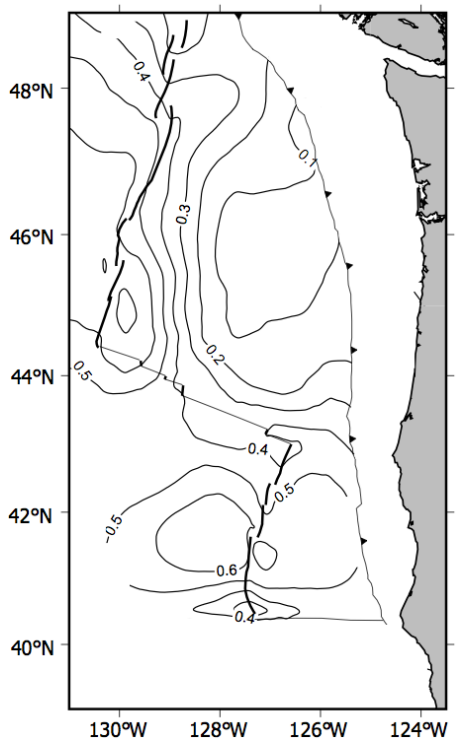

Figure 12. Contours of depth-averaged variations in melt fractions in the upper 200 km (in %). The same regions are masked as in Figure 6d, with the addition of the regions south of the Mendocino transform fault and east of the Cascadia megathrust. The calculation and associated uncertainties are described in the text.

Our tomographic results are consistent with relatively low, but non-zero melt fractions, at depths near 200 km. A 3% contrast in *Vs* (Figure 6c), for example, requires unrealistically large temperature anomalies of 130 and 260 K for *Qs* of 50 and 200, respectively [*Karato*, 1993]. The *Vs* anomalies may indicate the presence of carbonatitic melts [*Dasgupta and Hirschmann*, 2006; *Dasgupta et al.,* 2013], with retained melt fractions on the order of ~0.1% or less [*Hirschmann*, 2010]. We consider two possible distributions of melt near 200 km depth. First, a 3% change in *Vs* could correspond to a ~0.3% contrast in melt fraction if melt is distributed in elongate inclusions at grain boundaries [*Faul et al.*, 1994; *Hammond and Humphreys*,

2000a]. However, smaller melt fractions are thought to be present within the carbonatitic melting regime [*Hirschmann*, 2010]. A second possibility is that the deep melt fractions are as small as 0.01% and are distributed in a connected network of thin films along grain boundaries, which may reduce *Vs* relative to melt-free rock by ~5% [*Holtzman*, 2016]. Thus, the deep *Vs* anomalies either reflect the presence of variable fractions of melt, or regions of melt-free and melt-bearing rock. Seismic and conductivity anomalies beneath the EPR and Galápagos Archipelago have been attributed to deep melting [*Hammond and Toomey*, 2003; *Key et al*., 2013; *Villagómez et al.,* 2014], suggesting that carbonatitic melts are commonplace in regions of mantle upwelling near 200 km depth.

5.2 Geodynamic Processes

Here we discuss how variations in upper mantle melt fraction can occur in our study area and their relations to geodynamic processes. To emphasize relations between our tomographic results, estimates of melt distribution, and tectonic features, Figure 13 shows the absolute value of the gradient of the *Vs* anomalies in the upper 200 km of the mantle; a value larger than 0.03 %/km (bold contour in Figure 13) outlines regions of large lateral velocity gradients. We expect the largest and most rapid variations to occur within the dry melting regime because melt productivity is an order of magnitude lower below than above the dry solidus [*Hirth and Kohlstedt*, 1996] and because of the likelihood that mantle upwelling is more broadly distributed at deeper depths. Processes that can cause lateral variations in melt content include melt production during mantle upwelling, melt freezing during mantle downwelling, and variable rates of melt transport. In the following sections,

we discuss how such processes can give rise to the inferred variations in melt fractions within the different tectonic settings of our study area. We do not consider melt freezing at the base of the thermal lithosphere, since the deepening of a G discontinuity cannot explain either the range or lateral gradients of the velocity anomalies.

5.2.1 Juan de Fuca Ridge and Plate

Figure 13 shows that near the JdF Ridge, the largest lateral gradients are located east of the spreading center. We attribute the largest gradients in velocity to melt freezing due to mantle downwelling. Our reasoning is as follows: if only melt production and transport rates varied — without freezing — then melt fraction would decrease gradually with distance from a spreading center since melt fractions below ~1% do not readily segregate from the mantle [*Spiegelman*, 1996; *Faul*, 2000]. In this scenario, abrupt gradients in velocity structure would not develop. We note that both the location and magnitude of the gradient is not uniform near the JdF Ridge. The largest gradients are closer to the spreading center to the north than to the south of Axial Seamount (~46˚N), consistent with the westward offset of *Vs* anomalies north of Axial Seamount. Farther to the north, and near the Endeavour segment (~48˚N), the gradients east of the ridge axis are both lower in magnitude and farther from the ridge axis, which suggests that downwelling is not present; synthetic tests confirm that we would detect a large gradient in this region if it were present (Figure S14 of the Supporting Information).

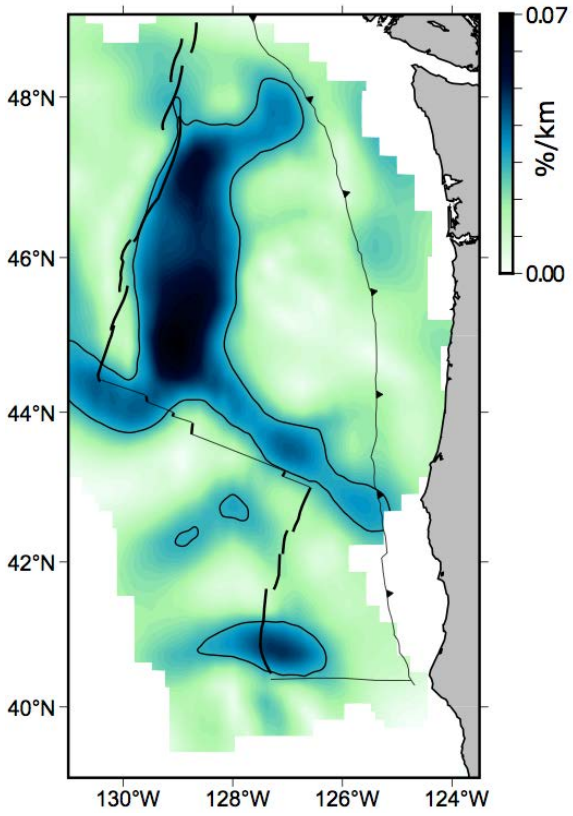

Figure 13. Magnitude of the gradient of the *Vs* anomalies shown in Figure 6d. The bold lines show the 0.03 %/km contour. The same regions are masked as in Figure 6b. The calculation is described in the text.

In Figure 14 we illustrate a first-approximation, two-dimensional scenario for mantle flow and melting beneath the central JdF Ridge that is consistent with our tomographic results, geodynamic predictions, and previous work in the region. Characteristics of this simplified scenario include asymmetric mantle flow due to northwest migration of the JdF Ridge, asymmetric melting that extends farther west of the spreading center due to an entrained thermal anomaly, and mantle downwelling with melt freezing beneath the eastern flank. Geodynamic studies predict that ridge migration alone does not give rise to significant asymmetric melting [*Toomey et al.*, 2002; *Conder et al.*, 2002; *Katz*, 2010]. However, a ridge

migrating over a thermal anomaly does result in asymmetric melting [*Toomey et al.,* 2002; *Conder et al.*, 2002], particularly if there is a component of dynamic upwelling, which enhances mantle downwelling and melt freezing beneath the trailing flank. Assuming that the temperature of the melt is near the pressure dependent solidus, the melt fraction will reach zero with less than 10 km of downwelling [*Katz*, 2010]. Dynamic upwelling and off-axis downwelling are triggered when the viscosity of the mantle is low enough for buoyancy forces — due to the composition, temperature, or retained melt fraction of the mantle — to contribute to mantle flow [*Scott and Stevenson*, 1989; *Jha et al.*, 1994; *Katz*, 2010].

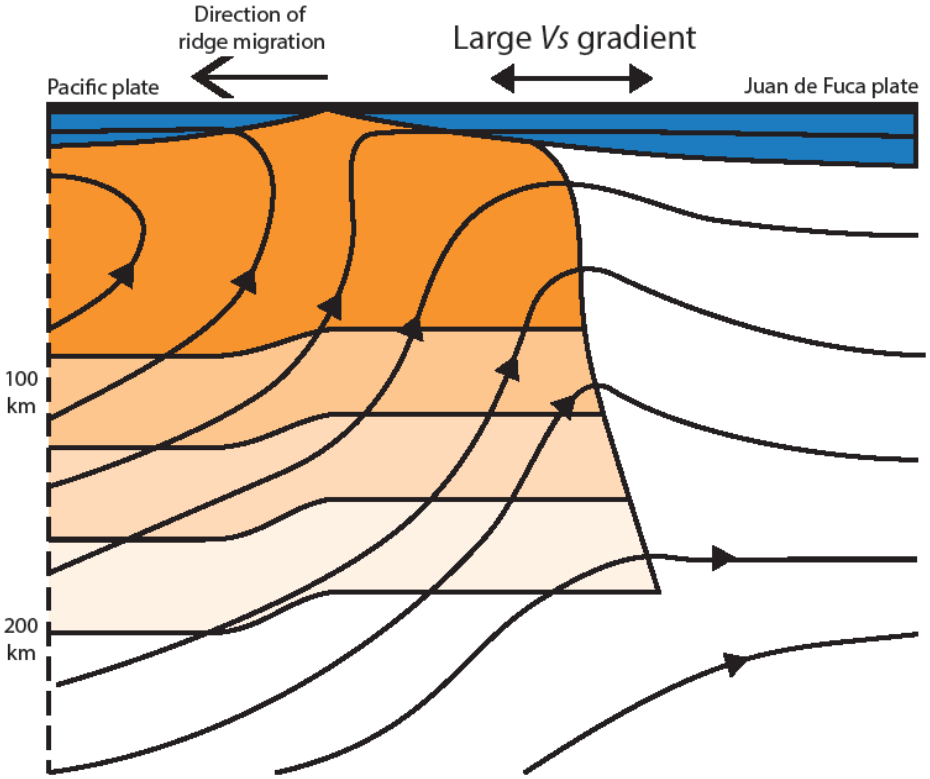

Figure 14. Scenario for upwelling and melting beneath the JdF Ridge. Melt fractions are qualitatively shown in shades of orange, the lithosphere in blue, streamlines by black lines with arrows, the edge of station coverage by the vertical dashed line, and approximate depths are given on the left. See text for discussion.

We attribute the primary characteristics of mantle structure near the JdF Ridge to a modest thermal anomaly beneath the Pacific plate, in conjunction with ridge migration and dynamic upwelling. A likely source of this thermal anomaly are the hotspots in the northeastern Pacific; for example, the Cobb-Eickelburg hotspot is estimated to have an excess temperature of at least 30 to 40°K [*Rhodes et al.*, 1990; *Hooft and Detrick*, 1995]. We note that if buoyancy forces do not contribute to mantle flow, then either a thermal anomaly on the order of 100°K orpressure driven flow in the asthenosphere is required to explain the mantle velocity structure [e.g., *Toomey et al.*, 2002; *Conder et al.*, 2002]; we consider such scenarios for this region unlikely.

Our preferred interpretation for the mantle structure of the central and southern JdF Ridge is that the thermal anomaly responsible for the asymmetry is preferentially located north of Axial Seamount and west of the ridge axis. To support this view, in Figure 15 we show the difference between *Vs* over the upper 200 km along transects 75 km east of and directly beneath the JdF Ridge. The eastwards increase in *Vs* (Figure 13) begins closest to the ridge axis near 47˚N and farthest from the ridge axis south of 45˚N. This is consistent with the largest westward offset in the mantle low-velocity anomaly occurring near 47˚N and suggests that thermally-induced dynamic upwelling is stronger in this region. While we image a more symmetric pattern of anomalies about the southern than central ridge axis, only one OBS was deployed west of the southern JdF Ridge. However, the asymmetry of mantle Bouguer anomalies (MBA) — which constrains mantle density anomalies since it accounts for variations in seismically measured crustal thickness

— from three ridge-perpendicular transects are consistent with our interpretation (dashed lines and text in Figure 15, [*Marjanović et al.*, 2011]). For example, mass deficits in the mantle are most asymmetric at 47˚N, with lower densities to the west of the ridge (positive ΔMBA in Figure 15), and are more ridge-centered at 45˚N with some eastward offset (negative ΔMBA). Intriguingly, $^{3}He/^{4}He$ ratios vary with the asymmetry of mantle structure (blue circles in Figure 15, [*Lupton et al.,* 1993]). This trend, which negatively correlates with $^{87}Sr/^{86}Sr$, is consistent with the presence of a modest thermal anomaly where $^{3}He/^{4}He$ ratios are higher [*Graham et al*., 2001; *Graham et al*., 2014]. One issue with our interpretation is that the crust is moderately thicker along the southern JdF Ridge [*Carbotte et al.*, 2008], and it is commonly assumed that crustal thickness is related to mantle temperature. In some geodynamic models, crustal thickness decreases as the strength of dynamic upwelling increases and the melt-producing region narrows [*Katz,* 2010]. Our results may be consistent with this prediction, since we observe both a wider and stronger low velocity zone beneath the southern JdF Ridge.

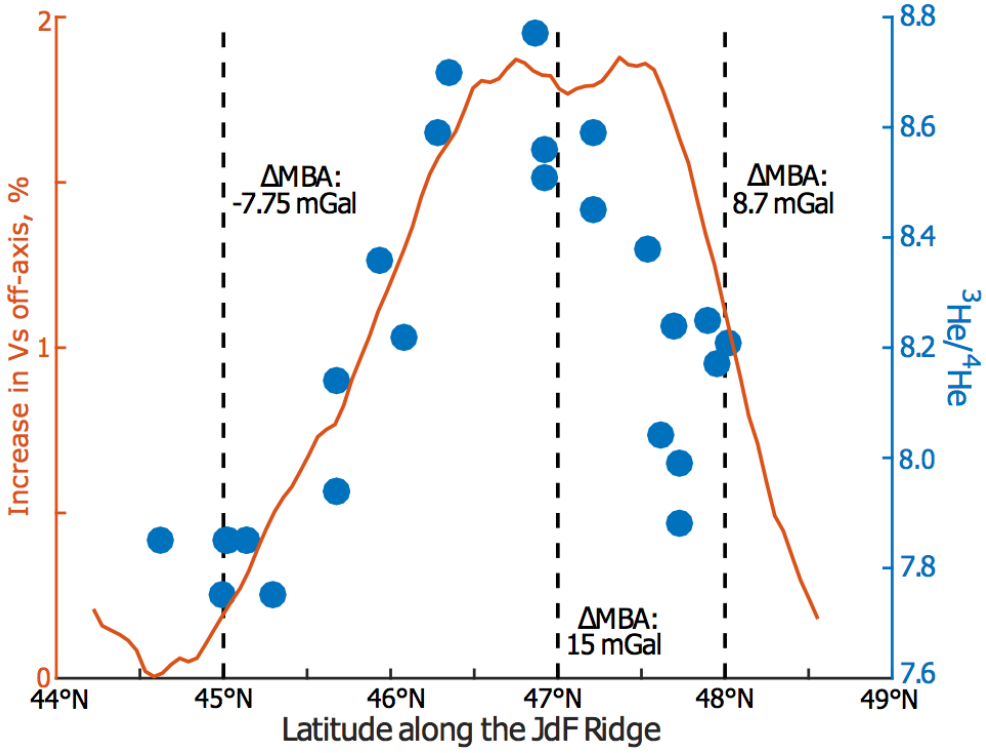

Figure 15. Comparison between *Vs* anomalies (orange), the asymmetry of mantle Bouguer anomalies (ΔMBA, black, dashed lines and text, from *Marjanović et al.*, [2011]), and helium ratios (blue, from *Lupton et al.,* [1993]) along the JdF Ridge. The orange line shows the difference between *Vs* anomalies averaged over the top 200 km of the mantle along transects 75 km east and directly on the JdF Ridge; positive values indicate increasing *Vs* to the east of the ridge axis. ΔMBA is the difference between gravity anomalies 50 km east and west of the JdF Ridge from three ridge-perpendicular transects; positive values indicate a greater mass deficit to the west of the ridge.

Farther north along the Juan de Fuca Ridge, and beneath the Explorer deformation zone, we infer that mantle upwelling is relatively broad and occurs at a reduced rate. This region is characterized by a decreased magnitude of the low-velocity anomaly (Figure 6), reduced melt fractions (Figure 12), and *Vs* gradients that are both lower in magnitude and farther off axis than to the south (Figure 13). This suggests slower rates of mantle upwelling and that mantle downwelling is

weaker or not occurring to the east of the spreading center. Moreover, the helium ratios and asymmetry in gravity anomalies about the ridge axis also decrease in this region (Figure 15). These trends to reduced anomalies north of the Cobb Offset all occur near a diffuse plate boundary (Figure 1) associated with the Explorer plate and the region south of the Sovanco transform fault [*Dziak,* 2006]. This region of the JdF Ridge has undergone significant deformation and reorganization in the last 3.5 Myr [*Riddihough*, 1984; *Wilson et al.*, 1984; *Karsten et al.*, 1986; *Braunmiller and Nábělek*, 2002]. As deformation has progressed, basalts of more variable and enriched compositions are being erupted along the Endeavour segment that may originate from a small degree of melting of an enriched component that reaches the surface without mixing with more depleted melts during ascent [*Karsten et al.,* 1990; *Goldstein et al.*, 1991; *Cousens et al.*, 1995; *Sours-Page et al.,* 1999]. Based on these observations, we infer that beneath the diffuse plate boundary the rate of mantle upwelling and the in situ melt fractions have decreased, and the region of mantle upwelling has broadened as mantle downwelling waned.

Our results are consistent with a region of nearly melt-free asthenosphere beneath the older portions of the JdF plate. As noted above, to explain the abrupt gradients in velocity we infer that melt freezing has occurred within the primary region of melt production due to mantle downwelling. Hence, the asthenosphere nearest to the Cascadia subduction zone at latitudes between approximately 45˚N and 48˚N may be largely melt free. While our results only constrain relative variations in velocity, *Bell et al.* [2016] likewise inferred a nearly melt-free asthenosphere in this region from surface wave tomography. We do not resolve

structure east of the Cascadia megathrust (Figure 10), thus we cannot constrain if melt fractions are higher beneath the subducting plate [e.g. *Hawley et al.*, 2016].

5.2.2 Ridge-Transform-Ridge Plate Boundaries

We infer that mantle upwelling and melt production occurs along the full length of Blanco transform fault in a broad and sinuous pattern. The relatively low velocities imaged throughout the transform domain (Figure 6a-d) and the inferred melt fractions (Figure 12) support this view. Our interpretation is also consistent with the inference from petrology that some melt is produced beneath the Pacific plate near Blanco transform fault [*Gaetani et al.*, 1998]. We further note that the lowest *Vs* anomalies near the JdF-Blanco RTI do not follow the ridge-transform-ridge geometry observed on the surface. Instead, low-velocity anomalies elongate along the strike of the Blanco transform fault. For example, anomalies near the southern JdF Ridge extend towards the east at shallow depths (Figure 6a and b) and the discord between geometry of the plate boundaries and the low *Vs* anomalies becomes more pronounced near 200 km depth (Figure 6c).

The sinuous character of the velocity structure beneath the Blanco transform is consistent with predictions of dynamic models of mantle flow. Passive flow models predict that upwelling and melt production will be centered beneath the spreading centers with a gradual reduction in upwelling toward an RTI and continued upwelling beyond the ridge end. The distribution of upwelling at mantle depths in passive flow models largely maintains the geometry of the ridge-transform-ridge system [*Phipps Morgan and Forsyth*, 1988, Figure 6]. In contrast, for dynamic flow models the mantle flow displays a smoother geometry than the

surface offsets, resulting in a more sinuous pattern that is asymmetric about the ridge axis and weaker within approximately 100 km of the RTI [*Sparks et al*., 1993, Figure 4; *Magde et al*., 1997]. In concert with our interpretation for the asymmetry and *Vs* gradients of the JdF Ridge, we attribute the sinuous pattern of anomalies beneath the Blanco transform fault to the influence of dynamic upwelling beneath the ridge-transform-ridge system.

5.2.3 Gorda Ridge and Plate

The seismic structure of mantle beneath the Gorda Ridge and plate shows a strong association with the Gorda deformation zone that rivals that of seafloor spreading processes. South of the Blanco transform fault, variations in melt fractions are generally less than 0.2% (Figure 12) and appear unrelated to the Gorda Ridge or lithospheric age (Figure 11), which is in contrast to the structure beneath the JdF Ridge and plate. Instead, the clearest trend is an abrupt decrease in *Vs* from the central Gorda Ridge toward the south that terminates at the Escanaba Trough (Figure 6a-d). Results from surface wave tomography for the same region show a decrease in *Vs* toward the south at 55 km depth [*Bell et al.*, 2016]. However, this trend is not apparent in the surface wave results at shallower depths, suggesting that melt may be primarily retained at deeper depths than beneath the JdF Ridge. Results from *SKS* splitting are consistent with the view that seafloor spreading processes are being overwhelmed by diffuse deformation. Fast polarization directions become more closely aligned with the relative Pacific-JdF plate motion from north to south and, like the *Vs* anomalies, do not vary with distance from the ridge axis [*Bodmer et al.*, 2015]. Therefore, seismic velocity and anisotropy appear

to be better related to the deformation of the southern Gorda plate than with spreading at the Gorda Ridge. We also do not observe evidence for mantle downwelling (Figure 13) and instead observe a continuous distribution of melt at longitudes nearest to the Cascadia subduction zone. Tomographic studies using onshore data also observe lower *Vs* anomalies underneath the slab south of 43˚N than farther north [e.g., *Schmandt and Humphreys*, 2010; *Xue and Allen*, 2010; *James et al*., 2011], which is consistent with the retention of melt farther east than our results can constrain (Figure 10).

We conclude that the dynamics of mantle flow beneath the diffuse plate boundaries of the Gorda and Explorer deformation zones are fundamentally different in comparison with that beneath the JdF Ridge and plate. The age-independence of seismic velocity and anisotropy across the Gorda Ridge and their association with the deformation of the Gorda plate suggests that the shear zone between the JdF and Pacific plates dominates mantle deformation over seafloor spreading. Similarly, the Endeavour segment of the JdF Ridge, at the southern edge of the Explorer deformation zone, also features gradual variations in *Vs* anomalies that are more similar to the tomographic results for the Gorda Ridge than to the large gradients along the JdF Ridge south of the Cobb Offset. Plate boundary reorganization around both the Gorda and Explorer Ridges results in a broad region of intraplate deformation, volcanism, and seismicity [*Wilson*, 1986; *Wilson*, 1989; *Chaytor et al.* 2004; *Karsten et al*, 1986; *Braunmiller and Nábělek*, 2002; *Dziak*, 2006], and is associated with the eruption of increasingly enriched basalts derived from smaller degrees of melting [*Karsten et al.*, 1990; *Davis et al.¸* 2008]. These

contrasting observations between the JdF Ridge and plate, and the adjacent deformation zones, suggests distinct patterns of mantle flow beneath discrete and diffuse plate boundaries. Dynamic upwelling and mantle downwelling occur in response to spreading at the JdF Ridge south of the Cobb Offset (Figure 14), while forces associated with the deformation zones appear to disrupt or even dominate over the influence of seafloor spreading and mantle buoyancy beneath the diffuse plate boundaries.

6. Conclusions

The Cascadia Initiative and Blanco transform experiments provide a novel opportunity to study the structure of the upper mantle beneath an entire tectonic plate. In this study, we have tomographically imaged shear-wave velocity anomalies in the upper mantle beneath the Juan de Fuca, Gorda, and Pacific plates using the relative arrival times of teleseismic *S* waves recorded on the transverse components of OBSs. The range of observed *Vs* anomalies requires variations in the retained melt fraction of the asthenosphere. We attribute large *Vs* anomalies beneath the JdF and Gorda Ridges to melt production shallower than the dry solidus and smaller *Vs* anomalies across the transform faults and at least as deep as 200 km to volatile-induced melting. Three lines of evidence suggest that dynamic upwelling —driven by the buoyancy of the mantle — occurs beneath the JdF Ridge. First, large gradients in *Vs* to the east of the JdF Ridge require melt freezing due to downwelling, which is predicted to occur in tandem with dynamic upwelling. Second, the asymmetry of the low *Vs* region beneath the JdF Ridge is most likely due to the interaction of a modest

thermal anomaly in the asthenosphere and dynamic upwelling. Third, the low *Vs* anomalies beneath the JdF-Blanco transform intersection display a smoother pattern than the surface offsets, as predicted by some models of dynamic upwelling. Distinct patterns of mantle flow are inferred beneath the diffuse plate boundaries of the Gorda and Explorer deformation zones from that beneath the discrete plate boundary of the JdF Ridge. We do not observe evidence for dynamic upwelling north of the Cobb Offset and beneath the Gorda Ridge, where the shear zone between the Pacific and JdF plates dominates mantle deformation over seafloor spreading.

7. Bridge

In Chapter III, mantle flow beneath the JdF Ridge was shown to be inconsistent with a passive response to the spreading of the JdF and Pacific plates. Rather, dynamic upwelling, driven by density variations of the upwelling asthenosphere in addition to plate spreading, is consistent with many features of the tomographic results. The physical state of the asthenosphere, therefore, must be considered when discussing mantle convection beneath the JdF Ridge. This style of upwelling is predicted by numerical models that assume the viscosity of the upper mantle is on the order of 10^{19} Pa s or less. These results open up the range of possible patterns of mantle flow in this region to those predicted by models for a low viscosity asthenosphere.

One predicted behavior for a low viscosity asthenosphere is lateral mantle flow driven by variations in density or pressure within the asthenosphere. Mantle flow may then be decoupled from the motion of the lithosphere. Observations of azimuthal anisotropy require simple shear of the asthenosphere and a near-horizontal fast axis requires some degree of lateral mantle flow. Studies of azimuthal anisotropy in the

oceanic asthenosphere have generally interpreted the such deformation of the upper mantle in terms of viscous coupling between the lithosphere and asthenosphere. In Chapter IV, this dissertation returns to the *S*-to-*p* receiver functions method to identify a discontinuity (L, or Lehmann) beneath the JdF plate that can only be attributed to a contrast in seismic anisotropy. The required fast propagation direction at the L discontinuity is not parallel to the motion of the JdF plate in a hotspot reference frame, and significant magnitudes of anisotropy are required at depths well separated from the base of the lithosphere. Therefore, mantle flow beneath the JdF plate, just as beneath the JdF Ridge, is not solely a consequence of the motion of the lithosphere, but that some component of dynamic flow must occur in the asthenosphere in response to pressure or density anomalies.

CHAPTER IV

FLOW IN THE OCEANIC ASTHENOSPHERE BENEATH THE JUAN DE FUCA PLATE: RESULTS FROM *S*-TO-*P* RECEIVER FUNCTIONS WITH CASCADIA INTIATIVE DATA

This chapter is in preparation for publication, and was written with advising and input from Douglas Toomey and Emilie Hooft.

1. Introduction

The velocities of the tectonic plates at the Earth's surface are well characterized, but the convective motion of the mantle is poorly understood. Beneath oceanic plates in particular, different observations have led to different views of mantle flow in the asthenosphere. Large scale studies of seismic anisotropy beneath fast moving plates generally infer that asthenospheric flow is parallel to the motion of the lithosphere in a hotspot reference frame [e.g. *Montagner and Tanimoto*, 1991; *Maggi et al.*, 2006; *Beghein et al.*, 2014]. Such observations have motivated models of the oceanic asthenosphere where mantle flow is driven by viscous coupling between the lithosphere and asthenosphere [e.g. *Tommasi*, 1998; *Podolefsky et al.*, 2004; *Conrad et al,* 2007; *Behn et al.*, 2009]. In this view, the asthenosphere primarily deforms as a passive response to the motion of the lithosphere.

However, the extent to which this passive response controls the oceanic asthenosphere is unclear. The alignment between the direction of absolute plate motion (APM) and the fast propagation direction of seismic waves in the asthenosphere degrades with decreasing spreading rate in global models, yet the magnitude of anisotropy in the asthenosphere is similar beneath fast and slow

moving plates [*Debayle and Ricard,* 2013; *Becker et al.,* 2014]. Observations with arrays of ocean-bottom seismometers (OBSs), which can resolve smaller scale features than inversions of global data, often observe a misalignment between current plate motions and the azimuth of seismic anisotropy [*Toomey et al.,* 2007; *Takei et al.,* 2013; *Bodmer et al.*, 2015; *Lin et al.*, 2016; *VanderBeek et al.*, 2016]. In addition to viscous coupling with the lithosphere, variations in density [*Haxby and Weissel*, 1986] or pressure [*Phipps Morgan et al.,*1995] within the asthenosphere provide addition driving mechanisms for mantle flow. Further geophysical constraints on the structure of the upper mantle are required to understand the competing roles of different boundary conditions on the deformation of the oceanic asthenosphere.

The Cascadia Initiative community experiment [*Toomey et al.*, 2014] provides a unique opportunity to study to the upper mantle using data from OBSs. Here, we use data from OBSs deployed across the full extent of the Juan de Fuca (JdF) and Gorda plates (Figure 1), including across the JdF and Gorda Ridges. Many of the currently available geophysical constraints on the structure of the oceanic lithosphere-asthenosphere system come from inversion of global datasets, and investigation of the upper mantle with regional seismic data can reveal features not apparent in global-scale inversions [*e.g. Lin et al.,*2016]. Previous seismic results with Cascadia Initiative data have shown that mantle upwelling occurs within approximately 100 km of the JdF Ridge [*Bell et al.*, 2016; Chapter III of this dissertation]. Beneath the JdF plate, mantle flow is driven by the motion of the JdF plate [*Bodmer et al.*, 2015; *Martin-short et al.*, 2015]. However, the fast-polarization

directions from *SKS* splitting are rotated 10 to 20° clockwise of the APM of the JdF plate, which cannot be attributed to lithospheric structure [*Bodmer et al.*, 2015]. In the Gorda region, mantle flow is distinct from that beneath the JdF plate, as deformation is dominated by shear between the JdF and Pacific plates [*Bodmer et al.*, 2015; *Martin-short et al.*, 2015].

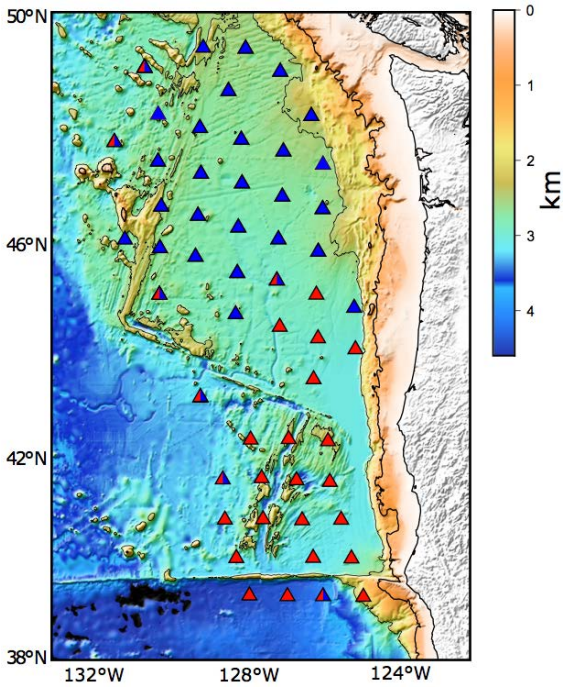

Figure 1. Topographic map of the study area and the locations of the OBSs used. Blue triangles show stations deployed during the first or third year of the Cascadia Initiative, red triangles show stations deployed during the second year of the Cascadia Initiative, and sites reoccupied during a northern and southern deployment are shown by half red and half blue triangles. Background colors show bathymetry in kilometers below sea level. Thick and thin contours are drawn at 1 and 2.5 km below sea level.

To further investigate the structure of the upper mantle beneath the JdF and Gorda plates, we use the *S*-to-*p* receiver function method to look for contrasts in seismic velocity or anisotropy in the upper 200 km of the mantle. We identify a discontinuity beneath the JdF plate that we refer to as the Lehmann (L)

discontinuity. We interpret the discontinuity as a decrease in the magnitude of seismic anisotropy after rejecting models of isotropic seismic velocity on geological grounds. Models consistent with both the receiver function and previously published *SKS* splitting results feature increases in the magnitude of and clockwise rotations of the azimuth of seismic anisotropy within the asthenosphere. These results require deformation of the asthenosphere due to mantle flow that is independent of the overriding lithosphere.

2. Seismic Data and Receiver Functions

We used the *S*-to-*p* receiver function method to identify contrasts in seismic velocity which are sharp relative to the seismic wavelength. Energy converted to *p* waves from vertically polarized *S* waves arrives before the primary *S* phase and so is not contaminated by crustal reverberations. This makes the interpretation of *S*-to-*p* receiver functions simpler than the more commonly used *P*-to-*s* receiver functions for studies of the upper mantle. Seismic data were recorded by ocean bottom seismometers (OBSs) deployed west of the continental shelf during the first three years of the Cascadia Initiative (Figure 1). The majority of the sites marked in blue in Figure 1 were occupied during the first and third years, sites marked in red were only occupied during the second year, and sites marked in half red and half blue were reoccupied during both a northern and southern deployment. Orientations of the horizontal components were provided by IRIS [*Sumy et al.*, 2015]. In this study, we only use the first-arriving *S* phase from events located at epicentral distances of 55° - 85° with magnitudes greater than 6. Converted *p* phases from closer events are reflected back into the Earth, and the *SKS* phase interferes with the primary *S* phase

for epicentral distances between 85° and 95° [*Yuan et al.*, 2006; *Wilson et al.*, 2006]. An insufficient number of high quality *SKS* phases at epicentral distances of greater than 95° were recorded for use in this study. Seismic traces were windowed 200 seconds before and after the *S* wave arrival time predicted by the IASPEI velocity model [*Kennett*, 1991], and were filtered between 10 and 50s with a fourth order, zero-phase butterworth filter. Microseisms generate high levels of seismic noise at shorter periods, while infragravity waves and the tilting of the instruments generate high levels of noise at longer periods [*Webb*, 1998]. We use a wider pass-band than the traditional 'noise notch' between 10 and 33 s [*Webb*, 1998] because the narrower pass-band causes artifacts in the filtered time series which could be incorrectly interpreted as converted phases. Seismograms from a magnitude 7.1 event near Peru that have been processed in this fashion are shown in Figure 2.

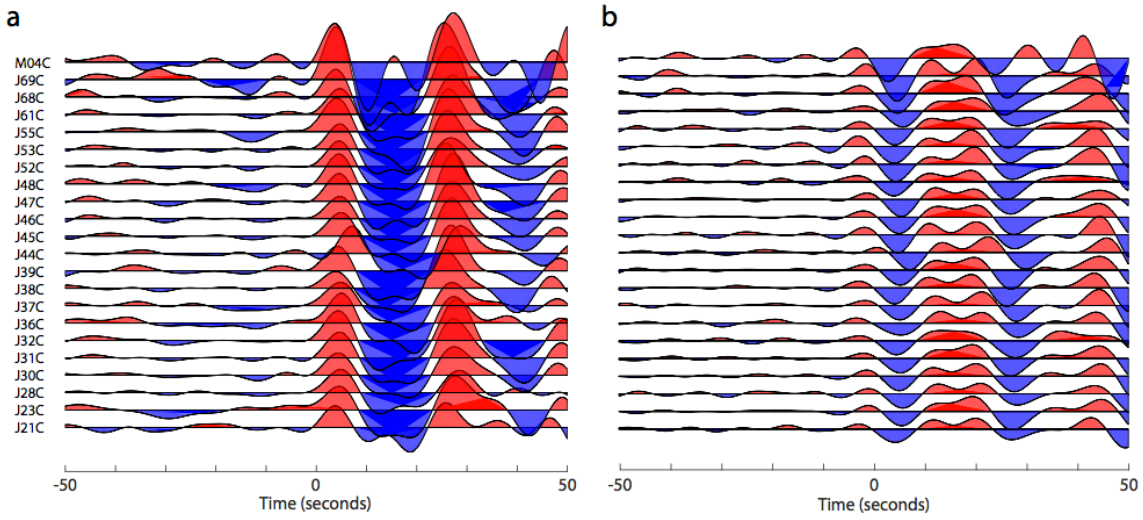

Figure 2. Vertical (a) and radial (b) seismograms for a magnitude 7.1 event off the coast of Peru, which occurred on September 25th, 2013. Seismograms are aligned to the predicted arrival time by the IASPEI radial earth model.

We used a two-step process to identify high-quality data. First, each event was analyzed for signal-to-noise ratio and coherent waveforms between stations on the vertical and radial components. Second, we calculated the implied incidence angle between the vertical and radial seismograms for each event to test if the data were consistent with a vertically polarized shear (*SV*) wave, as proposed by *Kumar and Kawakatsu* [2011]. We found that performing this additional quality control procedure resulted in a more consistent set of receiver functions. We first rotated the seismograms into an empirical *SV* and *P* coordinate system [*Vinnik*, 1977] by finding the implied incidence angle θ that minimizes the amplitude of the candidate *SV* wave on to the *P* component with a grid search. The term 'implied' is used here because the incidence angles and associated surface velocities found in this way may be misleading, as discussed below. We then calculate the implied seismic velocity at the free surface by

$$v = \sin(\theta)/u \quad (1)$$

where v is the implied surface velocity in km/s, u is the horizontal slowness of the teleseismic *S* wave in s/km, and θ is the implied incidence angle in degrees. The horizontal slowness of the teleseismic *S* phase is predicted with the IASPEI velocity model [*Kennett,* 1991]. The distribution of the implied surface velocities for the visually selected events is approximately Gaussian with a mean of 4.0 ± 0.5 km/s within values of 1 and 6 km/s. Outliers cluster near 0 km/s and extend to 10 km/s (Figure S1 of supplementary information). We attribute the 87 station-event pairs with implied surface velocities outside of the range of 1 to 6 km/s to poor quality data and discard them from our analysis. 363 event-station pairs pass this two-step,

quality control procedure. The distribution of these events is shown Figure 3. The azimuthal distribution of these events is uneven, with a vast majority of events coming from Japan, Tonga, and South America (Figure 3b).

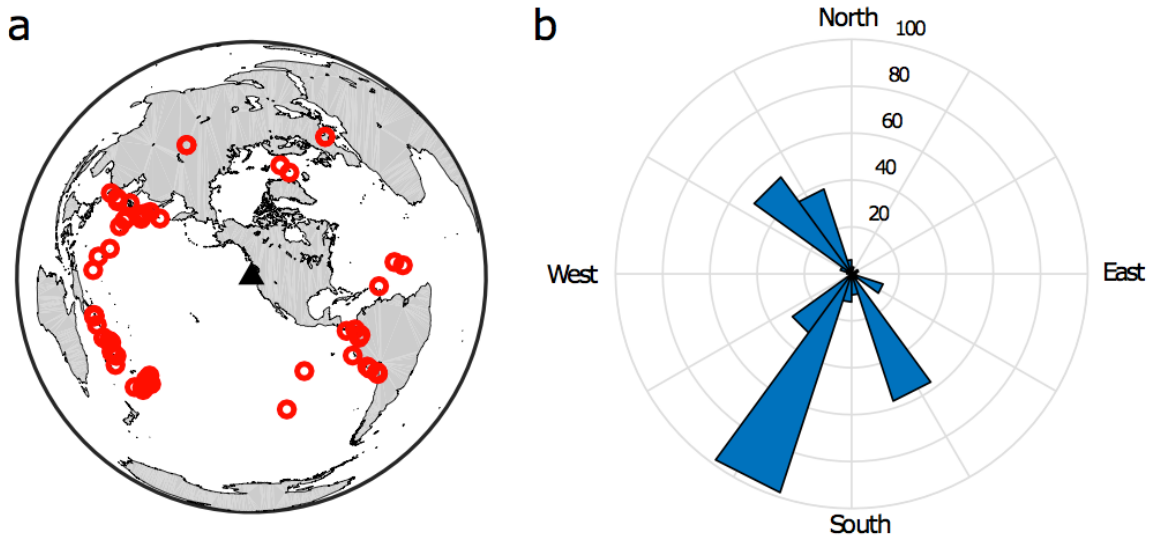

Figure 3. Event distribution. a) Locations of the 73 events used in this study. b) Rose diagram of the azimuth of the station-event pairs used in this study.

This test showed that the highest-quality data are consistent with near vertical incidence angles for the *SV* phases near the free surface. Because of the unrealistically high apparent surface velocities, we interpret the phases on the vertical seismograms as converted *p* phases with near vertical incidence angles in shallow, low *Vs* layers, instead of the projection of a shear wave on to the vertical component. *Harmon et al.*, [2007] showed that this can occur for broadband recordings of teleseismic phases by free fall OBSs when seafloor sediments are as thin as tens of meters, and we show in the following sections that waveforms predicted for the expected sediment structure in Cascadia reproduce the implied surface velocity. For this reason, we do not rotate the seismograms into a *P* and *SV*

coordinate system [*Vinnik*, 1977] to calculate the receiver functions, but use the vertical and radial seismograms.

Receiver functions were calculated using the extended-time, multitaper deconvolution method [*Park et al*., 1987; *Park and Levin*, 2000; *Helffrich*, 2006]. To smooth the source spectra, the traces were divided into 30-s-long segments with 50% overlap. Spectra for each segment were calculated with three Slepian tapers and a half-bandwidth parameter of 2.5, and then all the spectra were averaged [*Helffrich*, 2006]. To plot the arrival times and polarities of the receiver functions as are done for the more traditional *P*-to-*s* receiver functions, the time axis and polarity were reversed. After changing the signs, a sharp increase in isotropic seismic velocity with increasing depth would produce a positive phase in the receiver functions, and vice versa. We migrate the receive functions to depth with the velocity model of *Bell et al*. [2016], which is calculated from the phase velocities of teleseismic Rayleigh waves. The *Vs* model includes variations in the thickness of seafloor sediments and three-dimensional variations in shear-wave velocity.

3. Results

3.1 Receiver Functions

We present the mean of receiver functions from three regions, which we hereafter refer to as the JdF-Ridge (Figure 4a), the JdF-plate (Figure 4b), and Gorda (Figure 4c) stacks. The borders of these three regions are shown in Figure 4d. The JdF-Ridge and Gorda stacks are taken from regions where results from seismic tomography suggest mantle upwelling is occurring [*Bell et al.*, 2016; Chapter III of

this dissertation]. The JdF-plate stack is taken from a region of both higher shear-wave velocities at mantle depths [*Bell et al*., 2016; Chapter III of this dissertation] and fast *SKS* polarization directions that are sub-parallel to the APM of the JdF plate [*Bodmer et al.*, 2015; *Martin-short et al*, 2015]. Error bars are twice the standard deviation of the mean. Each stack is characterized by an amplitude 0.32 to 0.4 at 0 km depth and a negative phase at 50 to 60 km depth with an amplitude -0.175 to -0.2. Below 100 km depth, a negative phase is observed with amplitude of -0.08 at 136 km depth in the JdF-plate stack (Figure 4b). A weaker, and consequently less certain, negative phase at a similar depth is also present in the Gorda stack, and is not observed in the JdF-Ridge stack. We also explored stacks of receiver functions from smaller regions. However, subdivisions of each of these stacks are not statistically distinct from the stacks shown in Figure 4a-c; nor is a stack of receiver functions from the region in between the JdF-Ridge and JdF-plate regions statistically distinct from either (Figures S2-S8).

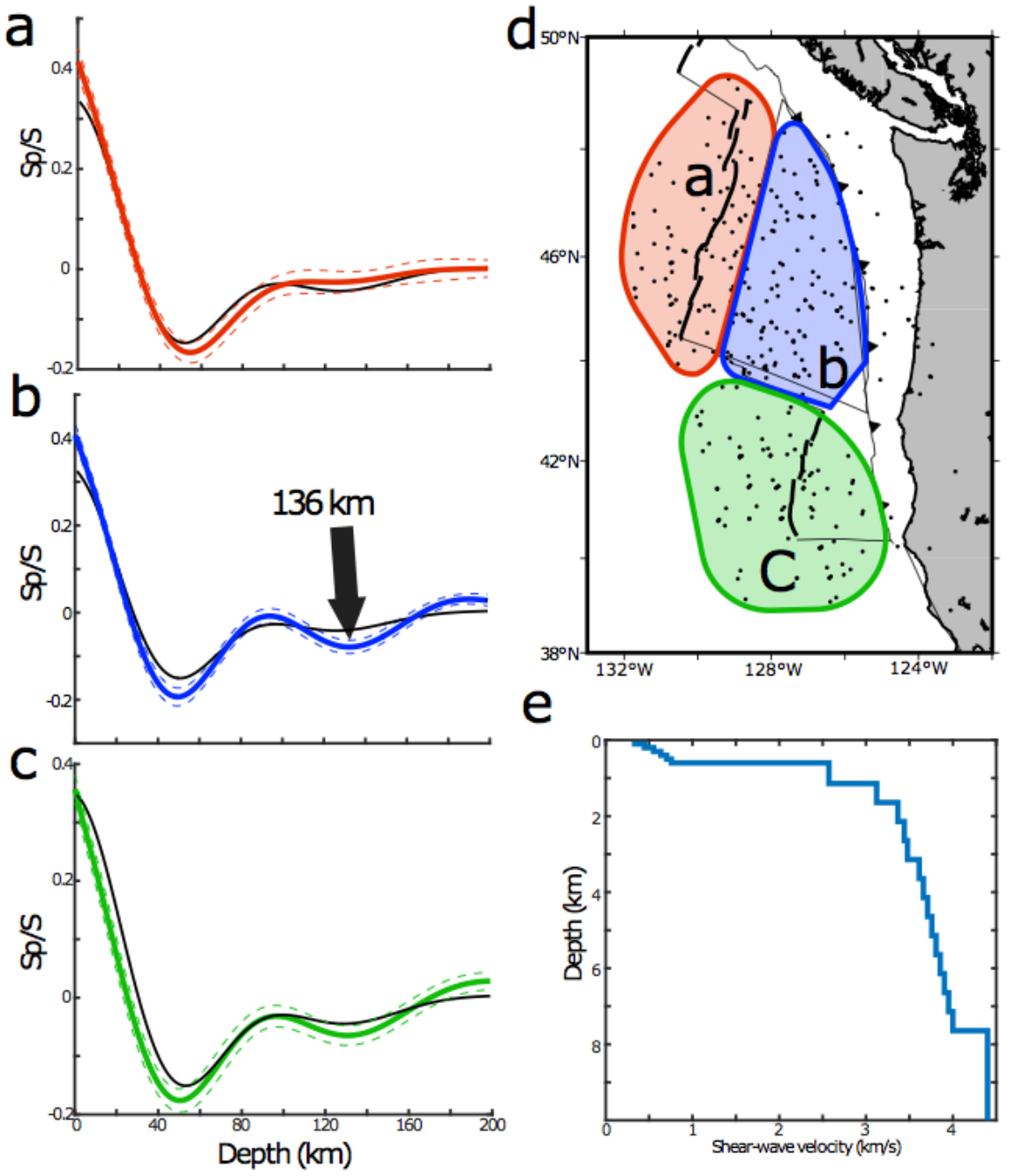

Figure 4. Receiver function results and comparison with synthetics for crustal structure. a,b,c) Stacks of receiver functions (colored) from the JdF-Ridge, JdF-plate, and Gorda regions, respectively, with the associated the 95% confidence intervals (dashed lines). Synthetic receiver functions for the expected crustal structure are shown in black. d) Shaded regions show where the JdF-Ridge (red), JdF-plate (blue), and Gorda (green) stacks were taken from. Black dots show the piercing points of individual receiver functions at 140 km depth. e) Example *Vs* model for the oceanic crust with an 800 m thick sedimentary layer.

3.2 Models of Isotropic Seismic Velocity

Here we explore models of isotropic seismic velocity that are consistent with the results for each stack at shallow depths, and then explore subcrustal structure consistent with the JdF-plate stack. We first show that much of the structure in the receiver functions can be explained by the expected crustal structure. While the presence of a G discontinuity is shown to be consistent with the data, the depth and amplitude of the discontinuity are poorly constrained. An isotropic 10 ± 5% contrast in *Vs* can explain the *S*140*p* phase; models of seismic anisotropy are considered in the following section.

Synthetic receiver functions are plotted alongside the observed receiver functions in Figures 4a-c to show the effect of the crust and sediments on the waveforms. Synthetic receiver functions are a stack of the predicted radial receiver function for each station-event pair [*Park*, 1996; *Levin and Park*, 1998] that have been processed in the same way as the data. Since the lower end of the pass-band in seconds used for filtering is longer than the two-way travel time of a *P* wave in the water column, we do not model water-column reverberations [*Blackman et al.*, 1995]. A different velocity model was used for events recorded at different stations to account for variations in the thickness of the sedimentary layer. Sediment thickness was varied for each OBS as described in Chapter III of this dissertation. We used the model of *Harmon et al.* [2007] for the basaltic crust, and the power law relations of *Ruan et al*. [2014] for *Vs* and *Hamilton* [1979] for *Vp* in the sediments. No discontinuities at depths greater than the Moho were assumed to generate the synthetic receiver functions shown in Figure 4 a-c. An example velocity model is

shown in Figure 4e. The lowest *Vs* layers in Figure 4e above 800 m depth represents the sediments, and the step function increase near 7.5 km depth represents the Moho. The mean implied surface velocity, as defined in Section 2, for the synthetic seismograms generated in this fashion is 3.5 km/s, which is consistent with the value of 4.0 ± 0.5 km/s measured for the data.

The synthetic receiver functions are consistent with the JdF-Ridge and Gorda stacks, but significantly misfit the JdF-plate stack at depths below 100 km. Each stack is approximately matched at depths shallower than 100 km. The misfit to the amplitude and shape of the shallow portion of the Gorda stack may be due to uncertainties in the sediment or crustal structure in the region; we do not explore this further. The negative peak near 50 to 60 km depth in all three stacks can be explained as a sidelobe of the converted phases from the shallow, low *Vs* layers, but the amplitude is misfit in the JdF-plate stack. The synthetics, which were calculated for velocities models with no discontinuities deeper than the Moho, fit the JdF-Ridge and Gorda stack below 100 km depth to the error of the data. In contrast, the misfit to the JdF-plate stack at 136 km depth is significant at the 99% confidence interval. We refer to this deeper arrival as the '*S*140*p*' phase hereafter.

We test the hypothesis that the misfit to the amplitude of the JdF-plate stack near 60 km depth is consistent with a G discontinuity in Figure 5. The G, or Gutenberg, discontinuity is a generic term for a decrease in seismic velocity with increasing depth that is sharp relative to the seismic wavelength. We generate synthetics for velocity models with a decreases in *Vs* with increasing depth of 0% to

15% at 20 to 80 km depth, and evaluate the fit to the observed receiver functions with the misfit function

$$\chi^2 = \sum_{i=0}^{i=N}(R_O - R_P)^2 / E^2)/N \quad (2)$$

where R_o is the observed receiver function, R_p is the predicted receiver function, E is the error of the observed receiver function, and N is the number of points over which the fit was evaluated. We use this approach to ensure that the shape of the waveform, and not just the amplitude at a point, is well fit. In later sections, simpler misfit functions are shown to be sufficient to match the deeper portion of the JdF plate stack. For the results shown in Figure 5a, the fit was evaluated for points at 30 to 90 km depth in increments of 1 km. The results show that the amplitude of the JdF-plate stack is consistent with a G discontinuity at a depth of 35 to 75 km depth. The range of acceptable depths of the G discontinuity is reduced for smaller contrasts across the discontinuity. For example, a *Vs* contrast of 2.5% is only consistent with the data when the depth of the discontinuity is 60 km. We show a comparison between the predicted and observed receiver functions for a 20, 50, and 80 km deep G discontinuity with a 6% contrasts in Figure 5b. The energy from the G discontinuity is superimposed on the sidelobe from the high-amplitude crustal phases at 0 km depth, and the signature of the G discontinuity manifests as a perturbation to the waveform instead of an isolated phase.

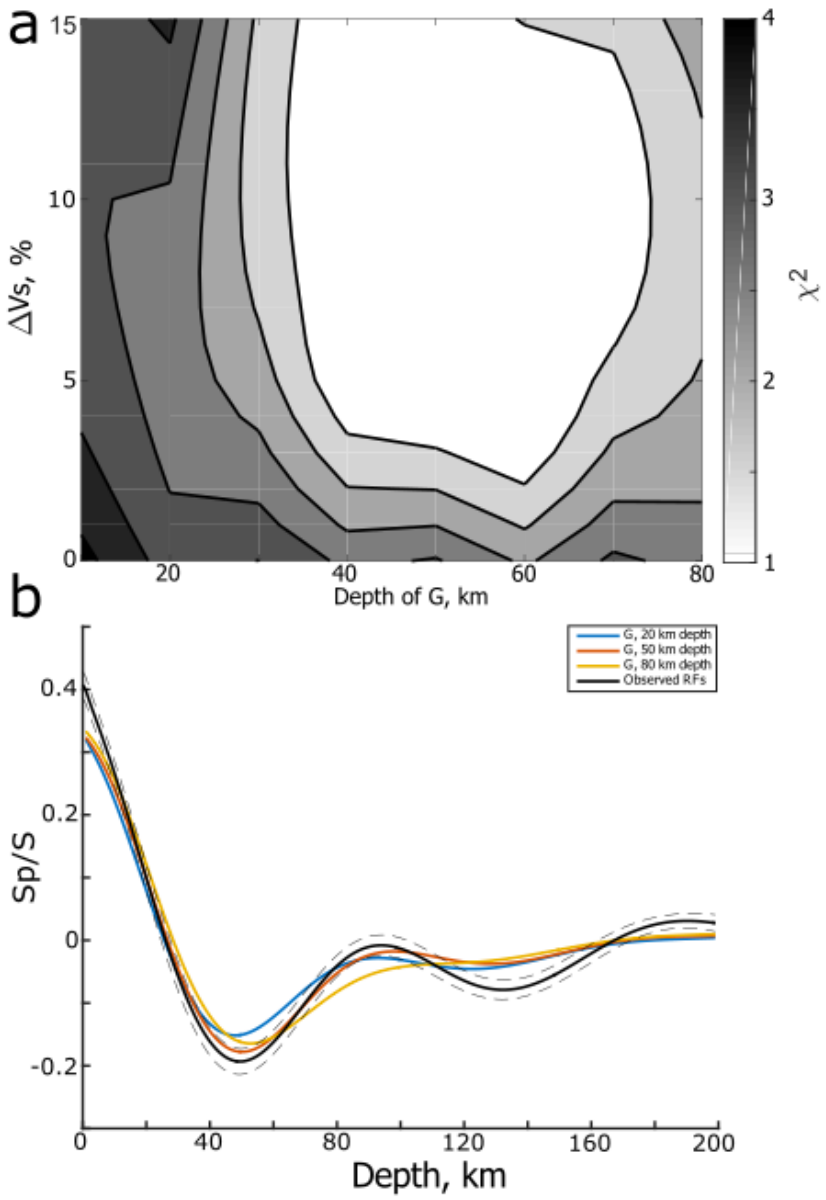

Figure 5. Results of a grid search to test for a G discontinuity beneath the JdF plate. a) Contours show the χ^2 misfit of the synthetic receiver functions for models with a G discontinuity for different depth and velocity contrasts. b) Examples of predicted receiver functions for velocity models with a G discontinuity at 20, 50 and 80 km depth and a 6% velocity contrast. The solid and dashed black lines show the receiver function from the JdF-plate stack and its uncertainty, respectively.

Next, we explore isotropic velocity models that can explain the deeper portion JdF-plate stack. A decrease in *Vs* of 10 ± 5% at 140 km depth can explain the

amplitude of the *S*140*p* phase (Figure 6a). We hereafter refer the deeper discontinuity that the *S*140*p* phase originates from as the Lehmann, or L discontinuity [*Lehmann*, 1937]. This class of velocity models explains the JdF-plate stack below 100 km depth (Figure 6b), and fitting the amplitude of the *S*140*p* phase acceptably matches the shape of the waveform for depths below 100 km. A G discontinuity was not assumed during this grid search. Though we have assumed the converted phase comes from a sharp L discontinuity, previous work has shown that identical converted phases are predicted by all model where a discontinuity is as sharp or sharper than half the seismic wavelength. Larger contrasts can be distributed over the full wavelength and still produced a converted phase [*Bostock et al.*; 1999; *Rychert et al.*, 2007]. Assuming an upper mantle velocity of 4.5 km/s, the decrease in velocity could occur over an interval as wide as approximately 25 km for any velocity contrast, and larger contrasts in *Vs* may be distributed over up to 50 km. In the discussion section, we argue that anisotropic discontinuities, instead of the isotropic models tested here, are more consistent with existing constraints on the seismic structure of the oceanic asthenosphere.

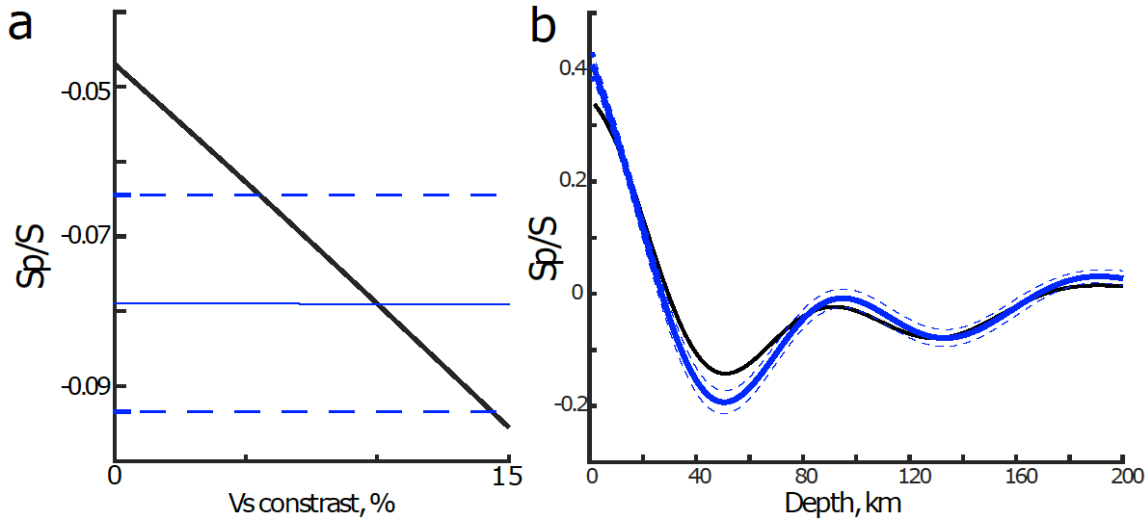

Figure 6. Waveform modeling of the JdF-plate stack with isotropic seismic velocity models. a) Black line shows the predicted amplitude of the *S*140*p* phase in synthetic receiver functions for decrease in *Vs* at 140 km depth, solid and dashed blue lines shows the amplitude of the *S*140*p* phase in the JdF-plate stack and its uncertainty, respectively. b) Black line shows the the best fitting synthetic receiver, solid and dashed blue lines show the JdF-plate stack and its uncertainty, respectively.

3.3 Models of Anisotropic Seismic Velocity

In this section, we explore models of hexagonally symmetric seismic anisotropy that can explain the L discontinuity beneath the JdF plate. We first explore a single layer of anisotropy to find magnitudes and azimuths of seismic anisotropy that are consistent with the data. We then use a Markov Chain Monte Carlo search to explore models of seismic anisotropy consistent with both the receiver function results of this study and the *SKS* splitting results of *Bodmer et al*. [2015].

To test the hypothesis that a contrast in hexagonally symmetric anisotropy could explain the *S*140*p* phase, we constructed models with an L discontinuity as a decrease in the magnitude of anisotropy at 140 km depth. The magnitude of anisotropy was tapered to zero over 40 km above the discontinuity to avoid

unrealistic degrees of shear wave splitting. We only tested a decrease in the magnitude of anisotropy at 140 km depth, since an increase in anisotropy would produce a phase with the opposite polarity as observed. We assumed a horizontal fast axis and that the magnitude of *S* anisotropy is 66% of the magnitude of *P* anisotropy [*Hammond and Toomey,* 2003].

The results of this test are shown in Figure 7a. To make a prediction for a given velocity model, we average a set of synthetic receiver functions that were calculated at the azimuth of each station-event pair used for the JdF-plate stack. Variations in amplitude with the azimuth of seismic anisotropy result from the limited back-azimuth distribution available in this study (Figure 3); were an equal number of receiver functions stacked from all back-azimuths the curves in Figure 7a would be offset by the magnitude of anisotropy and display no back-azimuth dependence. To evaluate these model, we find the difference between the maximum and minimum in the predicted receiver function near 90 and 136 km depth, respectively, for different fast directions and contrasts in the magnitude of anisotropy at the L discontinuity (Figure 7a). We use a difference in amplitude between two parts of the waveform, instead of the absolute amplitude of the *S*140*p* phase, for modeling the receiver functions for anisotropic models because some models of anisotropy predict negative values in the receiver function over a wide range of depths after bandpass filtering, but significantly misfit the waveform, as shown by the predicted receiver functions for 20° and 120° with a 6% contrast in *S* anisotropy (Figure 7b). Using the grid search to fit the difference between two points of the waveform removes the effect of this DC offset and accurately matches

the waveforms after bandpass filtering (green line in Figure 7b). We note that the minor perturbations to the receiver functions in the presence of seismic anisotropy can remove the misfit to the receiver function that was potentially attributable to a G discontinuity, as discussed in Section 3.2. Both the red and green traces in Figure 7b fit the JdF-plate stack at depths shallower than 100 km, even though only the relative amplitude of the *S*140*p* phase was evaluated. Finally, we do not model converted phases from horizontally polarized shear waves (*SH*), which average to zero for the azimuths used (Figure S9). Analysis of *SV*-to-*p* receiver functions that have been binned by azimuth would require modeling the *SV* and *SH* components of the source simultaneously, which is beyond the scope of this study.

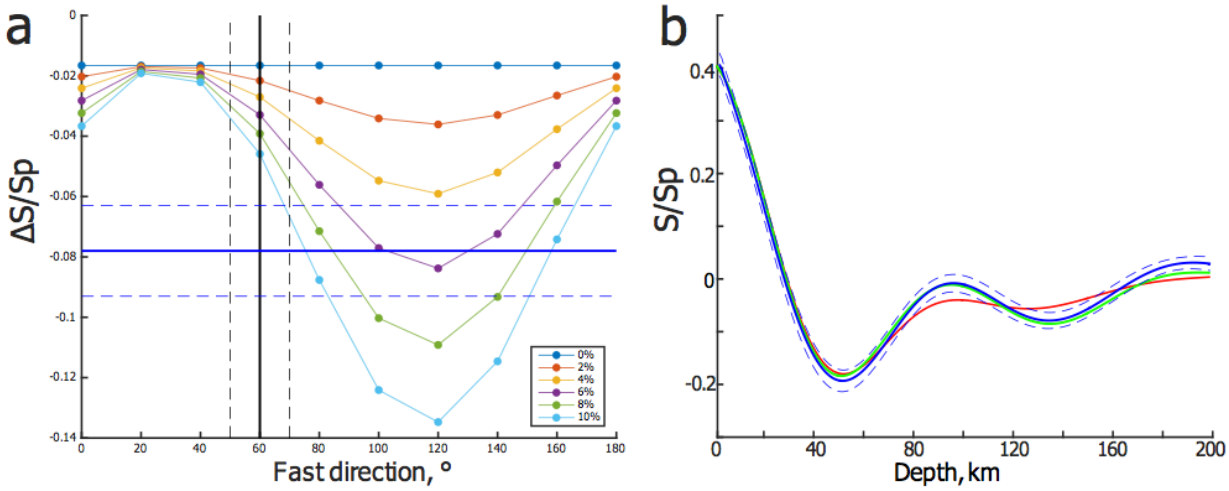

Figure 7. Waveform modeling of the JdF-plate stack with anisotropic seismic velocity models. a) Colored lines with circles show the predicted amplitude of the *S*140*p* phase, relative to the maxima near 90 km depth, for a decreases in the magnitude of *S* anisotropy at 140 km depth with different fast directions. The solid and dashed black lines show the fast polarization direction from *SKS* splitting for the JdF plate and its uncertainty, respectively. The solid and dashed blue lines show the relative amplitude of the *S*140*p* phase in the JdF-plate stack and its uncertainty, respectively. b) Solid and dashed blue lines show the JdF-plate stack and its uncertainty, respectively. The red and green lines show the predicted receiver functions for decrease in *S* anisotropy of 6% with fast directions of 20° and 120°, respectively.

The receiver function results require a fast direction that is clockwise of the *SKS* fast polarization direction (Figure 7a). Note that the *SKS* fast direction is in turn clockwise of the azimuth of the APM of the JdF plate [*Bodmer et al.*, 2015]. Varying the dip of the fast axis decreases the amplitude of the converted phases without changing how the amplitudes vary by back-azimuth (Figure S10).

To find models of seismic anisotropy consistent with both the receiver function and *SKS* splitting results, we used a Markov Chain Monte Carlo search [*Sambridge et al.*, 2002; *Shen et al.*, 2013]. The details of search are described in Appendix A, and the model parameters are summarized in Table 1. We vary the magnitude and fast direction in an upper and lower layer (a_U, φ_U, a_L, and φ_L in Table 1) at mantle depths between the Moho and an L discontinuity held fixed at 136 km depth. We also vary the thickness of the lower layer, and the thickness of a gradational region (*B* and *W,* respectively). The parameters, their initial ranges, and their final ranges in all acceptable models are summarized in Table 1, and three example models are shown in Figure 8.

Typical solutions feature a high-magnitude keel of anisotropy with a large clockwise rotation above the L discontinuity. a_L is greater than a_U and φ_L is clockwise of φ_U (Figure 8a,b). The central azimuth allowed for φ_L, 105°, is 45° clockwise of the average fast direction from SKS splitting [*Bodmer et al.*, 2015]. The model shown in Figure 8a and b has values near the center of the final range for each model parameter (Table 1), and represents a typical solution.

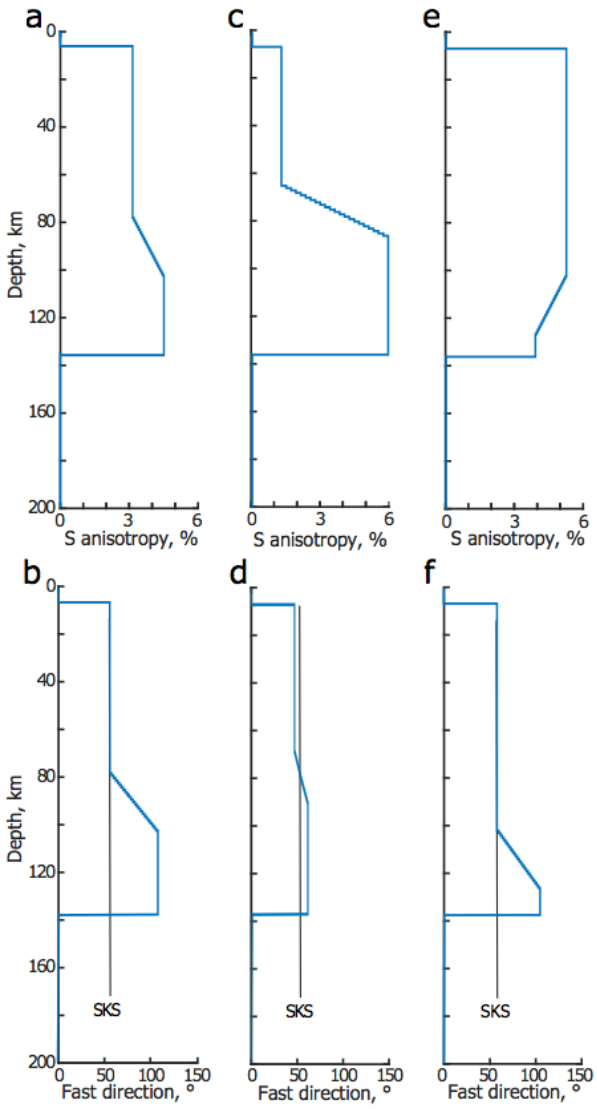

Figure 8. Each column shows a model of seismic anisotropy found by the Markov Chain Monte Carlo search, as discussed in the text. (a,c,e) Magnitude of *S* anisotropy with depth. (b,d,f) Azimuth of the fast direction with depth. Solid black lines mark the fast polarization direction from *SKS* splitting.

Alternative models are made possible by the uncertainties in the data. In some cases, φ_L is close to the *SKS* fast polarization direction. As shown in Figure 7a, these models require large degrees of anisotropy at the L discontinuity (Figure 8c) and will only satisfy the limits of the acceptable amplitudes of the receiver functions. When a_L is large, φ_U is counter-clockwise of the *SKS* fast polarization direction

(Figure 8d), and so the fast direction still rotates with depth. Because of the effect of the lower layer on the *SKS* splitting prediction, the final range for φ_U extends up to 40° counter-clockwise, but only 10° clockwise, of the *SKS* fast polarization direction of 60°. In other models, the contrast in anisotropy is smaller than expected from the results of Figure 7a. One such example is shown in Figure 8e and f. In this case, both *B* and *W* are small, and the decrease in the magnitude of anisotropy with increasing depth is distributed from 100 to 136 km depth (Figure 8e). Less anisotropy is required to decrease directly at the L discontinuity in this scenario. The final ranges of *B* and *W* are wider than the initial ranges (Table 1), and so the data does not strictly require any specific geometry for the transitional region between the upper and lower anisotropic layers.

Table 1. Summary of parameters used in the Markov Chain Monte Carlo search

Name	Description	Initial Range	Final Range
a_U	Peak-to-peak magnitude of *S* wave anisotropy in the upper layer, %	0.5 - 7	0.5 – 4.5
φ_U	Fast direction in the upper layer, °	20 - 90	20-70
a_L	Peak-to-peak magnitude of *S* wave anisotropy in the lower layer, %	0.5 - 7	2.2 – 9
φ_L	Fast direction in the lower layer, °	20 - 150	65 - 145
B	Thickness of the lower layer, km	10 - 60	0 – 70
W	Width of the central gradational region, km	10 - 80	0.5 - 70

No model of homogeneous anisotropy between the Moho and the L discontinuity satisfies the observations from both receiver functions and *SKS* splitting. Figure 9 compares a_L and a_U for the 802 acceptable models found by the Markov Chain Monte Carlo search. Models that fall along the dashed line in Figure 9

have the same magnitude of anisotropy in both the upper and lower layers; note that the majority of models fall to the right of the dashed line, indicating an increase in anisotropy with increasing depth above the L discontinuity (Figure 8a,c). All models with magnitudes a_U similar to or greater than a_L have φ_L clockwise of 70°. Hence if the magnitude of anisotropy is similar thorough the mantle between the Moho and L discontinuities, then the fast direction must rotate across the same region; these models cluster in the top-left of Figure 9. The misalignment between φ_L and φ_U generally grows with increasing a_U; φ_L reaches a peak value of 150° only for the highest values of a_U and represents the maximum degree of misalignment between φ_L and the *SKS* fast direction. If the fast direction is similar through the region between the Moho and L discontinuity, then the magnitude of anisotropy must markedly increase above the L discontinuity; these models cluster in the bottom-left of the Figure 9. While no model parameter is uniquely constrained by the data, significant variation in anisotropy above the L discontinuity is featured in all acceptable models.

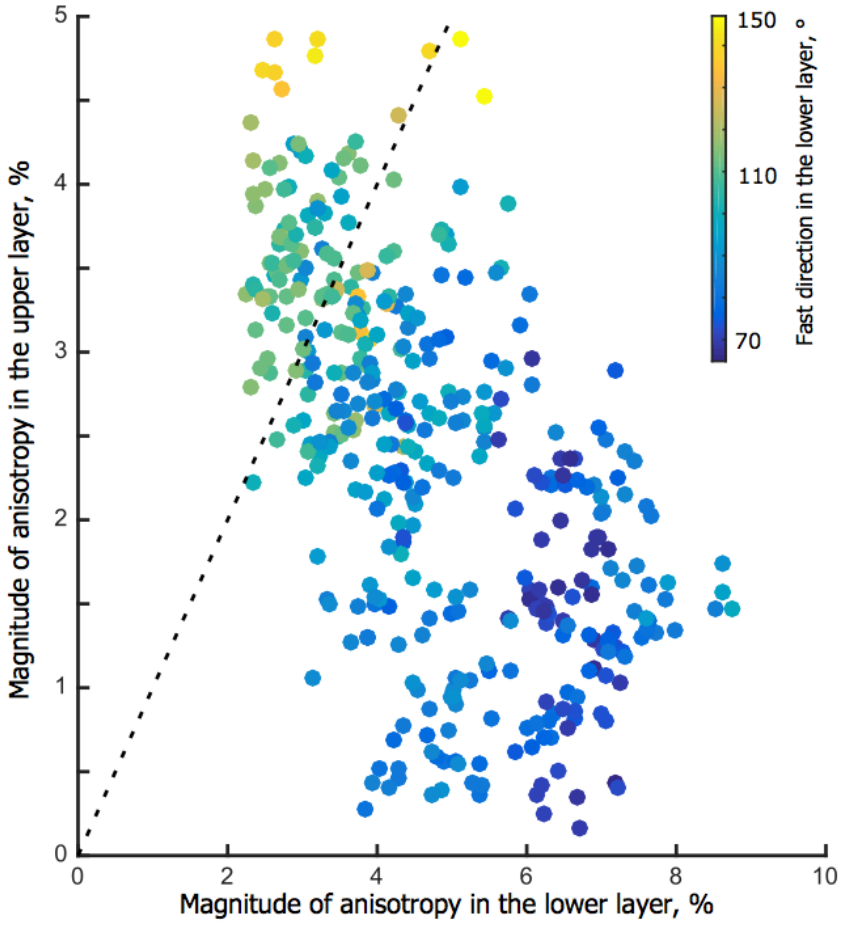

Figure 9. Comparison between the magnitude of anisotropy in the upper and lower layers of models found by the Markov Chain Monte Carlo search. Colors show the fast direction in the lower layer in degrees. The dashed line marks where models would have the same magnitude of anisotropy in the both the upper and lower layer. See text for discussion.

4. Discussion

Our results provide evidence for an L discontinuity beneath the JdF plate and do not require upper mantle discontinuities beneath either the JdF or Gorda Ridges. While the G discontinuity is often observed beneath oceanic lithosphere [e. g. *Gaherty et al.*, 1996; *Kawakatsu et al.*, 2009], the L discontinuity is more often detected beneath the continents than the oceans [*Gu et al.*, 2001] and is generally

detected from 150 to 250 km depth [*Rost and Weber*, 2001]. Whether the L discontinuity represents an isotropic or anisotropic contrast is disputed and the physical origin of the discontinuity may be different in different regions [*Gaherty and Jodan*, 1995; *Vinnik et al.,* 2005]. We first discuss our constraints on the G discontinuity, and then discuss implications of the L discontinuity for mantle flow in the oceanic asthenosphere

While our results are consistent with a G discontinuity beneath the JdF plate, the large converted phases from shallow structure make the depth and amplitude difficult to constrain. The allowable depths beneath the JdF plate range from 35 to 70 km depth, which is consistent with competing hypotheses that predict either age progressive [*Kawakatsu et al.*, 2009] or age independent [*Hirth and Kohlstedt*, 1996] depths to the G discontinuity. Further, while the range of allowable depths narrows to 45 to 65 km depth for *Vs* contrasts below 4%, the surface wave model of *Bell et al.*, [2016] shows a 7% decrease in *Vs* from 25 to 45 km depth for the same region. We conclude that our results suggest the presence of a G discontinuity beneath the JdF plate, but do not constrain the depth of the discontinuity well enough to discriminate its origin. In addition, the synthetic receiver functions for anisotropic velocity models shown in Figure 7b can explain the misfit amplitude of the JdF-plate stack that was first observed in Figure 4b, and shows that a G discontinuity is not strictly required to explain the JdF-plate stack.

Next, we discuss the physical origin of the L discontinuity and implications for our understanding of the oceanic asthenosphere. We prefer an anisotropic to isotropic origin for the L discontinuity beneath the JdF plate. Results from surface

wave tomography show increasing *Vs* at depths below 100 km beneath young oceanic lithosphere [*Nishimura and Forsyth*, 1989; *Bell et al.*, 2016], while isotropic models for the L discontinuity require a decrease in *Vs* with increasing depth. In contrast, the magnitude of anisotropy generally decreases with increasing depth in the upper mantle [*Nishmura and Forsyth*, 1989; *Montagner and Tanimoto*, 1991; *Gaherty et al.*, 1996]. Furthermore, the required *Vs* contrast across the L discontinuity is too large to be explained by the physical factors that determine seismic velocity in the upper mantle. Assuming a *Qs* of 100, an increase in temperature of 650 ± 300 K is necessary to explain a 10 ± 5% decrease in *Vs* [*Karato*, 1993], and the melt fraction of the asthenosphere is not expected to increase with increasing depth [*Hirschman*, 2010]. *Qs* below 140 km depth is over 100 in most regions [*Dziewonski and Anderson*, 1981], which is too large for variations in anelasticity to significantly affect *Vs*. Finally, the only known phase changes that may occur near 140 km depth predict an increase, not decrease, in *Vs* with increasing depth [*Bagely and Revenaugh*, 2008 and references therein]. For these reasons, we prefer an anisotropic origin for the *S*140*p* phase and the L discontinuity.

We do not observe evidence for L discontinuities beneath the JdF and Gorda Ridges. No converted phases are observed from beneath the Moho at the JdF Ridge (Figure 4a), and there is only weak evidence for an L discontinuity in the Gorda stack (Figure 4c). Because the mantle upwells beneath the ridges, the anisotropic fabric that gives rise to the L discontinuity beneath the JdF plate may be disrupted beneath the JdF and Gorda Ridges. In addition, we note that we do not observe

evidence for a sharp decrease in melt fraction with increasing depth beneath the JdF or Gorda Ridges. Previous studies have presented evidence for increases in *Vs* with depth beneath hotspots that were attributed to the onset of melting at 75 to 150 km depth [*Havlin and Parmentier*, 2014 and references therein]. Melting likely begins beneath the JdF Ridge between 200 and 300 km depth in the carbonatite stability field [*Dasgupta and Hirschmann,* 2006], and no converted phases are expected if melt fractions retained in the mantle are smooth over a length scale of 25-50 km depth.

Finally, the acceptable models of seismic anisotropy are inconsistent with a passively deforming asthenosphere. Because the fast direction of anisotropy rotates clockwise with increasing depth (Figure 8) and is always clockwise of the motion of the JdF plate, shear near the L discontinuity cannot be associated with the present-day motion of the overriding lithosphere. Neither can the anisotropy reflect the alignment of mantle flow with past plate motion. Since the JdF plate is currently rotating in the clockwise direction [*Riddihough*, 1984], both the *SKS* fast polarization direction [*Bodmer et al.*, 2015] and the fast direction at the L discontinuity are ahead of, and not lagging behind, changes in plate motion. The rotation of the lithosphere with respect to the deeper mantle is to the west in this region [*Ricard et al.*, 1991], and accounting for a westward drift will only enhance the misalignment. Because the azimuth of seismic anisotropy will align with the flow direction for total strains of only 1.5 [*Zhang and Karato*, 1995], and development of significant *S* anisotropy occurs when larger strains have been reached [*Tommasi*, 1998], the magnitude of anisotropy at the L discontinuity suggests that the fast direction faithfully records

the direction of mantle flow. Furthermore, any increase in the magnitude of anisotropy between the Moho and the L discontinuity likely requires an increase in shear-strains at depths well separated from the base of the JdF lithosphere, which is the opposite of the prediction for a passively deforming asthenosphere. Therefore, while viscous coupling with the overriding lithosphere is necessary to explain the fast polarization direction from *SKS* splitting [*Bodmer et al.,* 2015; *Martin-Short et al.*, 2015], an additional driving force for mantle flow is required within the asthenosphere.

Mantle flow can be dynamically driven from within the asthenosphere by variations in density or pressure. Density-driven flow beneath the Pacific plate has been inferred from linear gravity anomalies that are aligned sub-parallel to APM [*Haxby and Weissel,* 1986], but these anomalies are not observed above the JdF plate. Large-scale, density driven flow in the mesosphere could be coupled to the lower asthenosphere and explain the misalignment of the fast direction at the L discontinuity, though an increase in anisotropy above the L discontinuity is likely inconsistent with this scenario. Pressure-driven flow within the asthenosphere can occur if the viscosity of the asthenosphere is an order of magnitude lower than the deeper mantle [*Phipps Morgan et al.*, 1995]. Consistent with our results suggesting an increase in the magnitude of anisotropy above the L discontinuity and a clockwise rotation of the fast direction in the upper layer of our models relative to APM, pressure-driven flow can dominate the deformation of the asthenosphere over plate-driven flow [*Höink et al.*, 2012], particularly if the asthenosphere is as thin as ~200 km [*Weismüller et al.*, 2015]. One possible source of anomalies in pressure is

the subducted JdF slab, which could cause variations in pressure by acting as a barrier to mantle flow [*Phipps Morgan and Smith*, 1992]; westward rollback of the slab could enhance this effect. Another possibility is that viscous coupling between the faster-moving Pacific plate with the asthenosphere could cause variations in pressure that are capable of driving asthenospheric flow beneath the adjacent slower-moving JdF plate [*Buck et al.*, 2009].

We attribute the decrease in the magnitude of anisotropy below the L discontinuity to either a lower boundary condition to asthenospheric flow, or to a shear-zone within the asthenosphere. In the first view, mantle flow is more rapid above than below the L discontinuity, and the gradient in seismic anisotropy reflects the faster rate of mantle flow above the discontinuity. One possible barrier to mantle flow is a change in deformation mechanism from dislocation to diffusion creep with increasing depth, which would cause a change from a non-linear rheology above to a linear rheology below [*Karato and Wu,* 1993]. This would enhance the anisotropic contrast at the L discontinuity because seismic anisotropy is not created by deformation during diffusion creep [*Karato*, 1992]. A problem with this interpretation is the observation of anisotropy at depths below 200 km depth globally [e.g. *Montagner and Tanimoto*, 1991; *Lin et al.*, 2016], which suggests that the L discontinuity beneath the JdF plate may be shallower than the depth where the change in deformation mechanism occurs. Alternatively, the L discontinuity could reflect a decreasing gradient in shear within an asthenospheric channel [*Lin et al.*, 2016]. In this view, asthenospheric flow extends to deeper depths than the L discontinuity. However, seismic anisotropy does not develop below the

discontinuity where the vertical gradient in mantle flow is weak. This scenario may require a deeper layer of anisotropy below the L discontinuity near the base of the asthenosphere [*Lin et al.*, 2016], which is not constrained by our results. In addition, while the sharp L discontinuity assumed in Section 3.3 is unlikely to develop in the shear-zone scenario, receiver functions at long periods are consistent with an L discontinuity that occurs over a range of depths up to 50 km [*Bostock*, 1999; *Rychert et al.*, 2007].

5. Conclusions

We present evidence for an L discontinuity below the JdF plate. *S*-to-*p* receiver functions require a decrease in either seismic velocity or the magnitude of seismic anisotropy at 136 km depth, and models of seismic anisotropy are more consistent with pre-existing constraints on the structure of the oceanic asthenosphere. Similar discontinuities are not confidently observed beneath the JdF or Gorda Ridges. Models of seismic anisotropy consistent with results from both *SKS* splitting and *S*-to-*p* receiver functions are inconsistent with an asthenosphere that deforms via a passive response to the motion of the lithosphere. Instead, dynamically driven mantle flow is required to explain a rotation of the azimuth of seismic anisotropy and an increase in the magnitude of anisotropy above the L discontinuity. We therefore propose that below the JdF plate, pressure-drive flow occurs within a low viscosity asthenosphere.

CHAPTER V

CONCLUSION

A common theme emerged in each chapter of this dissertation. Mantle flow was inferred from the seismic velocities constrained in each study, and in each study mantle flow driven by a force other than drag from the overlying lithosphere was invoked. Plate tectonics has been successful in describing many features of the Earth's surface, yet the connection between the motion of the lithosphere and the underlying styles of mantle convection has remained unclear. Beneath the Galápagos Archipelago, the tilt of the mantle plume inferred from prior tomographic studies does not parallel the motion of the lithosphere. Upwelling to shallow depths was required to explain results from different disciplines, but does not occur beneath a region of lithospheric extension. Instead, it occurs off axis in a region of active convection. Buoyancy-driven upwelling beneath the JdF Ridge requires that the strength of the asthenosphere is low enough that density variations can compete with viscous coupling to the lithosphere as a driving force for mantle flow. These density variations cause asymmetric melting about the ridge and downwelling off-axis. A low viscosity asthenosphere is also predicted to host horizontal mantle flow, and some intra-asthenospheric driving force is required to explain the anisotropic structure beneath the JdF plate.

Yet in many ways these observations raise more questions than they answer. A low-viscosity asthenosphere is suggested but the precise strength of the upper mantle remains elusive. Small melt fractions or dissolved water can weaken the mantle and appear to be required. At minimum, the null-hypothesis of a dry and

solid asthenosphere modulated by temperature can be rejected. The presence of melt in the upper mantle was inferred, but the depth distribution of melt beneath the JdF and Gorda Ridges is poorly constrained. This is a particular intriguing problem in light of the eruption of enriched basalts in the Gorda and Explorer diffuse plate boundaries, suggesting that the distribution of melt at mantle depths may play a role in determining the composition of mid-ocean ridge basalts. Further studies of the isotropic and anisotropic structure of the oceanic lithosphere-asthenosphere system will likely reveal more examples of asthenospheric flow decoupled from the overlying plates.

Despite these open questions, the view that the oceanic lithosphere-asthenosphere system is dominated by a passive response to the motion of the lithosphere can be rejected. Similarly, the physical state of the upper mantle cannot be explained only in terms of the cooling lithosphere. While viscous coupling with and the conductive cooling of the lithosphere must occur, the behavior of the asthenosphere is not solely determined by these surface processes. Internally sourced heterogeneity and convection in the asthenosphere are needed to explain the seismic observations.

APPENDIX A

CHAPTER II THE EFFECT OF DEHYDRATION ON SEISMIC VELOCITY

We used the model of *Karato and Jung* [1998] to estimate the effect of dehydration on seismic velocity. In this model, the concentration of water in mantle minerals (primarily olivine) has almost no effect on the elastic behavior of the mantle. The water content of the mantle affects only anelastic behavior, described by the shear wave quality factor Q. Laboratory studies strongly suggest, but have not conclusively demonstrated, that small amounts of dissolved water in nominally anhydrous minerals (even less than 100 ppm H/Si) can reduce Q; conversely, removing water from these minerals increases Q. Here, we summarize this model and give values that would be necessary to explain the amplitude of the G discontinuity beneath the Galápagos. In an anelastic material, energy is lost during deformation, which attenuates seismic waves. The degree of anelasticity is characterized by Q; the higher the Q, the less energy is lost. Q depends strongly on the frequency of a seismic wave. Beneath young oceanic lithosphere [*Jackson and Faul,* 2010], Q is predicted to depend on ω as $Q \propto \omega^{-\alpha}$, where ω is the angular frequency and α is a dimensionless constant called the frequency dependence that varies in the Earth from 0.1 to 0.4. This model for Q is known as the absorption band model [*Anderson and Given*, 1982].

Low-Q materials are not only attenuating, they have lower seismic velocity. The fractional reduction in shear velocity relative to the perfectly elastic velocity (V_o) is given approximately by

$$\frac{\Delta V}{V_o} = \frac{1}{2}\cot\left(\frac{\pi\alpha}{2}\right)Q^{-1} \quad \text{(A1)}$$

The reduction in shear velocity, ΔV, is therefore greater when Q is lower or when α is lower (that is, when a material is more attenuating or when Q is less dependent on frequency). Removing water from the mantle increases Q and increases the shear velocity. By this means, a dehydration boundary can create a seismic discontinuity. Because a rigorously derived relation between Q and water content has not been established, we use the approximation of *Karato and Jung* [1998] by which Q depends on the concentration of water, C_{OH}, according to

$$Q^{-1} \propto C_{OH}^{\alpha} \quad \text{(A2)}$$

To derive (A2), we assume that the only term in the model of *Karato and Jung* [1998] that changes when the upwelling mantle crosses the solidus is C_{OH}. We model the effect of water on seismic velocity through the effect of water on Q for an assumed value of Q at temperatures below the solidus. A change in water concentration by a factor of 100 would mean a change in Q of 100^{α}, or 1.5 to 4 for an α value of 0.1 to 0.3, respectively. Note that Q changes more for greater ΔV, but it affects the seismic velocity more strongly for smaller ΔV because of the cotangent term in equation (A1).

We cannot rigorously constrain the concentration of water or Q at different depths beneath the Galápagos, but we can calculate the combination of Q, C_{OH}, and α that could give a sufficiently large velocity contrast to account for at least part of our observations. First, we note that laboratory studies suggest that α can be ~0.1 in

partially molten rocks [*Faul et al.*, 2005] and 0.1 represents the lower end of the observed values of α [*Shito et al.*, 2004]. We fixed the value of α at 0.1 to maximize the effect of water on seismic velocity. Second, we assume, following *Karato and Jung* [1998], that at a C_{OH} of 1 ppm H/Si the behavior of a nominally anhydrous mineral is the same as under fully anhydrous conditions. We consider dehydration, then, to be equivalent to the reduction of C_{OH} to 1 ppm H/Si.

We used equations (A1) and (A2) to calculate the shear velocity change induced by dehydration across the anhydrous solidus for different initial values of Q and C_{OH}, as shown in Figure A1. Our observed velocity contrasts of 5% and 11% are both within the paramater space shown. We note two important issues. First, the concentration of water at depths greater than that at which the temperature is at the anhydrous solidus is not the concentration of water in normal mantle. Rather, it is the concentration of water that remains after the upwelling mantle has passed through the volatile-enhanced melting regime. Although the Galápagos plume at sufficient depth may have a fairly high concentration of water [*Koleszar et al.*, 2009], the majority of the water will have been removed before the upwelling material reaches the depth at which the temperature is at the anhydrous solidus [*Hirth and Kohlstedt*, 1996]. Second, the values of Q necessary to explain fully the discontinuities are low, 20 to 35 for 100 ppm H/Si. Had we assumed a larger value for α, the required Q values would be even lower. For comparison, Q beneath the East Pacific Rise is as low as 50 between 50 and 100 km depth for shear wave periods betwen 10 and 70 s [*Yang et al.*, 2007]. However, values of Q similar to those required to match the results for the Galápagos region are observed in magmatically

active areas between 50 and 100 km depth for energy at 1 Hz [*Abers et al.*, 2014]. Another possible explanation of our observations is that the amplitude of the G discontinuity is not controlled solely by dehydration, but by a combination of factors, including depletion by melt extraction and a contrast in retained melt fraction.

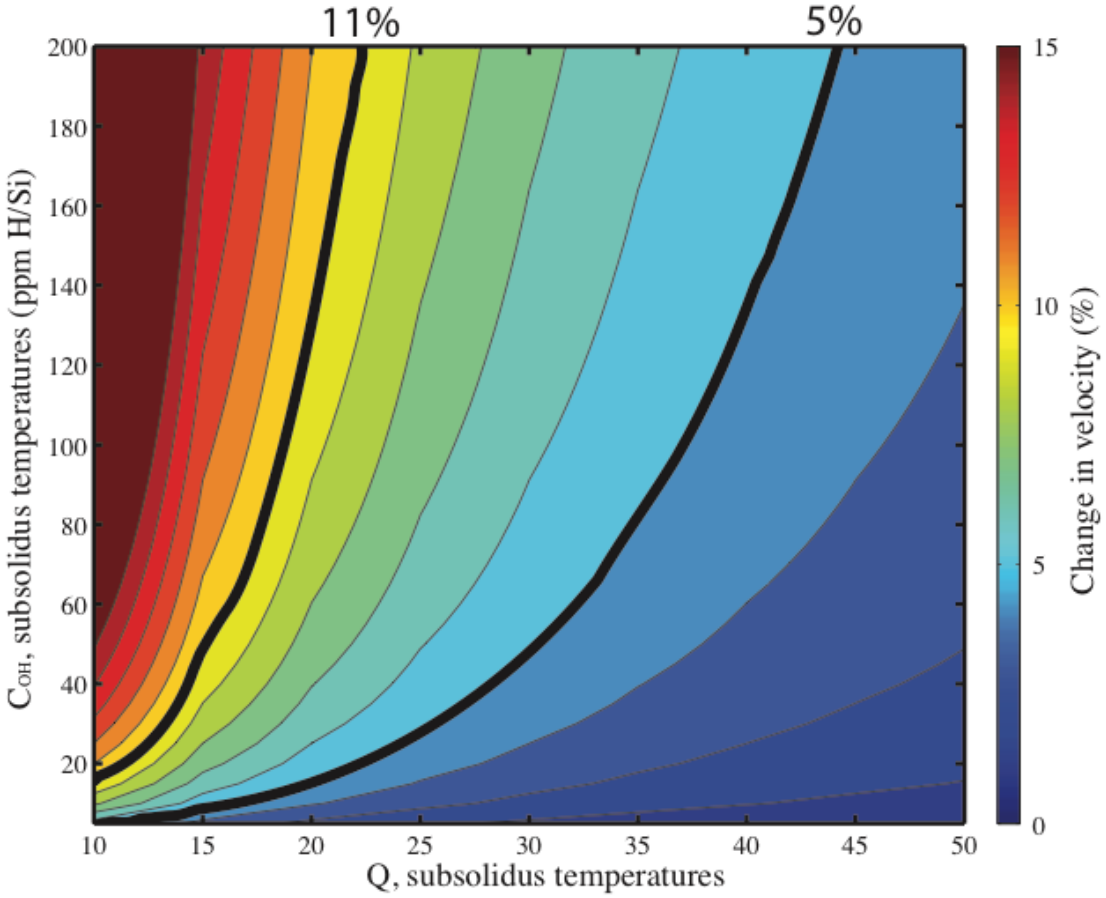

Figure A1. Calculated change in shear velocity at the anhydrous solidus dehydration boundary as a result of anelasticity. Bold contours indicate the inferred velocity contrasts beneath the southeastern archipelago (11%) and surrounding region (5%).

APPENDIX B

CHAPTER III SUPPORTING INFORMATION

Text S1: Uncertainty of a delay time measurement

We explore the uncertainty of a delay time measurement by cross-correlating synthetic waveforms. First, a random offset in time between -3 and 3 seconds was applied to each of a set of 12 identical waveforms. Then, these traces and 12 time-series of white noise were filtered in the same way as the OBS data. The filtered noise was scaled and added to the offset waveforms to create synthetic traces with a chosen signal-to-noise ratio (SNR), defined as the ratio of the maximum amplitude of the waveform to the RMS of the noise. Finally, the noisy traces were cross-correlated with the method of *VanDecar and Crosson*, [1990]. The errors that noise introduced to the delay time measurements were found by taking the difference between the measured delay times and the original delay times applied to the waveforms. This process was repeated 1000 times for different SNRs.

Figure S1 shows the standard deviation of the errors for SNRs between 5 and 80. The standard deviation of the set of errors provides an estimate of the uncertainty for an individual measurement. Only waveforms with a minimum SNR of approximately 10 would be useable with the OBS data. In Figure S1, the picking error assumed in this paper (0.25 s) is shown by the black line. We choose this value as a conservative minimum for the acceptable error, since other factors such as signal-generated noise may introduce additional uncertainty.

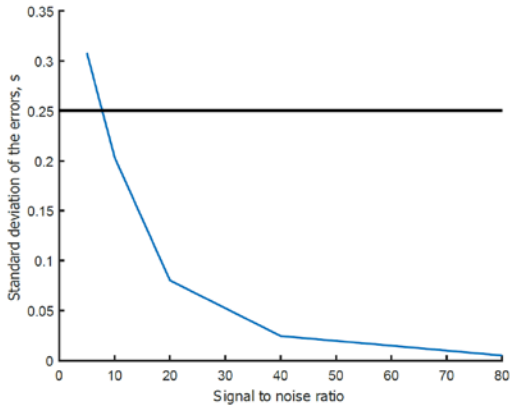

Figure S1. Standard deviation of the errors of delay time measurements for synthetic waveforms with different signal to noise ratios. The black line shows the minimum error assumed in this study.

We found that the method of *VanDecar and Crosson*, [1990] underestimates the uncertainties. Figure S2 compares the true error for each synthetic waveform, as measured by the procedure describe above, with the error predicted by the method of *VanDecar and Crosson*, [1990] for signal to noise ratios of 5 (Figure S2a) and 40 (Figure S2b). The best fitting lines to the results have slopes of 0.05 and 0.34 for SNRs of 5 and 40, respectively; slopes of 1 would indicate that the two sets were consistent. We conclude that the predicted error is consistently less than the true error and that the disagreement is more severe for lower quality data.

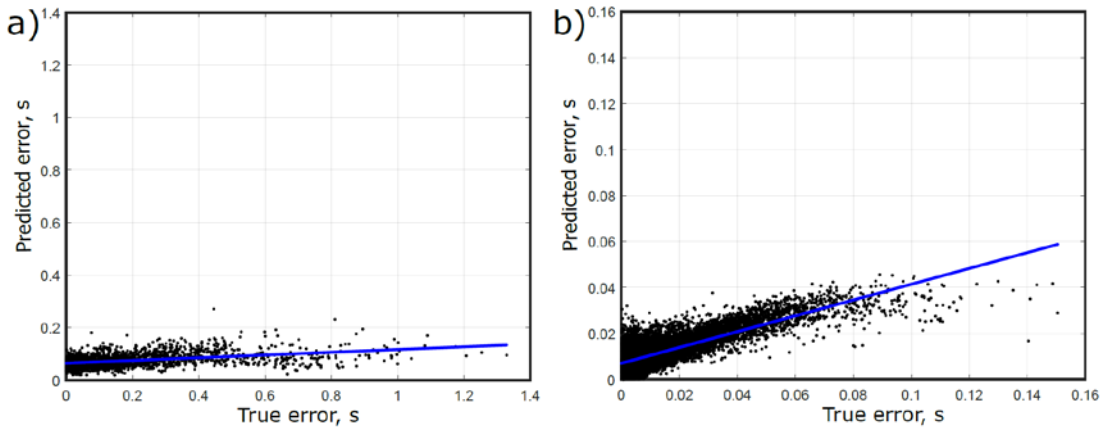

Figure S2. Errors of delay times predicted by the method of *VanDecar and Crosson*, [1990] against the true errors at signal to noise ratios of a) 5 and b) 40. The blue line is the best fitting lines through the results.

Text S2: Mean delay and station statics by year of the Cascadia Initiative

Here we show that changes to the delay times at most reoccupied sites are acceptably small. Figure S3 shows the same dataset as Figure 5a, but separated by year of the Cascadia Initiative. Data from the Blanco transform experiment are shown with the second year. The four stations circled in Figure S3 (J63A and G03A in year 1, G03B in year 2, and J23C in year 3) were not included in the preferred result because the mean delay time changed by more than 0.8s between deployments. For J63A (the northwestern station in year 1) and J23C (the southwestern station in year 3), the site in question was occupied three times and delays measured by only the removed station were anomalous; for G03A and G03B (the southernmost station in year 1 and reoccupied in year 2) the anomalous station could not be identified. The differences of the mean delay between reoccupied sites are shown in Figure S4. The stations discussed above have been removed, and the remaining changes are all less than 0.5 s. The circled sites were reoccupied during at

least one northern and southern deployment, and are shown by half blue and half red triangles in Figure 2.

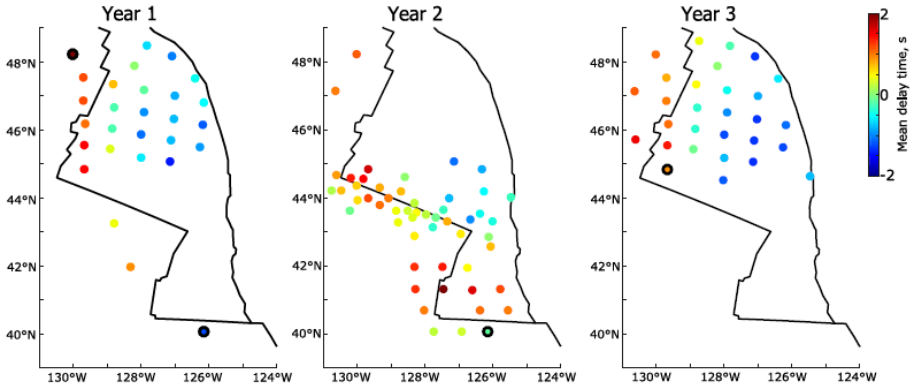

Figure S3. Mean delay times by year for each site. Stations deployed during the Blanco transform experiment are shown with the second year. Circled stations were not used for the preferred inversion; see text for details.

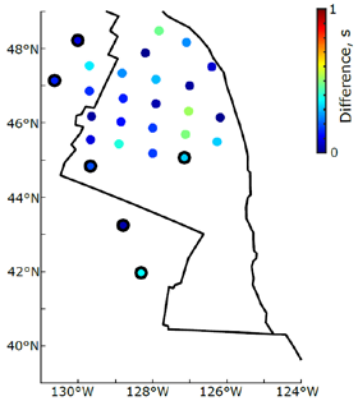

Figure S4. Absolute value of differences in the mean delay recorded at reoccupied sites. Circled stations were occupied during at least one northern and southern deployment.

The station statics from the preferred inversion are shown in Figure S5. The statics are of similar magnitude to the differences shown in Figure S4. The long-wavelength patterns apparent in the actual delay times (Figures 5a and b) are not apparent in the station statics of Figure S5. For inversions that used less damping to

the station statics, long-wavelength patterns became apparent, which we attribute to mantle structure.

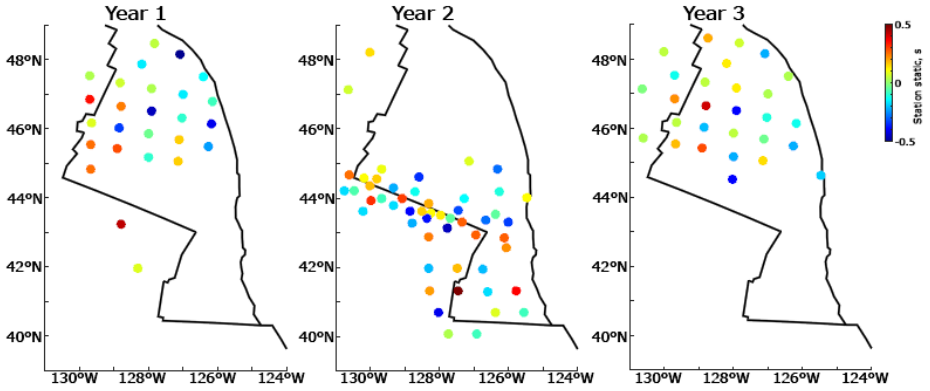

Figure S5. Station statics solved for during the preferred inversion, shown by year of the Cascadia Initiative. Stations deployed during the Blanco transform experiment are shown with the second year. The RMS of these statics is 0.22 s.

Text S3: Summary of alternative models

In this section, we summarize the results of tomographic inversions other than the preferred model used in the main text. The full set of models is summarized in Table S1 and we show depth slices through 4 models that reflect different approaches to processing the data. For certain inversions in Table S1, the station statics have been fixed to the set shown in Figure S5 to facilitate direct comparison with the preferred model. Models in Table S1 with higher penalties and horizontal smoothness have higher RMS misfits to the data. For lower horizontal smoothing, the misfit did not converge to a stable result during non-linear ray tracing and higher misfits are achieved. The effect of the vertical smoothing constraint is explored in Section 5.

Table S1 Summary of different tomographic inversions. The preferred model that used in the main text is in bold.

Model Description	Starting and Final RMS (% reduction)	RMS of station statics	Penalty, vertical smoothing, horizontal smoothing weights
Suspect Stations included with sediment corrections	1.42 to 0.47 s (67%)	0	1, 75, 150
Sediment corrections not applied	0.95 s to 0.43 s (55%)	0	1, 75, 150
Sediment corrections applied and no station terms	1.42 s to 0.45 s (68%)	0	1, 75, 150
Sediment corrections and heavily damped station terms	1.42 s to 0.44 s (69%)	0.05 s	1, 75, 150
Sediment corrections and moderately damped station terms	**1.42 s to 0.43 s (70%)**	**0.22 s**	**1, 75, 150**
Sediment corrections and lightly damped station terms	1.42 s to 0.42 s (70%)	0.3 s	1, 75, 150
Sediment corrections and undamped station terms	1.42 s to 0.41 s (71%)	1.4 s	1, 75, 150
Squeezing test – 300 km depth	1.42 s to 0.44 s (69%)	0.22 s (fixed)	1, 75, 150
Squeezing test – 200 km depth	1.42 s to 0.46 s (68%)	0.22 s (fixed)	1, 75, 150
Squeezing test – 100 km depth	1.42 s to 0.51 s (64%)	0.22 s (fixed)	1, 75, 150
Increased penalty and fixed station terms	1.42 s to 0.46 s (68%)	0.22 s (fixed)	4, 75, 150
Decreased penalty and fixed station terms	1.42 s to 0.43 s (70%)	0.22 s (fixed)	0.5, 75, 150
Decreased horizontal smoothing	1.42 s to 0.47 s (67%)	0.22 s	1, 75, 100
Increase horizontal smoothing	1.42 s to 0.47 s (67%)	0.22 s	1, 75, 250

The results of an inversion that used data from all OBSs for which delay times could be measured are shown in Figure S6. This inversion includes data from 4 stations (J20B, G27B, G37B, and G02B) that ongoing analysis of *P* wave data from onshore and offshore Cascadia found to be associated with anomalously large delay times after shallow corrections (M. Bodmer, personal communication); these stations have been removed from all other analysis in this paper. The model in Figure S6 also used data from the 4 anomalous stations identified in Section 1 of the Supporting Information. The model in Figure S6 contains high amplitude, circular anomalies not apparent in the preferred model, for example near 44˚N/127˚W, 42˚N/128˚W, and 40˚N/126˚W.

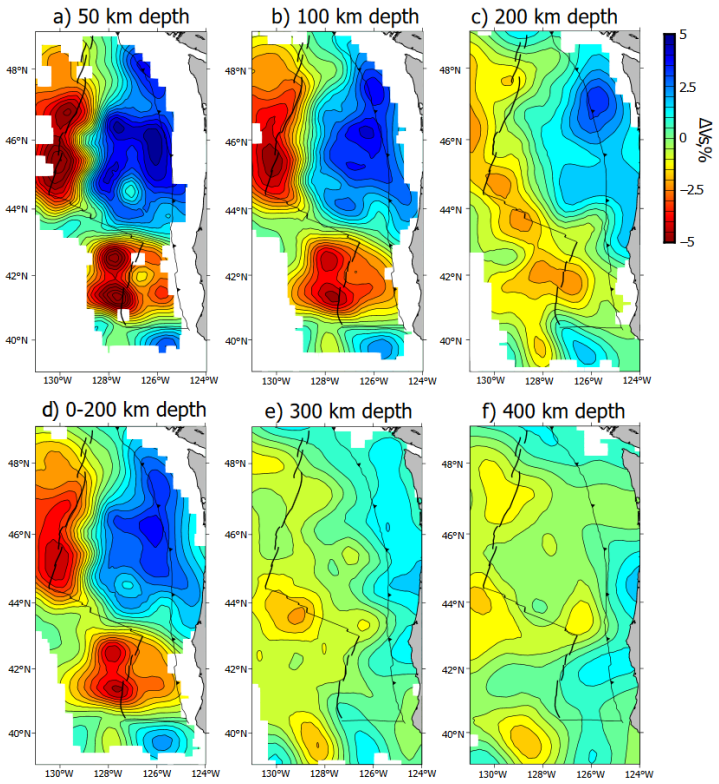

Figure S6. Map view sections through a tomographic model that used data from all OBSs for which delay times could be measured, at a) 50 km depth, b) 100 km depth, c) 200 km depth, d) the average over 0 to 200 km depth, e) 300 km depth, and f) 400 km depth. White areas are masked where there is no ray path coverage. This result includes stations whose timing is suspect; see text for details.

The results of an inversion without sediment corrections or station statics are shown in Figure S7. This model shares several features with the preferred model, such as a large gradient in *Vs* beneath the eastern flank of the JdF Ridge, sinuosity in mantle structure near the Blanco transform fault, and asymmetry about the central JdF Ridge. However, *Vs* is lower near the Cascadia megathrust, where sediments are known to be thicker, than near the center of the plate. This model is not preferred because the structure of the sediments is well constrained near the continental margin (Figure 5c) and can be corrected for *a priori*.

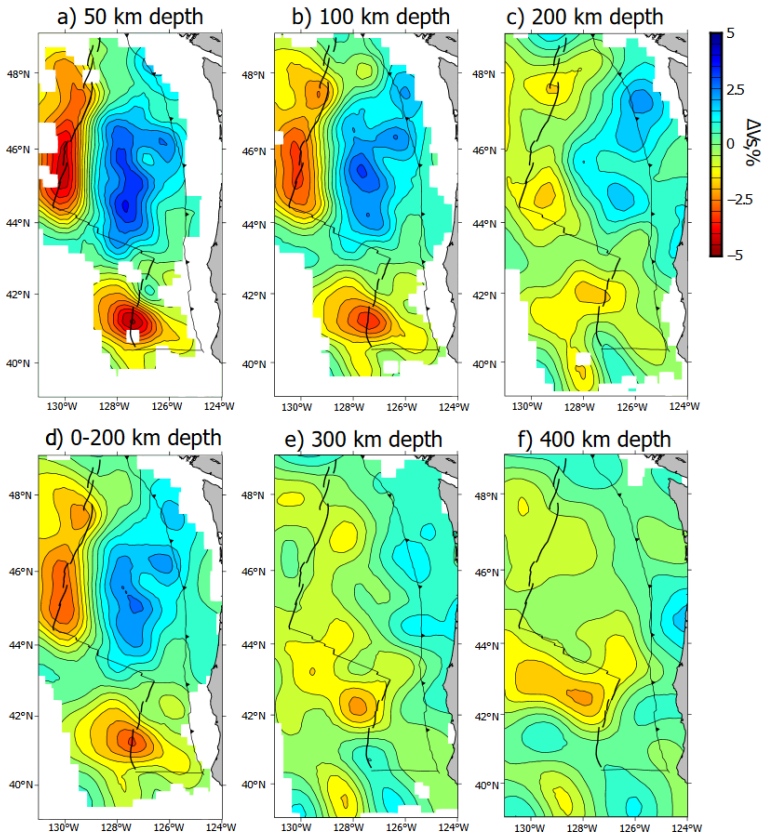

Figure S7. Map view sections through a tomographic model that did not apply sediment corrections and did not solve for station statics, at a) 50 km depth, b) 100 km depth, c) 200 km depth, d) the average over 0 to 200 km depth, e) 300 km depth, and f) 400 km depth. White areas are masked where there is no ray path coverage.

The results of an inversion that solved for undamped station statics are shown in Figure S8. Sediment corrections were used, but their effect on the model was offset by the statics. Relatively small amplitude anomalies are recovered and the RMS misfit to the data is only slightly lower than for other models (Table S1, line 7). The largest amplitude structures are beneath the northern JdF Ridge and a circular, fast anomaly beneath the central JdF plate. The station statics solved for during this inversion are shown in Figure S9. A comparison with Figure 5a shows that most of the signal has been absorbed by the statics. On the basis of the

recovered structures, which are less geologically plausible, and the large station statics, which display long-wavelength trends, we consider this model implausible.

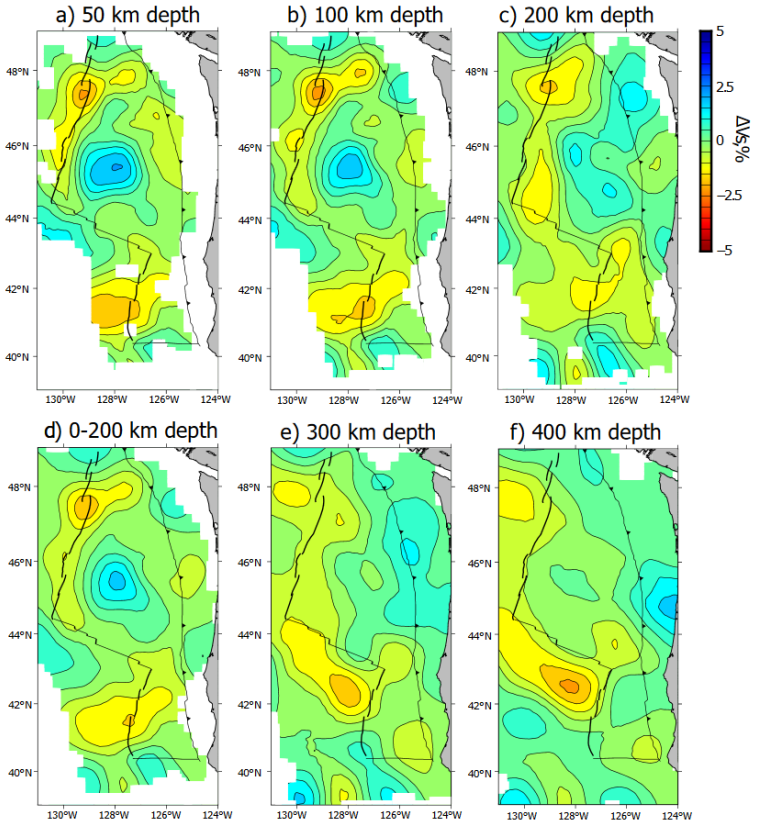

Figure S8. Map view sections through a tomographic model that solved for undamped station statics, at a) 50 km depth, b) 100 km depth, c) 200 km depth, d) the average over 0 to 200 km depth, e) 300 km depth, and f) 400 km depth. White areas are masked where there is no ray path coverage. Much of the actual structure is absorbed in the station statics; see text and Figure S9.

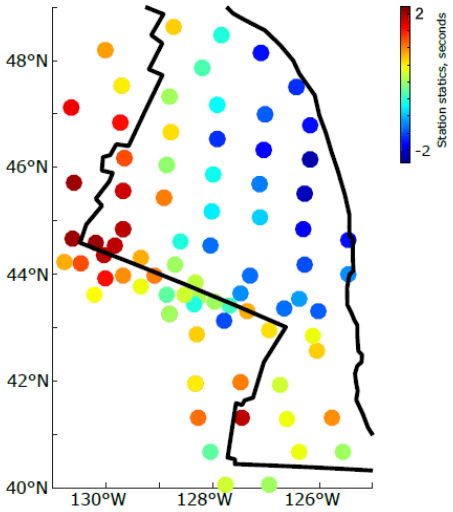

Figure S9 Station statics solved for during the inversion for the model shown in Figure S8. Values are averaged at reoccupied sites for comparison with Figure 5a of the main text.

The results of an inversion that applies sediment corrections but does not solve for small adjustments to station statics are shown in Figure S10. This model is rougher than the preferred model, particularly at 50 km depth. The high *Vs* gradients on the eastern flank of the JdF Ridge are less smooth near 47°N/128°W, and the high *Vs* anomalies beneath the older JdF plate are less continuous near 45°N/127°W. We prefer a model that uses a combination of sediment corrections and damped station statics because we cannot be confident that the short wavelength structures present in Figure S10 are due to mantle structure, and not due to uncertainties in the sediment corrections, variations in the velocity of the oceanic crust, or OBS timing errors.

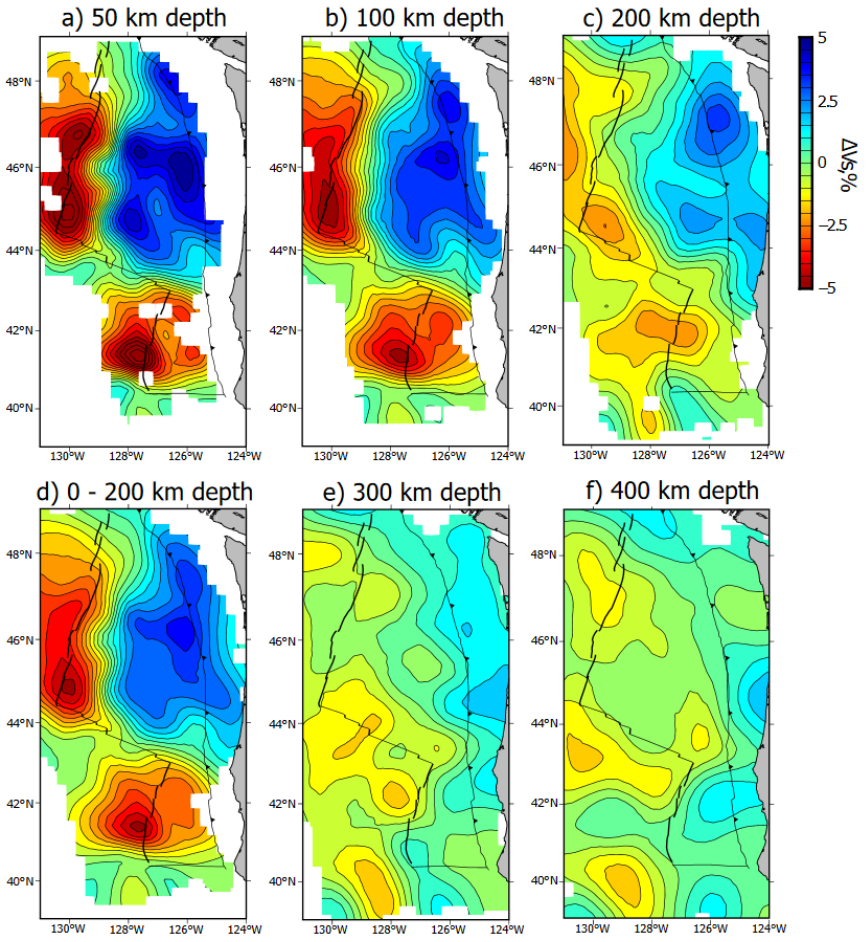

Figure S10. Map view sections through a tomographic model that used sediment corrections and did not solve for station statics, at a) 50 km depth, b) 100 km depth, c) 200 km depth, d) the average over 0 to 200 km depth, e) 300 km depth, and f) 400 km depth. White areas are masked where there is no ray path coverage.

Text S4: Effect of the sediment corrections on the velocity model

We show an inversion of only the sediment corrections in Figure S11 to demonstrate their effect on a tomographic result. Amplitudes are highest near the surface and only weak anomalies are observed by 200 km depth. Regions with smaller than average sediment corrections are associated with negative velocity anomalies because the delay times are demeaned during the inversion. Many of the short-wavelength features reflect regions where the preferred model and the model

shown in Figure S10 differ because the damped station statics mute small amplitude and short-wavelength variations. The amplitudes of the anomalies in Figure S11 indicate that the sediment corrections do contribute to the range of the anomalies in the preferred model. However, many features that we interpret are not apparent in Figure S11, such as the asymmetry and large gradients near the JdF Ridge.

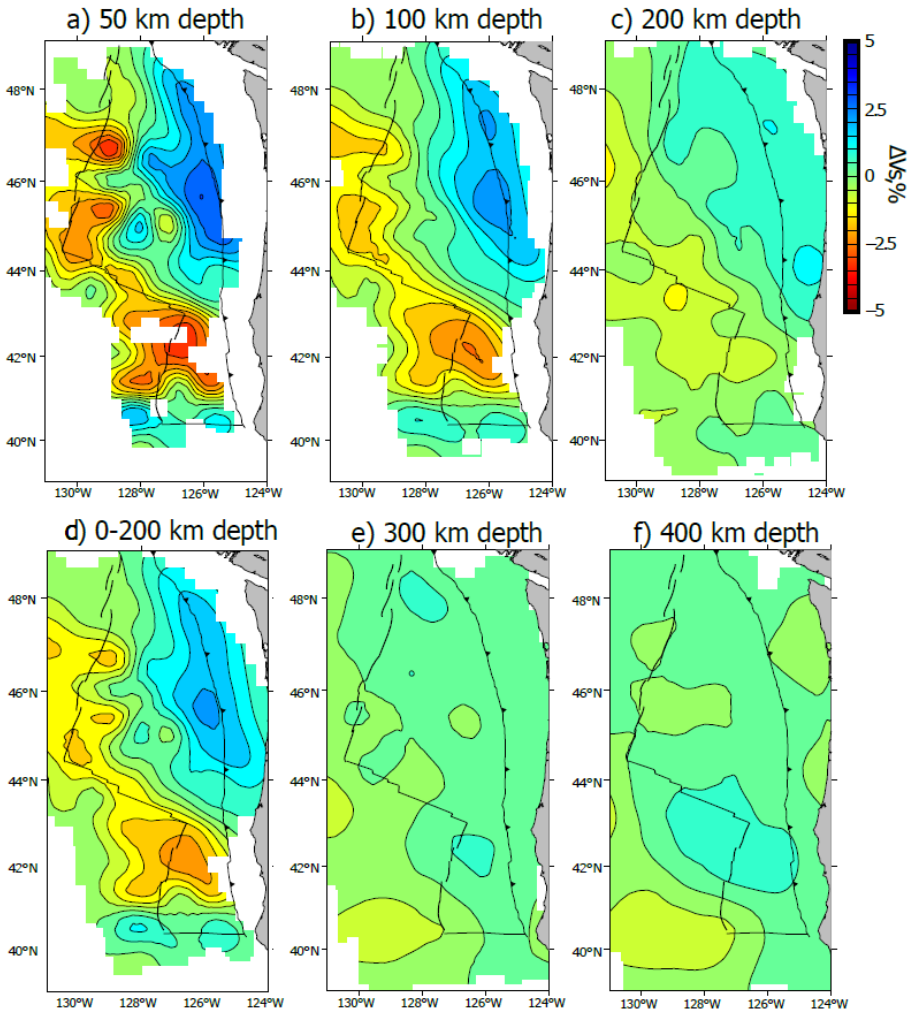

Figure S11. Map view sections through a tomographic model that used only sediment corrections as the input data, at a) 50 km depth, b) 100 km depth, c) 200 km depth, d) the average over 0 to 200 km depth, e) 300 km depth, and f) 400 km depth. White areas are masked where there is no ray path coverage.

Text S5: Synthetic test with ideal station and event coverage

Here we demonstrate the ability of our inversion to recover an input model under ideal imaging conditions. We repeated the synthetic test shown in Figure 10 of the main text, but assumed an even grid of stations spaced every 70 km from 41˚N to 49˚N and from 125˚W to 131˚W and an even distribution of events spaced every 5˚ and 10˚ in epicentral distance and azimuth, respectively, relative to the center of the array. Figure S12 shows that the depth extent of anomalies is better recovered than in Figure 10, but still overestimated. The improvement relative to Figure 10 is more apparent for the shallower than deeper layer of anomalies.

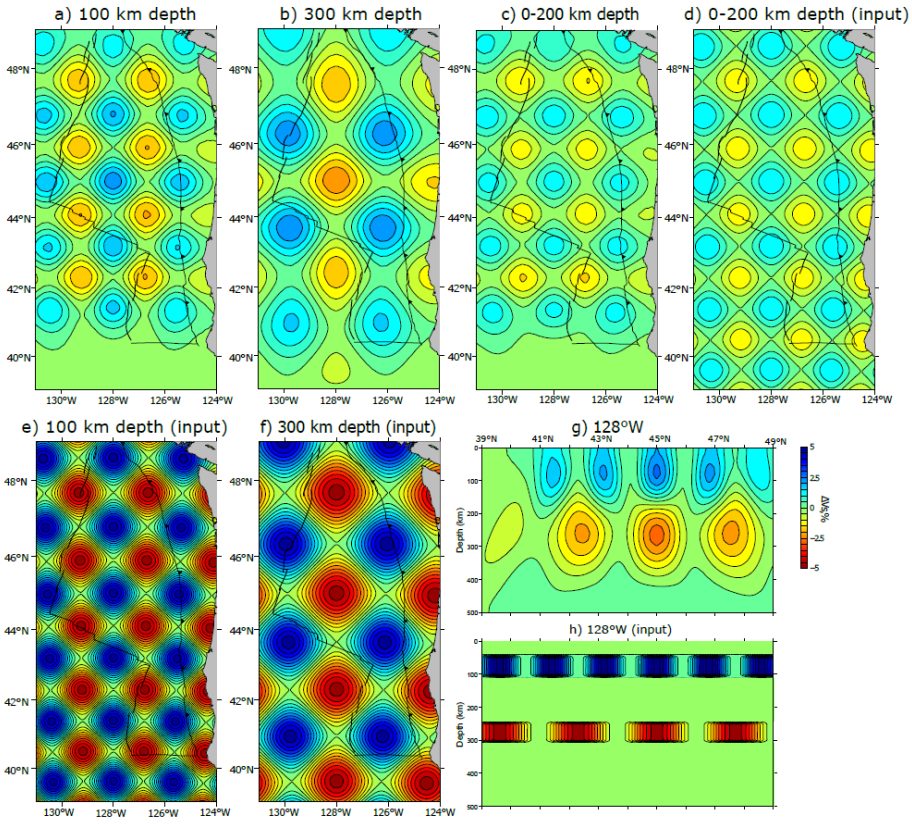

Figure S12. Checkerboard resolution test. Synthetic data were generated for a model with a regular pattern of anomalies and that assumed an even distribution of stations and events. The recovered model is shown at 100 km depth (a), 300 km depth (b), averaged over the upper 200 km (c), and along longitude 128˚W (g).

Anomalies from the starting model are shown for the same regions in panels d, e, f, and h.

We attribute the limited vertical resolution of these inversions to the use of near-vertical teleseismic ray paths. To investigate the effect of the vertical smoothing constraint, which is the other plausible limiting factor, in Figure S13 we show a cross-section through an inversion of the same data set used for Figure S12, but with the vertical smoothing weight set to 1. The recovery of the lower layer is similar and the anomalies in the shallower layer still extend toward the surface.

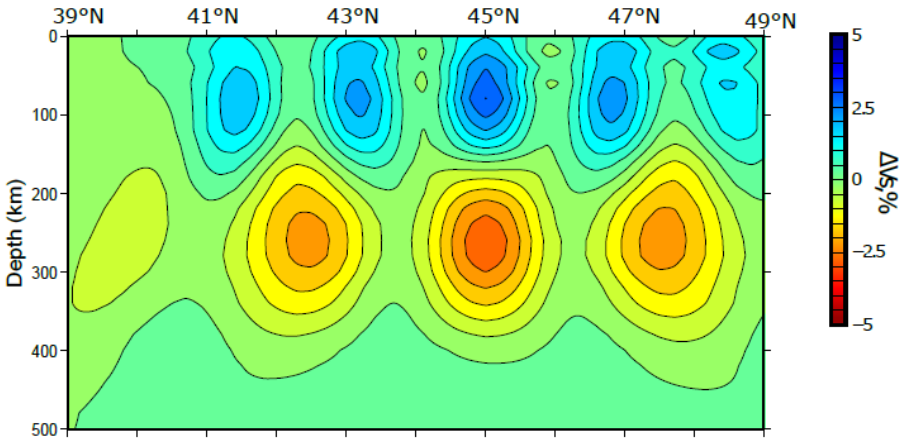

Figure S13. Same as Figure S12g, but from an inversion that applied a weaker vertical smoothing constrain.

Text S6: Synthetic test of a sharp gradient near the JdF Ridge

Figure S14 demonstrates the ability of our inversion to recover a gradient in *Vs* near the JdF Ridge. We performed an inversion of delay times predicted for a low velocity region that extended 75 km east of the JdF Ridge and sharply transitioned to higher velocities (Figure S14a). Anomalies in the input model extended from the surface to 150 km depth and had values of positive and negative 5%.

The low *Vs* anomaly and the gradient on the eastern flank are well recovered along the full length of the JdF Ridge. We conclude that increase in *Vs* north of the Cobb offset and the eastward offsets of the gradient near the northern and southern JdF Ridge in the preferred model are robust. In addition, for the synthetic inversion the magnitude of the gradient is higher and the width of the gradational region narrower than in the preferred model (Figure S14b), suggesting that the true gradient near the JdF Ridge may be wider than the instantaneous gradient used in this test. The recovered gradients west of the ridge broaden to the west where there is no station coverage.

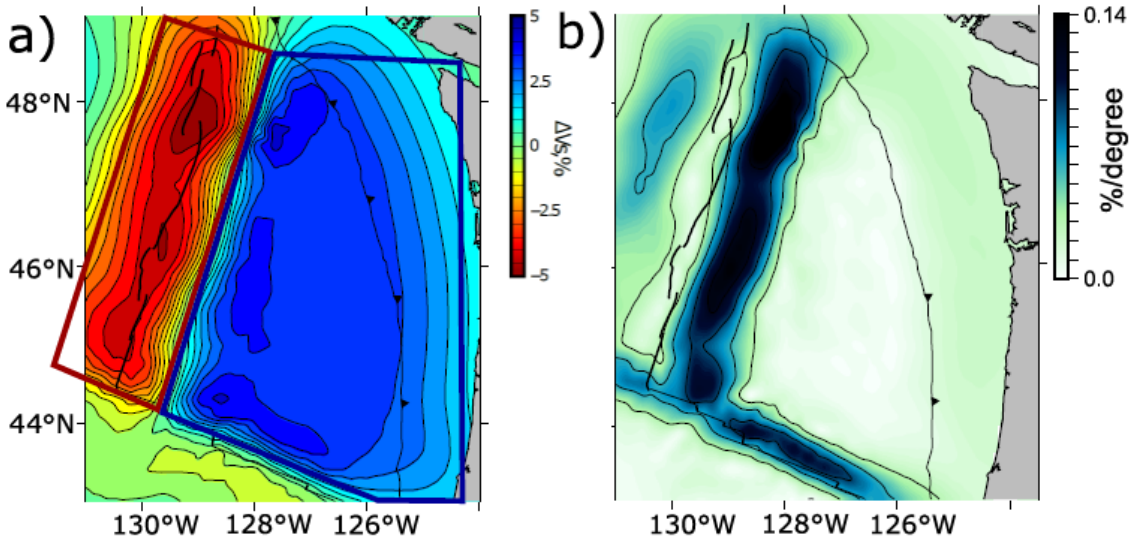

Figure S14. Inversion of synthetic delay times generated for a model that included a sharp, off-axis gradient. a) Recovered anomalies averaged over the upper 200 km are contoured and the outlines of the input velocity anomalies are shown by the red and blue polygons. b) The magnitude of the gradient of the anomalies in a). Contour interval is 0.03 %/degree.

APPENDIX C

CHAPTER IV APPENDIX A AND SUPPLEMENTAL FIGURES

Appendix A. Markov Chain Monte Carlo Search

We used a Markov Chain Monte Carlo algorithm to explore models of seismic anisotropy that satisfy results from both receiver functions and *SKS* splitting. Our approach closely follows that of *Shen et al*., [2013] (see also *Sambridge et al.* [2002]). The algorithm searches parameter space by first evaluating the fit to the data of a randomly chosen starting model. Then, a new model is chosen by perturbing each parameter of the starting model. The new model is evaluated and the results are saved. If the fit to the data of the new model is better than the fit of the starting model, the new model is accepted; if the fit is degraded, either the new or starting model may be accepted (see *Shen et al*., [2013] for a discussion). This process is repeated with the accepted model in the role of the starting model. This process guides the search towards models that fit the data well, while sometimes selecting inferior models to escape local minima. Instead of attempting to identify a best model, we draw inferences about acceptable values of parameters by analyzing the range of values in the ensemble of valid models.

Our approach deviated from the algorithm of *Shen et al.* [2013] in two ways. First, we drew starting models from a uniform distribution, instead of a Gaussian distribution centered on values from previously published studies. Second, we did not estimate the *a posteriori* probabilities for model parameters from the results of the search with Bayes' theorem. The uniform distribution is not a physically motivated *a priori* probability distribution for model parameters. To our knowledge,

quantitative, *a priori* constrains on mantle anisotropy at specific depths in our region of interest do not exist. Instead, we sought to eliminate possible regions of parameter space from consideration to constrain the ranges of model parameters consistent with two sets of seismic observations.

During the search, we evaluated the fit of model predictions to seismic observations by the misfit function

$$\chi^2 = (\chi_R^2 + \chi_S^2 + \chi_D)/2 \quad \text{(A1)}$$

where χ^2 is the total misfit, χ_R^2 is the misfit to the receiver function results, χ_S^2 is the misfit to the *SKS* splitting results, and χ_D is the absolute value of the difference between χ_R^2 and χ_S^2. The χ_D term steered the search away from regions of parameter space that over-fit one dataset while under-fitting another. We evaluated the first term, χ_R^2, by squaring the same misfit used for the single layer grid search described in Section 3.3. We evaluated the fit to the *SKS* splitting results by

$$\chi_S^2 = \left(\sum_{k=1}^{k=M}(T_O - T_p)^2 + \sum_{k=1}^{k=M}(F_O - F_p)^2\right)/2 \quad \text{(A2)}$$

where T_O and T_p are observed and predicted splitting times, F_O and F_p are the observed and predicted fast directions, k is the index of a back-azimuth used, and M is the total number of back-azimuths used. The input *SKS* splitting parameters were splitting times of 1 ± 0.25 s and fast polarization directions of 60 ± 10° at back-azimuths of 140°, 275°, and 325° [*Bodmer et al.*, 2015]. We assumed a horizontal slowness of 0.04 s/km for the *SKS* phases. The rotation-correlation method [*Silver and Chan*, 1991; *Wüstefeld et al.,* 2008] was used to evaluate the splitting parameters for synthetic waveforms generated with the same reflectivity algorithm used for the receiver functions [*Park*, 1996; *Levin and Park*, 1998].

The model parameters that were searched over are summarized in Table 1. We initialized the search at 50 stating points, each with model parameters randomly chosen from with the initial ranges listed in Table 1. The search was iterated 200 times from each starting point, and the standard deviation of the perturbations at each step was set to 5% of the initial range. We consider models with χ^2 below 1 for both the receiver function and *SKS* fits as consistent with the data; of the 10,000 models tested, 802 passed this condition. Because the uncertainties were 95% confidence intervals, a model with a fit of 1 is consistent with both sets of data at the 95% confidence interval.

Text S1. Implied incidence angles of *SV* phases

Figure S1 shows a histogram of the implied surface velocities discussed in Section 2. The implied surface velocities are approximately Gaussian within the range of 1 to 6 km/s, with outliers that extend to 0 and 10 km/s (Figure S1a). Station-event pairs with outlying implied surface velocities were removed from analysis; these traces generally have questionable signal-to-noise ratios. The test provides an objective quality-control step on subjectively selected data. No trend is observed with the predicted slowness of the incoming wave and the implied surface velocity (Figure S1b), which confirms this quantity is independent of epicentral distance, unlike the measured incidence angles themselves.

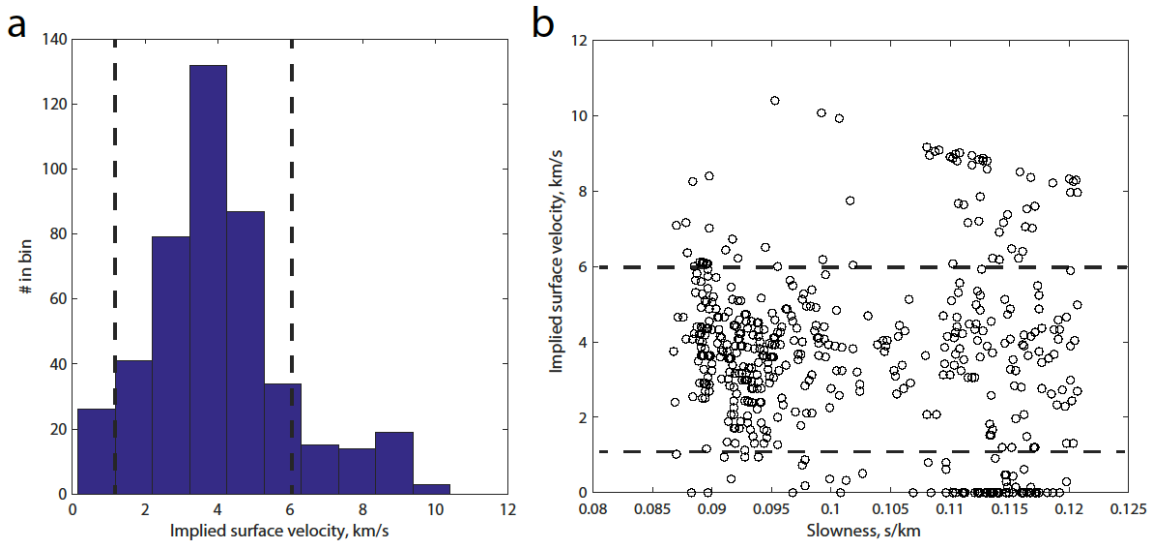

Figure S1. Implied surface velocities of *SV* phases. a) Histogram of the implied surface velocities. Dashed lines shows the range of acceptable values. b) Implied surface velocities by the predicted horizontal slowness of the *SV* phase. The dashed lines show the range of acceptable values.

Text S2. Subsets of three stacks

Smaller regions do not provide statistically distinct receiver functions from the results shown in the main text. Subsets of the three stacks shown in Figure 4 are shown in Figures S2-S8. Subsets are taken from the northern and southern JdF plate, from either side of the ridges, and between the JdF-Ridge and JdF-plate stacks. In each case, the subsets are not distinct from the stacks of broader regions and the uncertainties are approximately double that for the larger stacks. The *S*140*p* phase is observed with increased uncertainty in both subsets of the JdF-plate stack (Figure S2 and S3). Robust asymmetries about neither ridge axis are observed (Figure S4-S7). The most significant deviation in a subset is observed in Figure S8, where the *S*140*p* phase may be not be robust in the subset stack from the region between the JdF-Ridge and JdF-plate stacks.

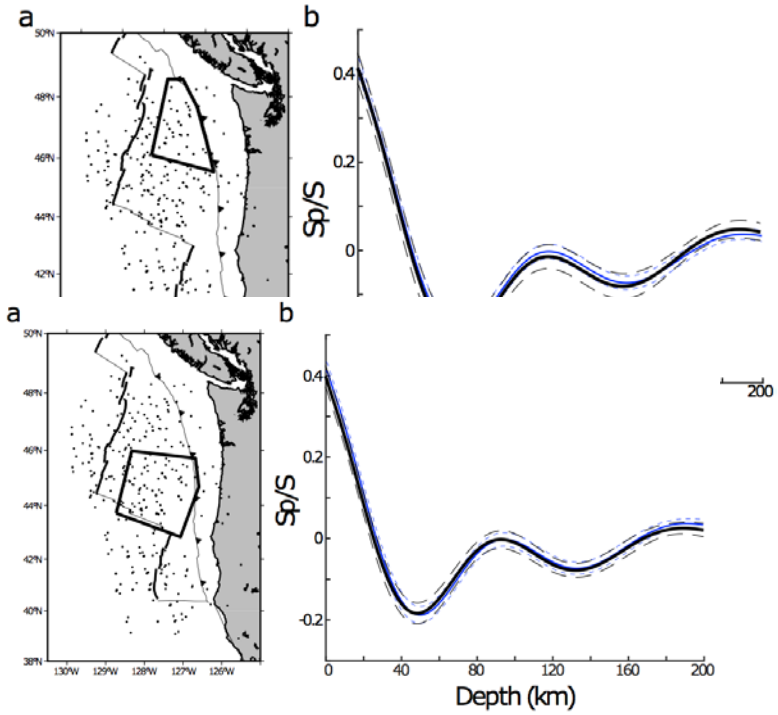

Figure S2. Subset of the receiver functions from the northern JdF plate. a) Piercing points of all receiver functions at 140 km depth. The region where the subset was taken from is shown by the black box. b) Comparison between the JdF-plate stack and its uncertainty, in solid and dashed blue lines respectively, with the subset for the northern JdF plate and its uncertainty, in solid and dashed black lines respectively.

Figure S3. Subset of the receiver functions from the southern JdF plate. a) Piercing points of all receiver functions at 140 km depth. The region where the subset was taken from is shown by the black box. b) Comparison between the JdF-plate stack and its uncertainty, in solid and dashed blue lines respectively, with the subset for the southern JdF plate and its uncertainty, in solid and dashed black lines respectively.

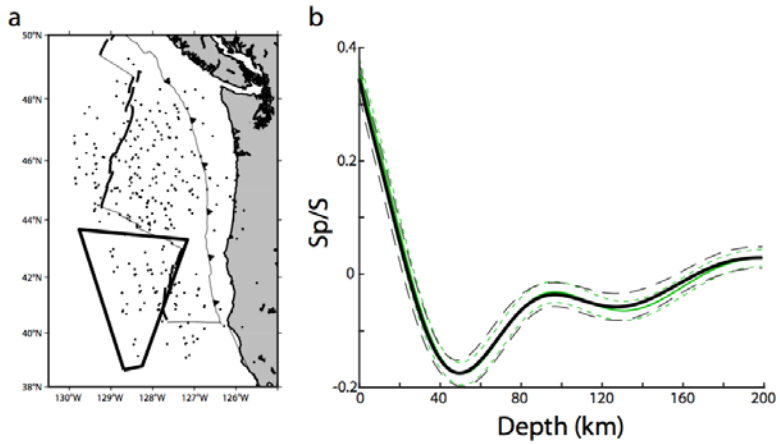

Figure S4. Subset of the receiver functions from beneath the western flank of the Gorda Ridge. a) Piercing points of all receiver functions at 140 km depth. The region where the subset was taken from is shown by the black box. b) Comparison between the Gorda stack and its uncertainty, in solid and dashed green lines respectively, with the subset for the western flank of the Gorda Ridge and its uncertainty, in solid and dashed black lines respectively.

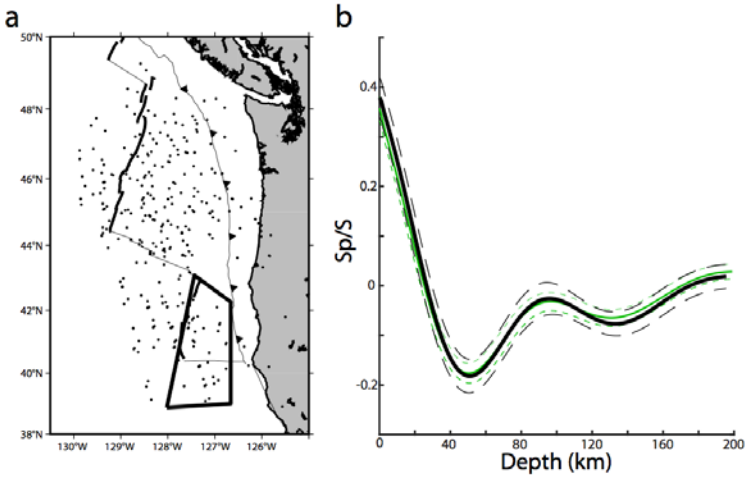

Figure S5. Subset of the receiver functions from beneath the eastern flank of the Gorda Ridge. a) Piercing points of all receiver functions at 140 km depth. The region where the subset was taken from is shown by the black box. b) Comparison between the Gorda stack and its uncertainty, in solid and dashed green lines respectively, with the subset for the eastern Gorda Ridge its uncertainty, in solid and dashed black lines respectively.

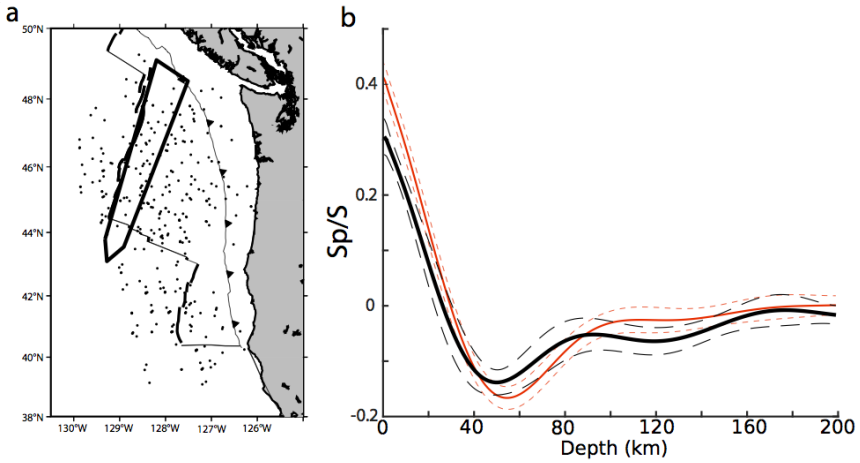

Figure S6. Subset of the receiver functions from beneath the eastern flank of the JdF Ridge. a) Piercing points of all receiver functions at 140 km depth. The region where the subset was taken from is shown by the black box. b) Comparison between the JdF-Ridge stack and its uncertainty, in solid and dashed red lines respectively, with the subset for the eastern flank of the JdF Ridge and its uncertainty, in solid and dashed black lines respectively.

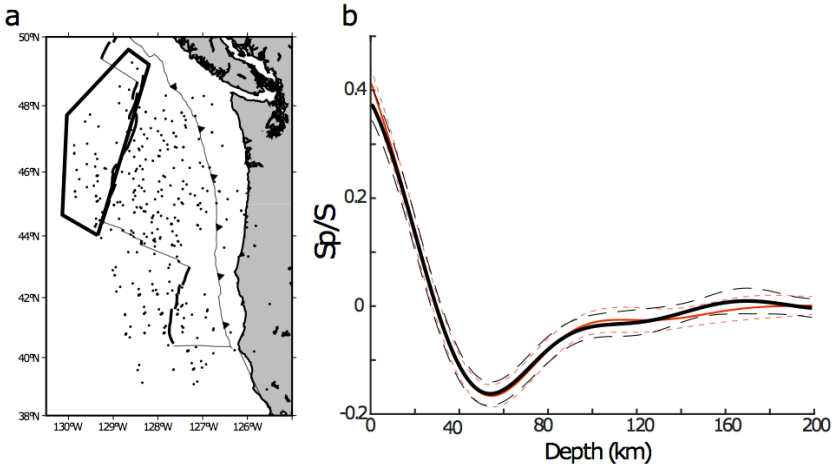

Figure S7. Subset of the receiver functions from beneath the western flank of the JdF Ridge. a) Piercing points of all receiver functions at 140 km depth. The region where the subset was taken from is shown by the black box. b) Comparison between the JdF-Ridge stack and its uncertainty, in solid and dashed red lines respectively, with the subset for the western flank of the JdF Ridge and its uncertainty, in solid and dashed black lines respectively.

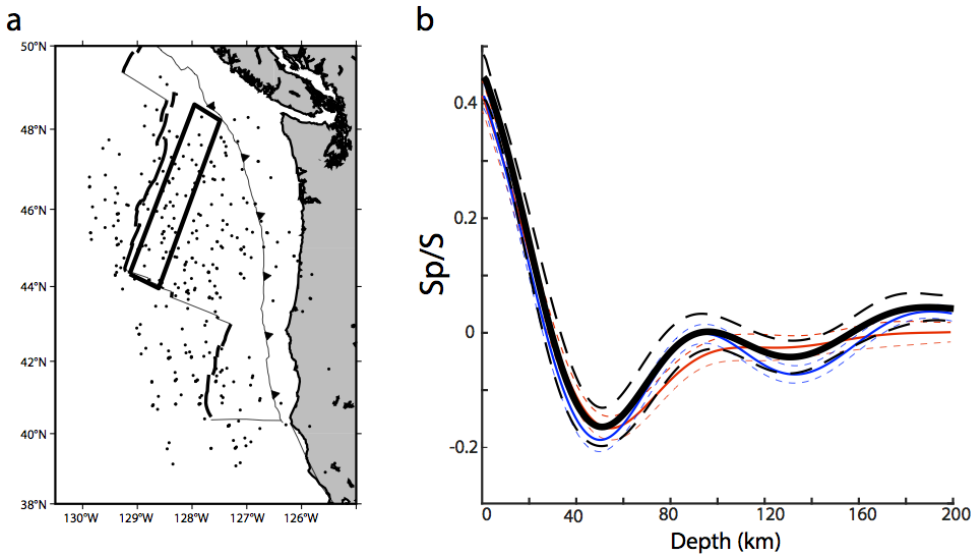

Figure S8. Subset of the receiver functions from the region in between the JdF Ridge and plate stacks. a) Piercing points of all receiver functions at 140 km depth. The region where the subset was taken from is shown by the black box. b) Comparison between the JdF-plate stack and its uncertainty, in solid and dashed blue lines respectively, the JdF-Ridge stack and its uncertainty, in solid and dashed red lines respectively, and the subset receiver function and its uncertainty, in solid and dashed black lines, respectively.

Text S3. Conversions from *SH* phases

Figure S9 shows the predicted *SH*-to-*p* receiver function for the model shown in Figure 8a,b. For isotropic velocity models, no *SH* conversions will occur, but *p* conversions will occur at contrasts in anisotropy. However, the small amplitude of the dashed line in Figure S9 confirms that the stacking procedure described in the main text suppresses conversions from the *SH* component of the incoming wavefield.

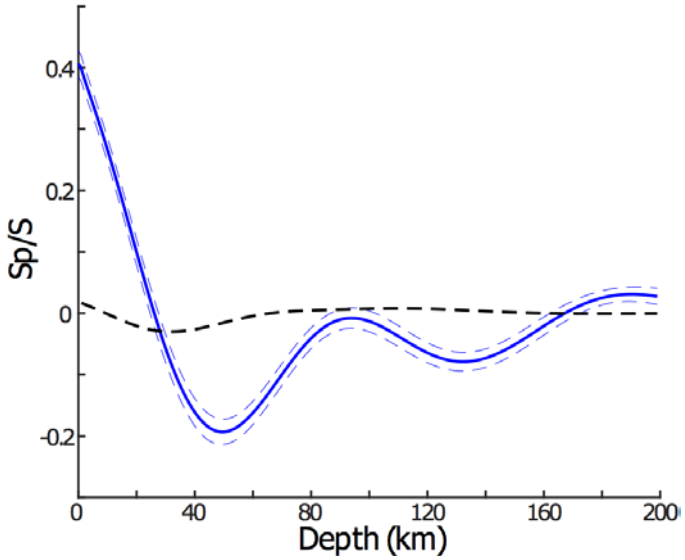

Figure S9. *SH*-to-*p* conversions for the stacking procedure used in the main text. The solid and dashed blue lines shows the JdF-plate stack and its uncertainty, respectively, and the dashed black lines show the predicted stack of *SH*-to-*p* conversions for the model shown in Figure 8a,b.

Text S4. Effect of a tilted fast axis on the amplitude of *S*-to-*p* phases

The effect of a tilted fast axis on the predicted amplitudes of *S*-to-*p* phases is explored in Figure S10. In Section 3.3 of the main text, the fast axis is assumed to be horizontal (90°). Both Figures S10a and S10b are identical to Figure 7a of the main text, expect that a tilt of 70° and 45°, respectively, was assumed. When the tilt of the fast axis is 70°, the amplitudes of the *S*140*p* phases are moderately reduced relative to the results in Figure 7a. However, the dependence of the amplitudes on the azimuth of the fast direction is unchanged (cf. with Figure 7a). When the tilt is 45°, no significant *S*140*p* phase is observed. We assumed a fixed horizontal fast axis in the main text, with the caveat that larger contrasts in anisotropy at the L discontinuity will be required if the fast axis is tilted.

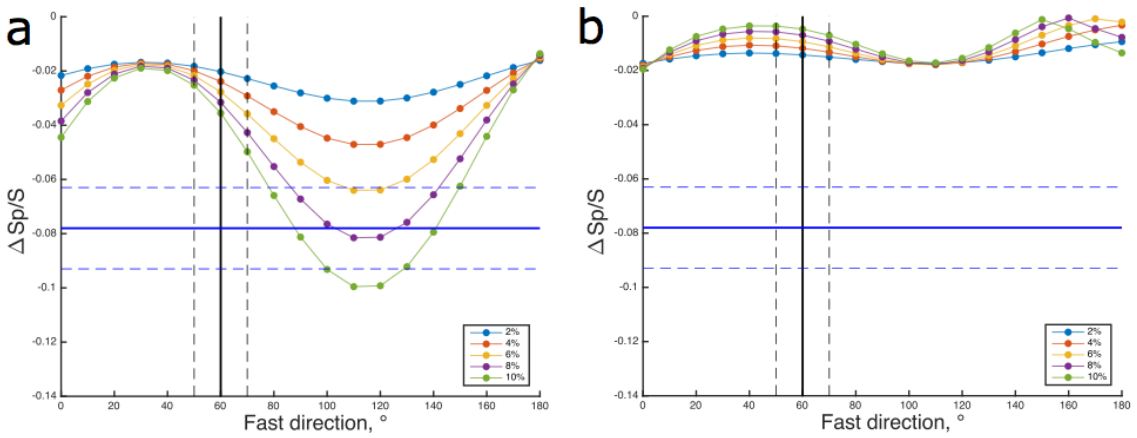

Figure S10. Effect of a tilted fast axis on the amplitude of *S*-to-*p* converted phases. Colored lines with circles show the predicted amplitude of the *S*140*p* phase, relative to the maxima near 90 km depth, for a decreases in the magnitude of *S* anisotropy at 140 km depth with different fast directions. The solid and dashed black lines show the fast polarization direction from *SKS* splitting for the JdF plate and its uncertainty, respectively. The solid and dashed blue lines show the relative amplitude of the *S*140*p* phase in the JdF-plate stack and its uncertainty, respectively. a) Same as Figure 7a, expect that the fast axis had a tilt of 70°. b) Same as Figure 7a, expect that the fast axis had a tilt of 45°.

REFERENCES CITED

Chapter II

Abers, G. A., K. M. Fischer, G. Hirth, D. A. Wiens, T. Plank, B. K. Holtzman, C. McCarthy, and E. Gazel (2014), Reconciling mantle attenuation-temperature relationships from seismology, petrology, and laboratory measurements, *Geochem. Geophys. Geosyst.*, *15*, 3521–3542, doi:10.1002/2014GC005444.

Abt, D. L., K. M. Fischer, S. W. French, H. A. Ford, H. Yuan, and B. Romanowicz (2010), North American lithospheric discontinuity structure imaged by Ps and Sp receiver functions, *J. Geophys. Res.*, *115*, B09301, doi:10.1029/2009JB006914.

Afonso, J. C., and D. L. Schutt (2012), The effects of polybaric partial melting on density and seismic velocities of mantle restites, *Lithos*, *134*, 289–303, doi:10.1016/j.lithos.2012.01.009.

Aizawa, Y., A. Barnhoorn, U. H. Faul, J. D. F. Gerald, I. Jackson, and I. Kovács (2008), Seismic properties of Anita Bay dunite: An exploratory study of the influence of water, *J. Petrol.*, *49*, 841–855, doi:10.1093/petrology/egn007.

Anderson, D. L., and J. W. Given (1982), Absorption band Q model for the Earth, *J. Geophys. Res.*, *87*, 3893–3904, doi:10.1029/JB087iB05p03893.

Asimow, P. D., and C. H. Langmuir (2003), The importance of water to oceanic mantle melting regimes, *Nature*, *421*, 815–820, doi:10.1038/nature01429.

Asimow, P. D., J. E. Dixon, and C. H. Langmuir (2004), A hydrous melting and fractionation model for mid-ocean ridge basalts: Application to the Mid-Atlantic Ridge near the Azores, *Geochem. Geophys. Geosyst.*, *5*, Q01E16, doi:10.1029/2003GC000568.

Bagley, B., and J. Revenaugh (2008), Upper mantle seismic shear discontinuities of the Pacific, *J. Geophys. Res.*, *113*, B12301, doi:10.1029/2008JB005692.

Barckhausen, U., C. R. Ranero, R. von Huene, S. C. Cande, and H. A. Roeser (2001), Revised tectonic boundaries in the Cocos plate off Costa Rica: Implications for the segmentation of the convergent margin and for plate tectonic models, *J. Geophys. Res.*, *106*, 19,207–19,220, doi:10.1029/2001JB000238.

Beghein, C., K. Yuan, N. Schmerr, and Z. Xing (2014), Changes in seismic anisotropy shed light on the nature of the Gutenberg discontinuity, *Science*, *343*, 1237–1240, doi:10.1126/science.12467234.

Braun, M. G., G. Hirth, and E. M. Paramentier (2000), The effects of deep damp melting on mantle flow and melt generation beneath mid-ocean ridges, *Earth*

Planet. Sci. Lett., *176*, 339–356, doi:10.1016/S0012-821X(00)00015-7.

Brocher, T. M. (2005), Empirical relations between elastic wavespeeds and density in the Earth's crust, *Bull. Seismol. Soc. Am.*, *95*, 2081–2092, doi:10.1785/0120050077.

Chan, W. W., I. S. Sacks, and R. Morrow (1989), Anelasticity of the Iceland Plateau from surface wave analysis, *J. Geophys. Res.*, *94*, 5675–5688, doi:10.1029/JB094iB05p05675.

Choblet, G., and E. M. Parmentier (2001), Mantle upwelling and melting beneath slow spreading centers: Effects of variable rheology and melt productivity, *Earth Planet. Sci. Lett.*, *184*, 589–604, doi:10.1016/S0012-821X(00)00330-7.

Collins, J. A., F. L. Verson, J. A. Orcutt, and R. A. Stephen (2002), Upper mantle structure beneath the Hawaiian swell: Constraints from the Ocean Seismic Network Pilot Experiment, *Geophys. Res. Lett.*, *29*, 1522, doi:10.1029/2001GL013302.

Cushman, B., J. Sinton, G. Ito, and J. E. Dixon (2004), Glass compositions, plume-ridge interaction, and hydrous melting along the Galápagos Spreading Center, *Geochem. Geophys. Geosyst.*, *5*, Q08E17, doi:10.1029/2004GC000709.

Dasgupta, R., M. M. Hirschmann, and N. D. Smith (2007), Water follows carbon: CO_2 incites deep silicate melting and dehydration beneath mid-ocean ridge, *Geology*, *35*, 135–138, doi:10.1130/G22856A.1.

Detrick, R. S., and S. T. Crough (1978), Island subsidence, hot spots, and lithospheric thinning, *J. Geophys. Res.*, *83*, 1236–1244, doi:10.1029/JB083iB03p01236.

Detrick, R. S., J. M. Sinton, G. Ito, J. P. Canales, M. Behn, T. Blacic, B. Cushman, J. E. Dixon, D. W. Graham, and J. J. Mahoney (2002), Correlated geophysical, geochemical, and volcanological manifestations of plume-ridge interaction along the Galápagos Spreading Center, *Geochem. Geophys. Geosyst.*, *3*, 1–14, doi:10.1029/2002GC000350.

Dueker, K. G., and A. F. Sheehan (1998), Mantle discontinuity structure beneath the Colorado Rocky Mountains and high plains, *J. Geophys. Res.*, *103*, 7153–7169, doi:10.1029/97JB03509.

Faul, U. H., and I. Jackson (2005), The seismological signature of temperature and grain size variations in the upper mantle, *Earth Planet. Sci. Lett.*, *234*, 119–134, doi:10.1016/j.epsl.2005.02.008.

Faul, U. H., J. D. Fitzgerald, and I. Jackson (2004), Shear wave attenuation and dispersion in melt-bearing olivine polycrystals: 2. Microstructureal interpretation

and seismological implications, *J. Geophys. Res.. 109*, B06202, doi:10.1029/2003JB002407.

Fischer, K. M., H. A. Ford, D. L. Abt, and C. A. Rychert (2010), The lithosphere-asthenosphere boundary, *Annu. Rev. Earth Planet. Sci.*, *38*, 551–575, doi:10.1146/annurev-earth-040809-152438.

Fisk, M. R., A. E. Bence, and J. G. Schilling (1982), Major element chemistry of Galápagos rift zone magmas and their phenocrysts, *Earth Planet. Sci. Lett.*, *61*, 171–189, doi:10.1016/0012-821X(82)90050-4.

Gaherty, J. B., T. H. Jordan, and L. S. Gee (1996), Seismic structure of the upper mantle in a central Pacific corridor, *J. Geophys. Res.*, *101*, 22,291–22,309, doi:10.1029/96JB01882.

Gaherty, J., M. Kato, and T. H. Jordan (1999), Seismological structure of the upper mantle: A regional comparison of seismic layering, *Phys. Earth Planet. Inter., 110*, 21–41, doi:10.1016/S0031-9201(98)00132-0.

Ghahremani, F. (1980), Effect of grain boundary sliding on anelasticity of polycrystals, *Int. J. Solids Structures*, *16*, 825–845, doi:10.1016/0020-7683(80)90052-9.

Gibson, S. A., and D. Geist (2010), Geochemical and geophysical estimates of lithospheric thickness variation beneath Galápagos, *Earth Planet. Sci. Lett.*, *300*, 275–286, doi:10.1016/j.epsl.2010.10.002.

Graham, D. W., D. M. Christie, K. S. Harpp, and J. E. Lupton (1993), Mantle plume helium in submarine basalts from the Galápagos platform, *Science*, *262*, 2023–2026, doi: 10.1126/science.262.5142.2023.

Gripp, A. E., and R. G. Gordon (2002), Young tracks of hotspots and current plate velocities, *Geophys. J. Int.*, *150*, 321–361, doi:10.1046/j.1365-246X.2002.01627.x.

Gutenberg, B. (1948), On the relatively low wave velocity at depth of about 80 kilometers, *Bull. Seismol. Soc. Am.*, *38*, 121–147.

Hall, P. S., and C. Kincaid (2003), Melting, dehydration, and the dynamics of off-axis plume-ridge interaction, *Geochem. Geophys. Geosyst.*, *4*, 8510, doi:10.1029/2003GC000567.

Hammond, W. C., and E. D. Humphreys (2000), Upper mantle seismic wave velocity: Effects of realistic partial melt geometries, *J. Geophys. Res.*, *105*, 10,975–10,986, doi:10.1029/2000JB900041.

Hansen, S., and K. Dueker (2009), P-and S-wave receiver function images of

crustal imbrication beneath the Cheyenne Belt in southeast Wyoming, *Bull. Seismol. Soc. Am.*, *99*, 1953–1961, doi:10.1785/0120080168.

Harpp, K. S., and W. M. White (2001), Tracing a mantle plume: Isotopic and trace element variations of Galápagos seamounts, *Geochem. Geophys. Geosyst.*, *2*, 2000GC000137, doi:10.1029/2000GC000137.

Havlin, C., and E. M. Parmentier (2014), Implications for melt transport and source heterogeneity in upwelling mantle from the magnitude of S_p converted phases generated at the onset of melting, *Geophys. Res. Lett.*, *34*, 5444–5450, doi:10.1002/2014GL060890.

Heit, B., F. Sodoudi, X. Yuan, M. Bianchi, and R. Kind (2007), An S receiver function analysis of the lithospheric structure in South America, *Geophys. Res. Lett.*, *34*, L14307, doi:10.1029/2007GL030317.

Helffrich, G. (2006), Extended-time multitaper frequency domain cross-correlation receiver-function estimation, *Bull. Seismol. Soc. Am.*, *96*, 344–347, doi:10.1785/0120050098.

Herzberg, C., and E. Gazel (2009), Petrological evidence for secular cooling in mantle plumes, *Nature*, *458*, 619–622, doi:10.1038/nature07857.

Herzberg, C., P. Raterron, and J. Zhang (2000), New experimental observations on the anhydrous solidus for peridotite KLB-1, *Geochem. Geophys. Geosyst., 1,* 2000GC000089, doi: 10.1029/2000GC000089

Hey, R., and P. Vogt (1977), Spreading-center jumps and sub-axial asthenosphere flow near the Galápagos hotspot, *Tectonophysics*, *37*, 41-52, doi:10.1016/0040-1951(77)90038-5.

Hirschmann, M. M. (2010), Partial melt in the oceanic low velocity zone, *Phys. Earth Planet. Inter.*, *179*, 60–71, doi:10.1016/j.pepi.2009.12.003.

Hirschmann, M. M., T. Tenner, C. Aubaud, and A. C. Withers (2009), Dehydration melting of nominally anhydrous mantle: The primacy of partitioning, *Phys. Earth Planet. Inter.*, 176, 54–68, doi:10.1016/j.pepi.2009.04.001.

Hirth, G., and D. L. Kohlstedt (1996), Water in the oceanic upper mantle: Implications for rheology, melt extraction and the evolution of the lithosphere, *Earth Planet. Sci. Lett.*, *144*, 93–108, doi:10.1016/0012-821X(96)00154-9.

Hooft, E. E., D. R. Toomey, and S. C. Solomon (2003), Anomalously thin transition zone beneath the Galápagos hotspot, *Earth Planet. Sci. Lett.*, *216*, 55–64, doi:10.1016/S0012-821X(03)00517-X.

Ingle, S., G. Ito, J. J. Mahoney, W. Chazey III, J. Sinton, M. Rotella, and D. M.

Christie (2010), Mechanisms of geochemical and geophysical variations along the western Galápagos Spreading Center, *Geochem. Geophys. Geosyst., 11*, Q04003, doi:10.1029/2009GC002694.

Ito, G., and J. Lin (1995), Mantle temperature anomalies along the past and paleoaxes of the Galápagos spreading center as inferred from gravity analyses, *J. Geophys. Res., 100,* 3733–3745.

Jackson, I., and U. H. Faul (2010), Grainsize-sensitive viscoelastic relaxation in olivine: Towards a robust laboratory-based model for seismological application, *Phys. Earth Planet. Inter.*, *183*, 151–163, doi:10.1016/j.epsl.2005.02.008.

Jackson, I., M. S. Paterson, and J. D. Fitz Gerald (1992), Seismic wave dispersion and attenuation in Åheim dunite: An experimental study, *Geophys. J. Int.*, *108*, 517–534, doi:10.1111/j.1365-246X.1992.tb04633.x.

Karato, S. (1986), Does partial melting reduce the creep strength of the upper mantle?, *Nature*, *319*, 309–310, doi:10.1038/319309a0.

Karato, S.-I. (2012), On the origin of the asthenosphere, *Earth Planet. Sci. Lett.*, *321*, 95–103, doi:10.1016/j.epsl.2012.01.001.

Karato, S.-I. (2014), Does partial melting explain geophysical anomalies? *Phys. Earth Planet. Inter.*, *228*, 300-306, doi:10.1016/j.pepi.2013.08.006.

Karato, S.-I., and H. Jung (1998), Water, partial melting and the origin of the seismic low velocity and high attenuation zone in the upper mantle, *Earth Planet. Sci. Lett.*, *157*, 193–207, doi:10.1016/S0012-821X(98)00034-X.

Katz, R. F., Spiegelman, M., and Langmuir, C. H. (2003), A new parameterization of hydrous mantle melting, *Geochem. Geophys. Geosyst.*, *4,* 1073, doi:10.1029/2002GC000433.

Kawakatsu, H., P. Kumar, Y. Takei, M. Shinohara, T. Kanazawa, E. Araki, and K. Suyehiro (2009), Seismic evidence for sharp lithosphere-asthenosphere boundaries of oceanic plates, *Science*, *324*, 499–502, doi:10.1126/science.1169499.

Kind, R., X. Yuan, and P. Kumar (2012), Seismic receiver functions and the lithosphere–asthenosphere boundary, *Tectonophysics*, *536-537*, 25–43, doi:10.1016/j.tecto.2012.03.005.

Koleszar, A. M., A. E. Saal, E. H. Hauri, A. N. Nagle, Y. Liang, M. D. Kurz (2009), The volatile contents of the Galápagos plume; evidence for H_20 and F open system behavior in melt inclusions, *Earth Planet. Sci. Lett.*, *287*, 442-452, doi:10.1016/j.epsl.2009.08.029.

Kumar, P., and H. Kawakatsu (2011), Imaging the seismic lithosphere-

asthenosphere boundary of the oceanic plate, *Geochem. Geophys. Geosyst.*, *12*, Q01006, doi:10.1029/2010GC003358.

Kumar, P., R. Kind, W. Hanka, K. Wylegalla, C. Reigber, X. Yuan, I. Woelbern, P. Schwintzer, K. Fleming, and T. Dahl-Jensen (2005), The lithosphere–asthenosphere boundary in the North-West Atlantic region, *Earth Planet. Sci. Lett.*, *236*, 249–257, doi:10.1016/j.epsl.2005.05.029.

Kumar, P., X. Yuan, M. R. Kumar, R. Kind, X. Li, and R. K. Chadha (2007), The rapid drift of the Indian tectonic plate, *Nature*, *449*, 894–897, doi:10.1038/nature06214.

Kurz, M. D., and D. Geist (1999), Dynamics of the Galápagos hotspot from helium isotope geochemistry, *Geochim. Cosmochim. Acta*, *63*, 4139–4156, doi:10.1016/S0016-7037(99)00314-2.

Lee, C. A., P. Luffi, T. Plank, H. Dalton, and W. P. Leeman (2008), Constrains on the depths and temperatures of basaltic magma generation on Earth and other terrestrial planets using new thermobarometers for mafic magma, *Earth Planet. Sci. Lett.*, *279*, 20–33, doi: 10.1016/j.epsl.2008.12.020.

Levin, V., and J. Park (1998), P-SH conversions in layered media with hexagonally symmetric anisotropy: A cookbook, *Pure Appl. Geophys.*, *151*, 669–697, doi:10.1007/s000240050136.

Li., A., and R. S. Detrick (2006), Seismic structure of Iceland from Rayleigh wave inversions and geodynamic implications, *Earth Planet. Sci. Lett., 241,* 901–912, doi:10.1016/j.epsl.2005.10.031.

Li, X., X. Yuan, and R. Kind (2007), The lithosphere-asthenosphere beneath the western United States, *Geophys. J. Int.*, *170*, 700–710, doi:10.1111/j.1365-246X.2007.03428.x.

Li, X., R. Kind, X. Yuan, I. Wölbern, and W. Hanka (2004), Rejuvenation of the lithosphere by the Hawaiian plume, *Nature*, *427*, 827–829, doi:10.1038/nature02349.

Lodge, A., and G. Helffrich (2006), Depleted swell root beneath the Cape Verde Islands, *Geology*, *34*, 449–452, doi:10.1130/G22030.1.

Matsukage, K. N., Y. Nishihara, and S.-I. Karato (2005), Seismological signature of chemical differentiation of Earth's upper mantle, *J. Geophys. Res.*, *110*, B12305, doi:10.1029/2004JB003504.

McKenzie, D. (1984), The generation and compaction of partially molten rock, *J. Petrol.*, *25*, 713–765, doi:10.1093/petrology/25.3.713.

McKenzie, D., and M. J. Bickle (1988), The volume and composition of melt generated by extension of the lithosphere, *J. Petrol.*, *29*, 625–679, doi:10.1093/petrology/29.3.625.

Mittelstadt, E., G. Ito, and J. van Hunen (2011), Repeat ridge jumps associated with plume-ridge interaction, melt transport, and ridge migration, *J. Geophys. Res.*, *116*, B01102, doi:10.1029/2010JB007504.

Morris, S. J. S., and I. Jackson (2009), Diffusionally assisted grain-boundary sliding and viscoelasticity of polycrystals, *J. Mech. Phys. Solids*, *57*, 744–761, doi:10.1016/j.jmps.2008.12.006.

Park, J. (1996), Surface waves in layered anisotropic structures, *Geophys. J. Int.*, *126*, 173–183, doi:10.1111/j.1365-246X.1996.tb05276.x.

Park, J., and V. Levin (2000), Receiver functions from multiple-taper spectral correlation estimates, *Bull. Seismol. Soc. Am.*, *90*, 1507–1520, doi:10.1785/0119990122.

Park, J., C. R. Lindberg, and F. L. Vernon (1987), Multitaper spectral analysis of high-frequency seismograms, *J. Geophys. Res.*, *92*, 12,675–12,684, doi:10.1029/JB092iB12p12675.

Parsons, B., and D. McKenzie (1978), Mantle convection and the thermal structure of the plates, *J. Geophys. Res.*, *83*, 4485–4496, doi:10.1029/JB083iB09p04485.

Phipps Morgan, J. (1997), The generation of a compositional lithosphere by mid-ocean ridge melting and its effect on subsequent off-axis hotspot upwelling and melting, *Earth Planet. Sci. Lett.*, *146*, 213–232, doi:10.1016/S0012-821X(96)00207-5.

Phipps Morgan, J., W. J. Morgan, and E. Price (1995), Hotspot melting generates both hotspot volcanism and a hotspot swell?, *J. Geophys. Res.*, *100*, 8045–8062, doi:10.1029/94JB02887.

Rychert, C. A., and P. M. Shearer (2009), A global view of the lithosphere-asthenosphere boundary, *Science*, *324*, 495–498, doi:10.1126/science.1169754.

Rychert, C. A., and P. M. Shearer (2011), Imaging the lithosphere-asthenosphere boundary beneath the Pacific using SS waveform modeling, *J. Geophys. Res.*, *116*, B07307, doi:10.1029/2010JB008070.

Rychert, C. A., K. M. Fischer, and S. Rondenay (2005), A sharp lithosphere–asthenosphere boundary imaged beneath eastern North America, *Nature*, *436*, 542–545, doi:10.1038/nature03904.

Rychert, C. A., S. Rondenay, and K. M. Fischer (2007), P-to-S and S-to-P imaging of a sharp lithosphere-asthenosphere boundary beneath eastern North America, *J. Geophys. Res.*, *112*, B08314, doi:10.1029/2006JB004619.

Rychert, C. A., P. M. Shearer, and K. M. Fischer (2010), Scattered wave imaging of the lithosphere–asthenosphere boundary, *Lithos*, *120*, 173–185, doi:10.1016/j.lithos.2009.12.006.

Rychert, C. A., N. Schmerr, and N. Harmon (2012), The Pacific lithosphere-asthenosphere boundary: Seismic imaging and anisotropic constraints from SS waveforms, *Geochem. Geophys. Geosyst.*, *13*, Q0AK10, doi:10.1029/2012GC004194.

Rychert, C. A., G. Laske, N. Harmon, and P. M. Shearer (2013), Seismic imaging of melt in a displaced Hawaiian plume, *Nature Geosci.*, *6*, 657-660, doi:10.1038/ngeo1878.

Rychert, C. A., N. Harmon, and C. Ebinger (2014), Receiver function imaging of lithospheric structure and the onset of melting beneath the Galápagos Archipelago, *Earth Planet. Sci. Lett.*, *388*, 156–165, doi:10.1016/j.epsl.2013.11.027.

Schilling, J. (1991) Fluxes and excess temperatures of mantle plumes inferred from their interaction with migrating mid-ocean ridges, *Nature*, *352*, 397–403.

Schilling, J., R. Kingsley, and J. Devine (1982), Galápagos hot spot-spreading center system, 1. Spatial petrological and geochemical variations (83°W–101°W), *J. Geophys. Res., 87*, 5593–5610.

Schmerr, N. (2012), The Gutenberg discontinuity: Melt at the lithosphere-asthenosphere boundary, *Science*, *335*, 1480–1483, doi:10.1126/science.1215433.

Schutt, D. L., and C. E. Lesher (2006), Effects of melt depletion on the density and seismic velocity of garnet and spinel lherzolite, *J. Geophys. Res.*, *111*, B05401, doi:10.1029/2003JB002950.

Shen, Y., and D. W. Forsyth (1995), Geochemical constraints on initial and final depths of melting beneath mid-ocean ridges, *J. Geophys. Res.*, *100*, 2211–2237.

Stixrude, L., and C. Lithgow-Bertelloni (2005), Mineralogy and elasticity of the oceanic upper mantle: Origin of the low-velocity zone, *J. Geophys. Res.*, *110*, B03204, doi:10.1029/2004JB002965.

Sundberg, M., and R. F. Cooper (2010), A composite viscoelastic model for incorporating grain boundary sliding and transient diffusion creep; correlating creep and attenuation responses for materials with a finite grain size, *Philos. Mag., 90*, 2817–2840, doi:10.1080/14786431003746656.

Tan, Y., and D. V. Helmberger (2007), Trans-Pacific upper mantle shear

velocity structure, *J. Geophys. Res.*, *112*, B08301, doi:10.1029/2006JB004853.

Tandon, G. P., and G. J. Weng (1984), The effect of aspect ratio of inclusions on the elastic properties of unidirectionally aligned composites, *Polymer Comps.*, *5*, 327–333, doi:10.1002/pc.750050413.

Till, C. B., T. L. Grove, R. W. Carlson, M. J. Fouch, J. M. Donnelly-Nolan, L. S. Wagner, and W. K. Hart (2013), Depths and temperatures of <10.5 Ma mantle melting and the lithosphere-asthenosphere boundary below southern Oregon and northern California, *Geochem. Geophys. Geosyst., 14*, 864–879, doi:10.1002/ggge.20070.

Tonegawa, T. and G. Helffrich (2012), Basal reflector under the Philippine sea plate, *Geophys. J. Int.*, *189*, 659-668, doi:10.1111/j.1365-246X.2012.05386.x.

Turcotte, D. L., and G. Schubert (2002), *Geodynamics*, 2nd ed., 456 pp., Cambridge Univ. Press, New York.

Villagómez, D. R., D. R. Toomey, E. E. Hooft, and S. C. Solomon (2007), Upper mantle structure beneath the Galápagos Archipelago from surface wave tomography, *J. Geophys. Res.*, *112*, B07303, doi:10.1029/2006JB004672.

Villagómez, D., D. R. Toomey, D. J. Geist, E. E. E. Hooft, and S. C. Solomon (2014), Mantle flow and multistage melting beneath the Galápagos hotspot revealed by seismic imaging, *Nature Geosci.*, *7*, 151–156, doi:10.1038/ngeo2062.

Vinnik, L. (1977), Detection of waves converted from P to SV in the mantle, *Phys. Earth Planet. Inter.*, *67*, 39–45, doi:10.1016/0031-9201(77)90008-5.

Vinnik, L. P., G. R. Foulger, and Z. Du (2005) Seismic boundaries in the mantle beneath Iceland: A new constraint on temperature, *Geophys. J. Int. 160*, 533–538, doi:10.1111/j.1365-246X.2005.02529.x.

Wagner, L. S., M. J. Fouch, D. E. James, and S. Hanson-Hedgecock (2012), Crust and upper mantle structure beneath the Pacific Northwest from joint inversion of ambient noise and earthquake data, *Geochem. Geophys. Geosyst.*, *13*, Q0AN03, doi:10.1029/2012GC004353.

Webb, S. C. (1998), Broadband seismology and noise under the ocean, *Rev. Geophys.*, *36*, 105–142, doi:10.1029/97RG02287.

White, W. M., A. R. McBirney, R. A. Duncan (1993), Petrology and geochemistry of the Galápagos Islands: Portrait of a pathological mantle plume, *J. Geophys. Res.*, *98*, 19533-19563, doi:10.1029/93JB02018.

Wölbern, I., A. W. B. Jacob, T. A. Blake, R. Kind, X. Li, X. Yuan, F. Duennebier, and M. Weber (2006), Deep origin of the Hawaiian tilted plume conduit derived

from receiver functions, *Geophys. J. Int.*, *166*, 767–781, doi:10.1111/j.1365-246X.2006.03036.x.

Yang, Y., D. W. Forsyth, and D. S. Weeraratne (2007), Seismic attenuation near the East Pacific Rise and the origin of the low-velocity zone, *Earth Planet. Sci. Lett.*, *258*, 260-268, doi:10.1016/j.epsl.2007.03.040.

Chapter III

Abers, G. A., K. M. Fischer, G. Hirth, D. A. Wiens, T. Plank, B. K. Holtzman, C. McCarthy, and E. Gazel (2014), Reconciling mantle attenuation-temperature relationships from seismology, petrology, and laboratory measurements, *Geochem. Geophys. Geosyst.*, *15*, 3521-3542, doi:10.1002/2014GC005444.

Anderson, D. L., and J. W. Given (1982), Absorption band *Q* model for the Earth, *J. Geophys. Res.*, 87, 3893–3904, doi:10.1029/JB087iB05p03893.

Backus, G., and F. Gilbert (1968), The resolving power of gross Earth data, *Geophys. J. Int.*, *16*, 169–205, doi:10.1111/j.1365-246X.1968.tb00216.x.

Bell, S., Y. Ruan, and D. W. Forsyth (2015), Shear velocity structure of abyssal plain sediments in Cascadia, *Seismol. Res. Lett.*, *86*, 1247-1252, doi: 10.1785/0220150101.

Bell, S., Y. Ruan, and D. W. Forsyth (2016), Ridge asymmetry and deep aqueous alteration at the trench observed from Rayleigh wave tomography of the Juan de Fuca plate, *J. Geophys. Res., 121*, 7298-7321, doi:10.1002/2016JB012990.

Bezada, M. J., E. D. Humphreys, D. R. Toomey, M. Harnafi, J. M. Dávila, and J. Gallart (2013), Evidence for slab rollback in westernmost Mediterranean from improved upper mantle imaging, *Earth Planet. Sci. Lett.*, *368*, 51–60, doi:10.1016/j.epsl.2013.02.024.

Bodmer, M., D. R. Toomey, E. E. Hooft, J. Nábělek, and J. Braunmiller (2015), Seismic anisotropy beneath the Juan de Fuca plate system: Evidence for heterogeneous mantle flow, *Geol.*, G37181.1, doi:10.1130/G37181.1.

Braunmiller, J., and J. Nábělek (2002), Seismotectonics of the Explorer region, *J. Geophys. Res.*, *107*, 2208, doi:10.1029/2001JB000220.

Braunmiller, J., and J. Nábělek (2008), Segmentation of the Blanco Transform Fault Zone from earthquake analysis: Complex tectonics of an oceanic transform fault, *J. Geophys. Res.*, *113*, B07108, doi:10.1029/2007JB005213.

Buck, W. R., and W. Su (1989), Focused mantle upwelling below mid-ocean ridges due to feedback between viscosity and melting, *Geophys. Res. Lett.*, *16*, 641–644, doi:10.1029/GL016i007p00641.

Carbotte, S. M., C. Small, and K. Donnelly (2004), The influence of ridge migration on the magmatic segmentation of mid-ocean ridges, *Nature*, *429*, 743–746, doi:10.1038/nature02652.

Carbotte, S. M., M. R. Nedimović, J. P. Canales, G. M. Kent, A. J. Harding, and M. Marjanović (2008), Variable crustal structure along the Juan de Fuca Ridge: Influence of on-axis hot spots and absolute plate motions, *Geochem. Geophys. Geosyst.*, *9*, Q08001, doi:10.1029/2007GC001922.

Chaytor, J. D., C. Goldfinger, R. P. Dziak, and C. G. Fox (2004), Active deformation of the Gorda plate: Constraining deformation models with new geophysical data, *Geol.*, *32*, 353-356, doi:10.1130/G20178.2.

Chen, Y., and W.J. Morgan (1990), Rift valley/no rift valley transition at mid-ocean ridges*, J. Geophys. Res.*, *95*, 17,583-17,604, doi:10.1029/JB095iB11p17571.

Conder, J. A, D. W. Forsyth, and E. M. Parmentier (2002), Asthenospheric flow and asymmetry of the East Pacific Rise, MELT area, *J. Geophys. Res.*, *107*, 2344, doi:10.1029/2001JB000807.

Cousens, B. L., J. F. Allan, M. I. Leybourne, R. L. Chase, N. Van Wagoner (1995), Mixing of magmas from enriched and depleted mantle sources in the northeast Pacific: West Valley segment, Juan de Fuca Ridge, *Contr. Mineral. and Petrol.*, *120*, 337-357, doi:10.1007/BF00306512.

Crotwell, H. P., T. J. Owens, and J. Ritsema (1999). The TauP Toolkit: Flexible seismic travel-time and ray-path utilities, *Seismol. Res. Lett., 70*, 154–160, doi: 10.1785/gssrl.70.2.154.

Dahlen, F., S. Hung, and G. Nolet (2000), Fréchet kernels for finite-frequency traveltimes—I. Theory, *Geophys. J. Int*, *141,* 157-174, doi:10.1046/j.1365-246X.2000.00070.x.

Dasgupta, R., and M. M. Hirschmann (2006), Melting in the Earth's deep upper mantle caused by carbon dioxide, *Nature*, *440*, 659–662, doi:10.1038/nature04612.

Dasgupta, R., A. Mallik, K. Tsuno, A. C. Withers, G. Hirth, and M. M. Hirschmann (2013), Carbon-dioxide-rich silicate melt in the Earth's upper mantle, *Nature*, 493, 211–215, doi:10.1038/nature11731.

Davis, A. S., D. A. Clague, B. L. Cousens, R. Keaten, and J. B. Paduan (2008), Geochemistry of basalt from the North Gorda segment of the Gorda Ridge: Evolution toward ultraslow spreading ridge lavas due to decreasing magma supply, *Geochem. Geophys. Geosyst.*, *9*, Q04004, doi:10.1029/2007GC001775.

DeCharon, A. V. (1989) Structure and tectonics of Cascadia segment, central Blanco Transform Fault Zone, *M.S. thesis*, pp. 73, Oreg. State Univ. Corvallis.

DeMets, C., R. G. Gordon, and D. F. Argus (2010), Geologically current plate motion, *Geophys. J. Int*, *181*, 1-80, doi: 10.1111/j.1365-246X.2009.04491.x.Divins, D. L. (2003), Total sediment thickness of the world's oceans & marginal seas, NOAA National Geophysical Data Center, Boulder, CO.

Dijkstra, E. W. (1959), A note on two problems in connection with graphs, *Numer. Math.*, *1*, 269–271.

Dziak, R. P. (2006), Explorer deformation zone: Evidence of a large shear zone and reorganization of the Pacific–Juan de Fuca–North American triple junction, *Geol.*, *34*, 213-216, doi:10.1130/G22164.1.

Embley, R. W. , and D. S. Wilson (1992) Morphology of the Blanco Transform Fault Zone-NE Pacific: Implications for its tectonic evolution, *Marine Geophys. Res.*, *14*, 25-45, doi: 10.1007/BF01674064.

Faul, U. H., D. R. Toomey, and H. S. Waff (1994), Intergranular basaltic melt is distributed in thin, elongated inclusions, *Geophys. Res. Lett.*, *21*, 29–32, doi:10.1029/93GL03051.

Faul, U. H. (2001), Melt retention and segregation beneath mid-ocean ridges, *Nature*, *410*, 920–923, doi:10.1038/35073556.

Faul, U. H., J. D. Fitzgerald, and I. Jackson (2004), Shear wave attenuation and dispersion in melt-bearing olivine polycrystals: 2. Microstructureal interpretation and seismological implications, *J. Geophys. Res.*, 109, B06202, doi:10.1029/2003JB002407.

Gaetani, G. A., S. E. DeLong, and D. A. Wark (1995), Petrogenesis of basalts from the Blanco Trough, northeast Pacific: Inferences for off-axis melt generation, *J. Geophys. Res.*, *100*, 4197-4214, doi:10.1029/94JB02774.

Ghorbani, P., Nabelek, J., and Braunmiller, J. (2015), Gorda and Juan de Fuca plate seismicity recorded by the Cascadia Initiative and Blanco transform fault zone seismic arrays, *Seismol. Res. Lett.*, *86*, 682, doi:10.1785/0220150017.

Goldstein, S. J., M. T. Murrell, D. R. Janecky, J. R. Delaney, and D. A. Clague (1991) Geochronology and petrogenesis of MORB from the Juan de Fuca and Gorda ridges by $^{238}U/^{230}Th$ disequilibrium, *Earth Planet. Sci. Lett.*, *107*, 25-41, doi: doi:10.1016/0012-821X(91)90041-F.

Graham, D. W., J. E. Lupton, F. J. Spera, and D. M. Christie (2001), Upper-mantle dynamics revealed by helium isotope variations along the southeast Indian ridge, *Nature*, *409*, 701–703, doi:10.1038/35055529

Graham, D. W., B. B. Hanan, C. Hémond, J. Blichert Toft, and F. Albarède (2014), Helium isotopic textures in Earth's upper mantle, *Geochem. Geophys. Geosyst.*, *15*(5), 2048–2074, doi:10.1002/2014GC005264.

Gregg, P. M., J. Lin, M. D. Behn, and L. G. J. Montési (2007), Spreading rate dependence of gravity anomalies along oceanic transform faults, *Nature*, *448*, 183–187, doi:10.1038/nature05962.

Hammond, W. C., and E. D. Humphreys (2000a), Upper mantle seismic wave velocity: Effects of realistic partial melt geometries, *J. Geophys. Res.*, *105*, 10,975–10,986, doi:10.1029/2000JB900041.

Hammond, W. C., and E. D. Humphreys (2000b), Upper mantle seismic wave attenuation: Effects of realistic partial melt distribution, *J. Geophys. Res.*, *105*, 10987-10999, doi:10.1029/2000JB900042.

Hammond, W. C., and D. R. Toomey (2003), Seismic velocity anisotropy and heterogeneity beneath the Mantle Electromagnetic and Tomography Experiment (MELT) region of the East Pacific Rise from analysis of P and S body waves, *J. Geophys. Res.*, *108*, 2176, doi:10.1029/2002JB001789.

Han, S., S. M. Carbotte, and J. P. Canales (2016), Seismic reflection imaging of the Juan de Fuca plate from ridge to trench: new constraints on the distribution of faulting and evolution of the crust prior to subduction, *J. Geophys. Res.*, *121*, 1849-1872, doi:10.1002/2015JB012416.

Haney, M. M., J. Power, M. West, and P. Michaels (2012), Causal instrument corrections for short-period and broadband seismometers, *Seismol. Res. Lett.*, *83*, 834–845, doi:10.1785/0220120031.

Harmon, N., D. W. Forsyth, and D. S. Weeraratne (2009), Thickening of young Pacific lithosphere from high-resolution Rayleigh wave tomography: A test of the conductive cooling model, *Earth Planet. Sci. Lett.*, *278*, 96–106, doi: 10.1016/j.epsl.2008.11.025.

Hawley, W. B., R. A. Allen, and M. R. Richards (2016), Tomography reveals buoyant asthenosphere accumulating beneath the Juan de Fuca plate, *Science*, *353*, 1406-1408, doi:10.1126/science.aad8104.

Hirschmann, M. M. (2010), Partial melt in the oceanic low velocity zone, *Phys. Earth Planet. Inter.*, *179*, 60–71, doi:10.1016/j.pepi.2009.12.003

Holtzman, B. K. (2016), Questions on the existence, persistence, and mechanical effects of a very small melt fraction in the asthenosphere, *Geochem. Geophys. Geosyst.*, *17,* 470-484, doi:10.1002/2015GC006102.

Holtzman, B. K., N. J. Groebner, M. E. Zimmerman, S. B. Ginsberg, and D. L. Kohlstedt (2003), Stress-driven melt segregation in partially molten rocks, *Geochem. Geophys. Geosyst.*, *4*, 8607, doi:10.1029/2001GC000258.

Hooft, E. E. E., and R. S. Detrick (1995), Relationship between axial morphology, crustal thickness, and mantle temperature along the Juan de Fuca and Gorda Ridges, *J. Geophys. Res.*, *100*, 22499, doi:10.1029/95JB02502.

Hung, S.-H., D. W. Forsyth, and D. R. Toomey (2000), Can a narrow, melt-rich, low-velocity zone of mantle upwelling be hidden beneath the East Pacific Rise? Limits from waveform modeling and the MELT Experiment, *J. Geophys. Res*, *105*, 7945–7960, doi:10.1029/1999JB900316.

Hyndman, R. D., R. P. Riddihough, and R. Herzer (1979), The Nootka fault zone – A new plate boundary off western Canada, *Geophys. J. R. Astron. Soc.*, 58, 667-683, doi:10.1111/j.1365-246X.1979.tb04801.x

Jackson, D. D. (1972), Interpretation of inaccurate, insufficient and inconsistent data, *Geophys. J. R. astr. Soc.*, *28*, 97-109

James, D. E., M. J. Fouch, J. B. Roth, and R. W. Carlson (2011), Slab fragmentation, edge flow, and the origin of the Yellowstone hotspot track, *Earth Planet. Sci. Lett.*, *311*, 124-135, doi:0.1016/j.epsl.2011.09.007.

James, E. K., C. A. Dalton, and J. B. Gaherty (2014), Rayleigh wave phase velocities in the Atlantic upper mantle, *Geochem. Geophys. Geosyst.*, *15*, 4305–4324, doi:10.1002/2014GC005518.

Jha, K., E. M. Parmentier, and J. Phipps Morgan (1994), The role of mantle-depletion and melt-retention buoyancy in spreading-center segmentation, *Earth Planet. Sci. Lett.*, *125*, 221–234, doi:10.1016/0012-821X(94)90217-8.

Katz, R. F. (2010), Porosity-driven convection and asymmetry beneath mid-ocean ridges, *Geochem. Geophys. Geosyst.*, 11, Q0AC07, doi:10.1029/2010GC003282.

Karato, S. (1993), Importance of anelasticity in the interpretation of seismic tomography, *Geophys. Res. Lett.*, *20*, 1623–1626, doi:10.1029/93GL01767.

Karato, S.-I. (2012), On the origin of the asthenosphere, *Earth Planet. Sci. Lett.*, *321*, 95–103, doi:10.1016/j.epsl.2012.01.001.

Karsten, J. L., S. R. Hammond, E. E. Davis, and R. G. Currie (1986), Detailed geomorphology and neotectonics of the Endeavour Segment, Juan de Fuca Ridge: New results from Seabeam swath mapping, *Geol. Soc. Am. Bull.*, *97*, 213 – 221, doi: doi: 10.1130/0016-7606(1986)9.

Karsten, J. L., J. R. Delaney, J. M. Rhodes, and R. A. Liias (1990), Spatial and temporal evolution of magmatic systems beneath the endeavour segment, Juan de Fuca Ridge: Tectonic and petrologic constraints, *J. Geophys. Res.*, *95*, 19235–19256, doi:10.1029/JB095iB12p19235.

Kawakatsu, H., P. Kumar, Y. Takei, M. Shinohara, T. Kanazawa, E. Araki, and K. Suyehiro (2009), Seismic evidence for sharp lithosphere-asthenosphere boundaries of oceanic plates, *Science*, *324*, 499–502, doi:10.1126/science.1169499.

Kennett, B. L. N., and E. R. Engdahl (1991), Traveltimes for global earthquake location and phase identification, *Geophys. J. R. Astron. Soc.*, *105*, 429–465, doi:10.1111/j.1365-246X.1991.tb06724.x

Key, K., S. Constable, L. Liu, and A. Pommier (2013), Electrical image of passive mantle upwelling beneath the northern East Pacific Rise, *Nature*, *495*, 499–502, doi:10.1038/nature11932.

Kumar, P., and H. Kawakatsu (2011), Imaging the seismic lithosphere-asthenosphere boundary of the oceanic plate, *Geochem. Geophys. Geosyst.*, *12*, Q01006, doi:10.1029/2010GC003358.

Liu, K., A. Levander, Y. Zhai, and R. W. Porritt (2012), Asthenospheric flow and lithospheric evolution near the Mendocino Triple Junction, *Earth Planet. Sci. Lett.*, *323-324*, 60-71, doi:10.1016/j.epsl.2012.01.020.

Lin, J., G. M. Purdy, H. Schouten, J. C. Sempere, and C. Zervas (1990), Evidence from gravity data for focused magmatic accretion along the Mid-Atlantic Ridge, *Nature, 344,* 627-632, doi:10.1038/344627a0.

Lupton, J. E., D. W. Graham, J. R. Delaney, and H. P. Johnson (1993), Helium isotope variations in Juan De Fuca Ridge basalts, *Geophys. Res. Lett.*, *20*, 1851–1854, doi:10.1029/93GL01271.

Magde, L. S., D. W. Sparks, and R. S. Detrick (1997), The relationship between buoyant mantle flow, melt migration, and gravity bull's eyes at the Mid-Atlantic Ridge between 33°N and 35°N, *Earth Planet. Sci. Lett.*, 148, 59-67, doi:10.1016/S0012-821X(97)00039-3.

Marjanović, M., S. M. Carbotte, M. R. Nedimović, and J. P. Canales (2011), Gravity and seismic study of crustal structure along the Juan de Fuca Ridge axis and across pseudofaults on the ridge flanks, *Geochem. Geophys. Geosyst.*, *12*, Q05008, doi:10.1029/2010GC003439.

Martin-Short, R., R. M. Allen, I. D. Bastow, and E. Totten (2015), Mantle flow geometry from ridge to trench beneath the Gorda-Juan de Fuca plate system, *Nat. Geosci.*, *8*, 965-967, doi:10.1038/ngeo2569

Moser, T. J. (1991), Shortest path calculation of seismic rays, *Geophysics*, *56*, 59–67, doi:10.1190/1.1442958.

Nettles, M., and A. M. Dziewoński (2008), Radially anisotropic shear velocity structure of the upper mantle globally and beneath North America, *J. Geophys. Res.*, *113*, B02303, doi:10.1029/2006JB004819

Nishimura, C. E., and D. W. Forsyth (1988), Rayleigh wave phase velocities in the Pacific with implications for azimuthal anisotropy and lateral heterogeneities, *Geophys. J. Int.*, *94*, 479–501, doi:10.1111/j.1365-246X.1988.tb02270.x.

Phipps Morgan, J., and D. W. Forsyth (1988) Three-dimensional flow and temperature perturbations due to a transform offset: Effect on oceanic crust and upper mantle structure, *J. Geophys. Res.*, *93*, 2955-2966, doi: 10.1029/JB093iB04p02955.

Putirka, K. D. (2005). Mantle potential temperatures at Hawaii, Iceland, and the mid-ocean ridge system, as inferred from olivine phenocrysts: Evidence for thermally driven mantle plumes, *Geochem., Geophys., Geosys.*, *6*, Q05L08, doi:10.1029/2005GC000915.

Riddihough, R. P. (1984), Recent movements of the Juan de Fuca plate system, *J. Geophys. Res.*, *89*, 6980-6994, doi:10.1029/JB089iB08p06980.

Rhodes, J. M., C. Morgan, R. A. Liias (1990) Geochemistry of Axial Seamount lavas: Magmatic relationship between the Cobb Hotspot and the Juan de Fuca ridge, *J. Geophys. Res., 95*, 12713–12733, doi: 10.1029/JB095iB08p12713.

Ruan, Y., D. W. Forsyth, and S. W. Bell (2014), Marine sediment shear velocity structure from the ratio of displacement to pressure of Rayleigh waves at seafloor, *J. Geophys. Res.*, *119,* 6257-6371, doi:10.1002/2014JB011162.

Rychert, C. A., and P. M. Shearer (2011), Imaging the lithosphere-asthenosphere boundary beneath the Pacific using *SS* waveform modeling, *J. Geophys. Res.*, *116*, B07307, doi:10.1029/2010JB008070.

Schmandt, B., Humphreys, E., (2010a), Complex subduction and small-scale convection revealed by body-wave tomography of the western United States upper mantle, *Earth Planet. Sci. Lett., 297,* 435–445, doi:10.1016/j.epsl.2010.06.047.

Schmandt, B., and E. Humphreys (2010b), Seismic heterogeneity and small-scale convection in the southern California upper mantle, *Geochem. Geophys. Geosys.*, *11*, Q05004, doi:10.1029/2010GC003042.

Schmandt, B., and F.-C. Lin (2014), P and S wave tomography of the mantle beneath the United States, *Geophys. Res. Lett.*, *41*, 6342–6349, doi:10.1002/2014GL061231.

Scott, D. R., and D. J. Stevenson (1989), A self-consistent model of melting, magma migration and buoyancy-driven circulation beneath mid-ocean ridges, *J. Geophys. Res.*, *94*, 2973–2988, doi:10.1029/JB094iB03p02973.

Small, C., and L. V. Danyushevsky (2003), Plate-kinematic explanation for mid-oceanic-ridge depth discontinuities, *Geol.*, *31*, 399-402, doi: 10.1130/0091-7613(2003)031.

Sparks, D. W., E. M. Parmentier, and J. Phipps Morgan (1993), Three-dimensional mantle convection beneath a segmented spreading center: Implications for along-axis variations in crustal thickness and gravity, *J. Geophys. Res.*, *98*, 21977-21995, doi:10.1029/93JB02397.

Spiegelman, M. (1996), Geochemical consequences of melt transport in 2-D: The sensitivity of trace elements to mantle dynamics, *Earth Planet. Sci. Lett.*, 139, 115–132, doi:10.1016/0012-821X(96)00008-8.

Spieglman, M., and J. R. Reynolds (1999) Combined dynamic and geochemical evidence for convergent melt flow beneath the East Pacific Rise, *Nature*, *402*, 282-285, doi:10.1038/46260.

Sours-Page, R., K. T. M. Johnson, R. L. Nielsen, and J. L. Karsten (1999), Local and regional variation of MORB parent magmas: Evidence from melt inclusions from the Endeavour Segment of the Juan de Fuca Ridge, *Contrib. Mineral. Petrol*., *134*, 342 – 363, doi:10.1007/s004100050489.

Stixrude, L., and C. L. Bertelloni (2005), Thermodynamics of mantle minerals–I. Physical properties, *Geophys. J. Int.*, *2*, 610-632, doi:10.1111/j.1365-246X.2005.02642.x

Su, W., and W. R. Buck (1993), Buoyancy effects on mantle flow under mid-ocean ridges, *J. Geophys. Res.*, *98*, 12,191-12,205, doi:10.1029/93JB00994

Sumy, D.F., Lodewyk, J.A., Woodward, R.L., and Evers, B. (2015), Ocean-bottom seismograph performance during the Cascadia Initiative, *Seismol. Res. Lett.*, *86*, doi:10.1785/0220150110

Tian, Y., W. Shen, and M. H. Ritzwoller (2013), Crustal and uppermost mantle shear velocity structure adjacent to the Juan de Fuca Ridge from ambient seismic noise, *Geochem. Geophys. Geosyst.*, *14*, 3221-3233, doi:10.1002/ggge.20206.

Toomey, D. R., and G. R. Foulger (1989), Tomographic inversion of local earthquake data from the Hengill-Grensdalur Central Volcano Complex, Iceland, *J. Geophys. Res.*, *94*, 17,497-17,510, doi:10.1029/JB094iB12p17497.

Toomey, D. R., S. C. Solomon, and G. Purdy (1994), Tomographic imaging of the shallow crustal structure of the East Pacific Rise at 9 30'N, *J. Geophys. Res.*, *99*, 24135–24157, doi:10.1029/94JB01942.

Toomey, D. R., W. Wilcock, J. A. Conder, D. W. Forsyth, J. D. Blundy, E. M. Parmentier, W. C. Hammond (2002), Asymmetric mantle dynamics in the MELT region of the East Pacific Rise, *Earth Planet. Sci. Lett.,* 200, 287-295, doi:10.1016/S0012-821X(02)00655-6.

Toomey, D.R., R.M. Allen, A.H. Barclay, S.W. Bell, P.D. Bromirski, R.L. Carlson, X. Chen, J.A. Collins, R.P. Dziak, B. Evers, D.W. Forsyth, P. Gerstoft, E.E.E. Hooft, D. Livelybrooks, J.A. Lodewyk, D.S. Luther, J.J. McGuire, S.Y. Schwartz, M. Tolstoy, A.M. Tréhu, M. Weirathmueller, and W.S.D. Wilcock (2014), The Cascadia initiative: A sea change in seismological studies of subduction zones, *Oceanography*, *27*, 138–150, doi:10.5670/oceanog.2014.49.

Turcotte, D. L., and G. Schubert (2002), Geodynamics, 2nd ed., 456 pp., Cambridge Univ. Press, New York.

VanDecar, J. C., and R. S. Crosson (1990), Determination of teleseismic relative phase arrival times using multi-channel cross-correlation and least squares, *Bull. Seis. Soc. Am.*, *80,* 150-169.

Vasco, D. W., and L. R. Johnson (2003), Resolution, uncertainty, and whole Earth tomography, *J. Geophys. Res., 108*, 2022, doi:10.1029/2001JB000412

Villagómez, D. R., D. R. Toomey, D. J. Geist, E. E. E. Hooft, and S. C. Solomon (2014), Mantle flow and multistage melting beneath the Galápagos hotspot revealed by seismic imaging, *Nature Geosci*, *7*, 151–156, doi:10.1038/ngeo2062.

Wang, Y., D. W. Forsyth, and B. Savage (2009), Convective upwelling in the mantle beneath the Gulf of California, *Nature*, *462*, 499–501, doi:10.1038/nature08552.

Webb, S. C. (1998), Broadband seismology and noise under the ocean, *Rev. Geophys.*, *36*, 105–142, doi:10.1029/97RG02287.

Wilson, D. S., R. N. Hey, C. Nishimura (1984), Propagation as a mechanism of reorientation of the Juan de Fuca Ridge, *J. Geophys. Res.*, *89*, 9215–9225, doi: 10.1029/JB089iB11p09215

Wilson, D. S. (1986), A kinematic model for the Gorda Deformation Zone as a diffuse southern boundary of the Juan de Fuca Plate, *J. Geophys. Res.*, *91*, 10259–10269, doi:10.1029/JB091iB10p10259.

Wilson, D. S. (1989), Deformation of the so-called Gorda Plate, *J. Geophys. Res.*, *94*, 3065–3075, doi:10.1029/JB094iB03p03065.

Wilson, D. S. (1992), Focused mantle upwelling beneath mid-ocean ridges: evidence from seamount formation and isostatic compensation of topography, *Earth Planet. Sci. Lett.*, *113*, 41-55, doi: 10.1016/0012-821X(92)90210-M.

Wilson, D. S. (1993), Confidence intervals for motion and deformation of the Juan de Fuca plate, *J. Geophys. Res., 98*, 16,053-16,701, doi: 10.1029/93JB01227.

Xue, M., and R. M. Allen (2010), Mantle structure beneath the western United States and its implications for convection processes, *J. Geophys. Res.*, *115*, B07303, doi:10.1029/2008JB006079.

Yang, Y., D. W. Forsyth, and D. S. Weeraratne (2007), Seismic attenuation near the East Pacific Rise and the origin of the low-velocity zone, *Earth Planet. Sci. Lett.*, *258*, 260–268, doi:10.1016/j.epsl.2007.03.040.

Yang, Y., and D. W. Forsyth (2008), Attenuation in the upper mantle beneath Southern California: Physical state of the lithosphere and asthenosphere, *J. Geophys. Res., 113,* doi*:* 10.1029/2007JB005118.

Chapter IV

Bagley, B., and J. Revenaugh (2008), Upper mantle seismic shear discontinuities of the Pacific, *J. Geophys. Res.*, *113*, B12, doi:10.1029/2008JB005692.

Beghein, C., K. Yuan, N. Schmerr, and Z. Xing (2014), Changes in Seismic Anisotropy Shed Light on the Nature of the Gutenberg Discontinuity, *Science*, *343*, 1237-1240, doi:10.1126/science.1246724.

Bell, S., Y. Ruan, and D. W. Forsyth (2016), Ridge asymmetry and deep aqueous alteration at the trench observed from Rayleigh wave tomography of the Juan de Fuca plate, *J. Geophys. Res., 121*, doi:10.1002/2016JB012990*.*

Becker, T. W., C. P. Conrad, A. J. Schaeffer, and S. Lebedev (2014), Origin of azimuthal seismic anisotropy in oceanic plates and mantle, *Earth Planet. Sci. Lett., 401*, 236-250, doi:10.1016/j.epsl.2014.06.014.

Behn, M. D., G. Hirth, and J. R. Elsenbeck II (2009) Implications of grain size evolution on the seismic structure of the oceanic upper mantle, *Earth Planet. Sci. Lett.*, *282*, 178-189*,* doi:10.1016/j.epsl.2009.03.014.

Bodmer, M., D. R. Toomey, E. E. Hooft, J. Nábělek, and J. Braunmiller (2015), Seismic anisotropy beneath the Juan de Fuca plate system: Evidence for heterogeneous mantle flow, *Geol.*, G37181.1, doi:10.1130/G37181.1.

Bostock, M. G. (1999), Seismic waves converted from velocity gradient anomalies in the Earth's upper mantle, *Geophys. J. Int.*, *138*, 747-756, doi: 10.1046/j.1365-246x.1999.00902.x.

Blackman, D. K., J. A. Orcutt, and D. W. Forsyth (1995), Recording teleseismic earthquakes using ocean-bottom seismographs at mid-ocean ridges, *Bull. .Seis. Soc. Am.*, *85*, 1648-1664.

Buck, W. R., C. Small, and W. B. F. Ryan (2009) Constraints on asthenospheric flow from the depths of oceanic spreading centers: The East Pacific Rise and the Australian-Antarctic Discordance, *Geochem. Geophys. Geosys.*, *10*, Q09007, doi:10.1029/2009GC002373.

Conrad, C. P., M. D. Behn, and P. G. Silver (2007), Global mantle flow and the development of seismic anisotropy: Differences between the oceanic and continental upper mantle, *J. Geophys. Res*., *112,* B7, doi:10.1029/2006JB004608.

Dasgupta, R., and M. M. Hirschmann (2006), Melting in the Earth's deep upper mantle caused by carbon dioxide, *Nature*, *440*, 659–662, doi:10.1038/nature04612.

Debayle, E. and Y. Ricard (2013), Seismic observations of large-scale deformation at the bottom of fast-moving plates, *Earth Planet. Sci. Lett.*, *376*, 165-177, doi: 10.1016/j.epsl.2013.06.025.

DeMets, C., R. G. Gordon, and D. F. Argus (2010), Geologically current plate motion, *Geophys. J. Int*, *181*, 1-80, doi: 10.1111/j.1365-246X.2009.04491.x.

Dziewonski. A. M., and D. L. Anderson (1981) Preliminary Earth Reference Model, *Phys. Earth Planet. Int.*, *25*, 297-365, doi:10.1016/0031-9201(81)90046-7.

Gaherty, J. B., and T. H. Jordan (1995), Lehmann Discontinuity as the Base of an Anisotropy Layer Beneath Continents, *Science*, 268, 1468-1471.

Gaherty, J. B., T. H. Jordan, and L. S. Gee (1996) Seismic structure of the upper mantle in a central Pacific corridor, *J. Geophys. Res.*, *101*, 22,291-22,309, doi:10.1029/96JB01882.

Gu, Y. J., A. M. Dziewonski, and G. Ekström (2001), Preferential detection of the Lehmann discontinuity beneath continents, *Geophys. Res. Lett.*, *28*, doi:10.1029/2001GL013679.

Hamilton, E. L. (1979), Vp/Vs and Poisson's ratios in marine sediments and rocks, *J. Acoustical. Soc. Am.*, *66*, 1094, doi:10.1121/1.383344.

Hammond, W. C., and D. R. Toomey (2003), Seismic velocity anisotropy and heterogeneity beneath the Mantle Electromagnetic and Tomography Experiment (MELT) region of the East Pacific Rise from analysis of P and S body waves, *J. Geophys. Res.*, *108*, 2176, doi:10.1029/2002JB001789.

Harmon, N., D. W. Forsyth, R. Lamm, and S. C. Webb (2007), P and S wave delays beneath intraplate volcanic ridges and gravity lineations near the East Pacific Rise, *J. Geophys. Res.*, *112*, B03309, doi:10.1029/2006JB004392.

Havlin, C. and E. M. Parmentier (2014), Implications for melt transport and source heterogeneity in upwelling mantle form the magnitude of Sp converted phases generated at the onset of melting, *Geophys. Res. Lett.*, *41*, 5,444-5450, doi:10.1002/2014GL060890.

Haxby, W. F. and J. K. Weissel (1986), Evidence for small-scale mantle convection from Seasat altimeter data, *J. Geophys. Res.*, *91*, 3,507-3,520, doi:10.1029/JB091iB03p03507.

Helffrich, G. (2006), Extended-time multitaper frequency domain cross-correlation receiver-function estimation, *Bull. Seismol. Soc. Am*., 96,344–347, doi:10.1785/0120050098.

Hirschmann, M. M. (2010), Partial melt in the oceanic low velocity zone, *Phys. Earth Planet. Inter*., *179*, 60–71, doi:10.1016/j.pepi.2009.12.003.

Hirth, G., and D. L. Kohlstedt (1996), Water in the upper oceanic mantle: implications for rheology, melt extraction and the evolution of the lithosphere, *144*, 93-108, doi:10.1016/0012-821X(96)00154-9.

Höink, T., A, Lenardic, M. Richards (2012), Depth-dependent viscosity and mantle stress amplification: implications for the role of the asthenosphere in maintaining plate tectonics, *Geophys. J. Int.*, *191*, 30-41, doi:10.1111/j.1365-246X.2012.05621.x.

Karato, S.-I. (1992), On the Lehmann discontinuity, *Geophys. Res. Lett., 19*, 2,255-2,258, doi:10.1029/92GL02603.

Karato, S.-I. (1993), Importance of anelasticity in the interpretation of seismic tomography, *Geophys. Res. Lett.*, *20*, 1623–1626, doi:10.1029/93GL01767.

Karato, S.-I., and P. Wu (1993), Rheology of the Upper Mantle: A Synthesis, *Science*, *260*, 771-778.

Kawakatsu, H., P. Kumar, Y. Takei, M. Shinohara, T. Kanazawa, E. Araki, and K. Suyehiro (2009), Seismic evidence for sharp lithosphere-asthenosphere boundaries of oceanic plates, *Science*, *324*, 499–502, doi:10.1126/science.1169499.

Kennett, B. L. N., and E. R. Engdahl (1991), Traveltimes for global earthquake location and phase identification, *Geophys. J. R. Astron. Soc*., *105*, 429–465, doi:10.1111/j.1365-246X.1991.tb06724.x

Kumar, P., and H. Kawakatsu (2011), Imaging the seismic lithosphere-asthenosphere boundary of the oceanic plate, *Geochem. Geophys. Geosyst.*, *12*, Q01006, doi:10.1029/2010GC003358.

Lehmann, I. (1937), S and the structure of the upper mantle, *Geophys. J. Int.*, *4*, 124-138, doi:10.1111/j.1365-246X.1937.tb07108.x.

Lin, P. P, J. B. Gaherty, G. Jin, J. A. Collins, D. Lizarralde, R. L. Evans, and G. Hirth (2016), High-resolution seismic constraints on flow dynamics in the oceanic asthenosphere, *Nature,* 538-541, doi:10.1038/nature18012.

Maggi, A., E. Debayle, K. Priestley, and G. Barruol (2006), Azimuthal anisotropy of the Pacific region, *Earth Planet. Sci. Lett*., *250*, 53-71, doi: 10.1016/j.epsl.2006.07.010.

Martin-Short, R., R. M. Allen, I. D. Bastow, E. Totten, and M. R. Richards (2015) Mantle flow geometry from ridge to trench beneath the Gorda-Juan de Fuca plate system, *Nat. Geosci.*, *8*, 965-968, doi:10.1038/ngeo2569.

Montagner, J.-P., and T. Tanimoto (1991), Global upper mantle tomography of seismic velocities and anisotropies, *J. Geophys. Res.*, *96*, 20,337-20,351, doi:10.1029/91JB01890.

Nishimura, C. E., and D. W. Forsyth (1988), Rayleigh wave phase velocities in the Pacific with implications for azimuthal anisotropy and lateral heterogeneities, *Geophys. J. Int.*, *94*, 479–501, doi:10.1111/j.1365-246X.1988.tb02270.x.

Park, J., C. R. Lindberg, and F. L. Vernon (1987), Multitaper spectral analysis of high-frequency seismograms, *J. Geophys. Res*., *92*, 12,675–12,684, doi:10.102 9/JB092iB12p12675.

Park, J., and V. Levin (2000), Receiver functions from multiple-taper spectral correlation estimates, *Bull. Seismol. Soc. Am*., *90*, 1507–1520, doi:10.1785/0119990122.

Phipps Morgan, J., and W. H. F. Smith (1992), Flattening of the sea-floor depth-age curve as a response to asthenospheric flow, *Nature*, *359,* 524-526.

Phipps Morgan, J., W. J. Morgan, Y.-S. Zhang, and W. H. F. Smith (1995), Observational hints for a plume-fed, suboceanic asthenosphere and its role in mantle convection, *J. Geophys. Res.*, *100*, 12,753-12,767, doi:10.1029/95JB00041.

Podolefsky, N. S., S. Zhong, and A. K. McNamara (2004), The anisotropic and rheological structure of the oceanic upper mantle from a simple model of plate shear, *Geophys. J. Int.*, *158*, 287-296, doi:10.1111/j.1365-246X.2004.02250.x.

Richard, Y., C. Doglioni, and R. Sabadini (1991), Differential rotation between lithosphere and mantle: A consequence of lateral mantle viscosity variations, *J. Geophys. Res.*, *96*, 8407-8415, doi:10.1029/91JB00204.

Riddihough, R. P. (1984), Recent movements of the Juan de Fuca plate system, *J. Geophys. Res.*, *89*, 6980-6994, doi:10.1029/JB089iB08p06980.

Rost, S., and M. Weber (2001), A reflector at 200 km depth beneath the northwest Pacific, *Geophys. J. Int.*, *147*, 12-28, doi:10.1046/j.1365-246X.2001.00497.x.

Ruan, Y., D. W. Forsyth, and S. W. Bell (2014), Marine sediment shear velocity structure from the ratio of displacement to pressure of Rayleigh waves at seafloor, *J. Geophys. Res.*, *119,* 6257-6371, doi:10.1002/2014JB011162.

Rychert, C. A., S. Rondenay, and K. M. Fischer (2007), P-to-S and S-to-P imaging of a sharp lithosphere-asthenosphere boundary beneatheastern North America, *J. Geophys. Res.*, *112*, B08314, doi:10.1029/2006JB004619.

Sambridge, M., and K. Mosegaard (2002) Monte Carlo methods in geophysical inverse problems, *Rev. Geophys., 40*, 1-29, doi:10.1029/2000RG000089.

Silver, P. G., W. W. Chan (1991) Shear wave splitting and subcontinental mantle deformation, *J. Geophys. Res.*, *96*, 16429-16454, doi: 10.1029/91JB00899.

Shen, W., M. R. Ritzwoller, V. Schulte-Pelkum, and F. C. Lin (2013), Joint inversion of surface wave dispersion and receiver functions: a Bayesian Monte-Carlo approach, *192*, 807-836, doi: 10.1093/gji/ggs050.

Sumy, D.F., Lodewyk, J.A., Woodward, R.L., and Evers, B. (2015), Ocean-bottom seismograph performance during the Cascadia Initiative, *Seis. Res. Lett.*, *86*, doi:10.1785/0220150110.

Takeo, A., H. Kawakatsu, T. Isse, K. Nishida, H. Sugioka, A. Ito, H. Shiobara, and D. Suetsugu (2016), Seismic azimuthal anisotropy in the oceanic lithosphere and asthenosphere from broadband surface wave analysis of OBS array records at 60 Ma seafloor, *J. Geophys. Res., 121*, 1,927-1,947, doi:10.1002/2015JB012429.

Tommasi, A. (1998), Forward modeling of the development of seismic anisotropy in the upper mantle, *Earth Planet. Sci. Lett.*, *160*, 1-13, doi: 10.1016/S0012-821X(98)00081-8.

Toomey, D. R., D. Jousselin, R. A. Dunn, W. S. D. Wilcock, and R. S. Detrick (2007), Skew of mantle upwelling beneath the East Pacific Rise governs segmentation, *Nature*, *446*, 409-414, doi:10.1038/nature05679.

Toomey, D.R., R.M. Allen, A.H. Barclay, S.W. Bell, P.D. Bromirski, R.L. Carlson, X. Chen, J.A. Collins, R.P. Dziak, B. Evers, D.W. Forsyth, P. Gerstoft, E.E.E. Hooft, D. Livelybrooks, J.A. Lodewyk, D.S. Luther, J.J. McGuire, S.Y. Schwartz, M. Tolstoy, A.M. Tréhu, M. Weirathmueller, and W.S.D. Wilcock (2014), The Cascadia initiative: A sea change in seismological studies of subduction zones, *Oceanography*, *27*, 138–150, doi:10.5670/oceanog.2014.49.

VanderBeek, B. P., D. R. Toomey, E. E. E. Hooft, and W. S. D. Wilcock (2016), Segmentation of mid-ocean ridges attributed to oblique mantle divergence, *Nat. Geosci.*, *9*, 636-642, doi:10.1038/ngeo2745.

Vinnik, L. (1977), Detection of waves converted from P to SV in the mantle, *Phys. Earth Planet. Inter.*, *67*, 39–45, doi:10.1016/0031–9201(77)90008-5.

Vinnik, L., E. Kurnik, and V. Farra (2005), Lehmann discontinuity beneath North America: No role for seismic anisotropy, *Geophys. Res. Lett.*, *32*, doi:10.1029/2004GL022333.

Webb, S. C. (1998), Broadband seismology and noise under the ocean, *Rev. Geophys.*, *36*, 105–142, doi:10.1029/97RG02287.

Weismüller, J. B. Gmeiner, S. Ghelichkhan, M. Huber, L. John, B. Wohlmuth, U. Rüde, and H.-P. Bunge (2015), Fast asthenosphere motion in high-resolution global mantle flow models, *Geophys. Res. Lett.*, *42*, 7,429-7,425, doi:10.1002/2015GL063727.

Wilson, D. C., D. A. Angus, J. F. Ni, and S. P. Grand (2006) Constraints on the interpretation of S-to-P receiver functions, *Geophys. J. Int.*, *165*, 96-980, doi: 10.1111/j.1365-246X.2006.02981.x.

Wüstefeld, A., G. Bokelmann, C. Zaroli, and G. Barruol (2008) SplitLab: A shear-wave splitting environment in Matlab, *Computers and Geosciences*, *34*, 515-528, doi:10.1016/j.cageo.2007.08.002.

Yuan, X. R. Kind, X. Li, and R. Wang (2006) The *S* receiver functions: synthetics and data example, *Geophys. J. Int*, *165*, 555-565, doi:10.1111/j.1365-246X.2006.02885.x.

Zhang, S., and S.-I. Karato (1995), Lattice preferred orientation of olivine aggregates deformed in simple shear, *Nature*, *375*, 774-777, doi:10.1038/375774a0.